HANDBOOK ON THE PHYSICS AND CHEMISTRY OF RARE EARTHS

North-Holland is an imprint of Elsevier

Radarweg 29, PO Box 211, 1000 AE Amsterdam, The Netherlands
The Boulevard, Langford Lane, Kidlington, Oxford OX5 1GB, UK

Notices
Knowledge and best practice in this field are constantly changing. As new research and experience broaden our understanding, changes in research methods, professional practices, or medical treatment may become necessary.

Practitioners and researchers must always rely on their own experience and knowledge in evaluating and using any information, methods, compounds, or experiments described herein. In using such information or methods they should be mindful of their own safety and the safety of others, including parties for whom they have a professional responsibility.

To the fullest extent of the law, neither the Publisher nor the authors, contributors, or editors, assume any liability for any injury and/or damage to persons or property as a matter of products liability, negligence or otherwise, or from any use or operation of any methods, products, instructions, or ideas contained in the material herein.

ISBN: 978-0-444-63260-9
ISSN: 0168-1273

Contributors

Numbers in Parentheses indicate the pages on which the author's contributions begin.

Alban Ferrier (1), Institut de Recherche de Chimie Paris, CNRS-Chimie, ParisTech, and Sorbonne Universités, UPMC Univ Paris 06, Paris, France

Koichiro Fujinaga (79), Department of Systems Innovation and Frontier Research Center for Energy and Resources (FRCER), School of Engineering, The University of Tokyo, Bunkyo-ku, Japan

Philippe Goldner (1), Institut de Recherche de Chimie Paris, CNRS-Chimie, ParisTech, Paris, France

Olivier Guillot-Noël (1), Institut de Recherche de Chimie Paris, CNRS-Chimie, ParisTech, Paris, France

Satoru Haraguchi (79), Department of Solid Earth Geochemistry, Japan Agency for Marine-Earth Science and Technology (JAMSTEC), Yokosuka, Japan

Yasuhiro Kato (79), Department of Systems Innovation and Frontier Research Center for Energy and Resources (FRCER), School of Engineering, The University of Tokyo, Bunkyo-ku, Japan; Research and Development Center for Submarine Resources, Japan Agency for Marine-Earth Science and Technology (JAMSTEC), Yokosuka, Japan

Shiki Machida (79), Department of Resources and Environmental Engineering, School of Creative Science and Engineering, Waseda University, Shinjyu-ku, Japan

Kentaro Nakamura (79), Department of Systems Innovation, School of Engineering, The University of Tokyo, Bunkyo-ku, and Research and Development Center for Submarine Resources, Japan Agency for Marine-Earth Science and Technology (JAMSTEC), Yokosuka, Japan

Junichiro Ohta (79), Department of Systems Innovation, School of Engineering, The University of Tokyo, Bunkyo-ku, Japan

Yutaro Takaya (79), Research and Development Center for Submarine Resources, Japan Agency for Marine-Earth Science and Technology (JAMSTEC), Yokosuka, Japan

Kazutaka Yasukawa (79), Department of Systems Innovation, School of Engineering, The University of Tokyo, Bunkyo-ku, Japan

Preface

These elements perplex us in our reaches [sic], baffle us in our speculations, and haunt us in our very dreams. They stretch like an unknown sea before us—mocking, mystifying, and murmuring strange revelations and possibilities.

Sir William Crookes (February 16, 1887)

Volume 46 of the *Handbook on the Physics and Chemistry of Rare Earths* features two chapters covering two very different subjects pertaining to crystals for quantum information and to potential new deep-sea resources.

Chapter 267 gives insight into a new and exciting field of quantum science: quantum communications, storage, and computing. Digital information is playing a crucial role in present-day world but its fundamental concepts were developed at the beginning of the twentieth century. In the mid-1980s, a new paradigm emerged in which classical bits of information that can only take discrete values of 0 and 1 are replaced by quantum bits (qubits) able to adopt any superposition state. Quantum processing information is, however, requiring very sophisticated materials with highly demanding properties because superposition states are destroyed by fluctuating environments. Therefore, a classical carrier for quantum information is light because photons only weakly interact with atoms and electromagnetic fields. Rare-earth-doped crystals have very narrow optical transitions and are consequently well suited as quantum information materials; appropriate ions include Pr^{3+}, Nd^{3+}, Eu^{3+}, Er^{3+}, or Tm^{3+}. After an introduction on quantum information and light-atom interactions, the review focuses on rare-earth spectroscopy and associated experimental techniques, absorption, hole burning and spectral tailoring for observing hyperfine structures, Raman heterodyne scattering, as well as techniques used for determining coherence lifetimes. Two applications are then discussed in more details: quantum memories based on light and quantum computers. In these last sections, concepts and protocols are presented as well as a few representative experimental examples.

Chapter 268 deals with potential new rare-earth resources. Rare-earth elements are distributed broadly in the Earth's crust but in relatively small concentrations and always as mixtures. Natural abundances of the elements in Earth's crust vary considerably, from 60 to 70 ppm for cerium to

less than 0.5 ppm for lutetium. Several hundreds of rare-earth-containing minerals are known, but only a few are exploited commercially. The minerals containing light lanthanides (La through Eu) have an equivalent rare-earth oxide (REO) content in the range 5–10 wt.%, while ion-adsorption clays exploited for heavy lanthanides (Gd–Lu) and Y contain less than 1 wt.% of REO. At the turn of the century, China emerged as the major producer of rare earths worldwide with a share reaching over 95% in 2010. Exportation quotas were introduced in 2006 and considerably reduced in 2010 following geopolitical tensions in Asia. As a consequence, several countries started to look for alternative, possibly domestic, supplies. In this context, the authors of the chapter report that deep-sea muds in the eastern South Pacific and central North Pacific contain 0.1–0.2 wt.% rare earths and can be recovered by established drilling techniques followed by simple acid leaching. The chapter first presents rare-earth distribution in Pacific, Indian, and Atlantic Oceans together with their lithological and geochemical characteristics. It then continues with a description of the minerals contained in the muds followed by a detailed discussion of the advantages of this new rare-earth resource. The review ends by presenting practical mining and leaching systems.

CHAPTER 267: RARE EARTH-DOPED CRYSTALS FOR QUANTUM INFORMATION PROCESSING

By Philippe Goldner, Alban Ferrier, and Olivier Guillot-Noël
Chimie ParisTech and Université Pierre et Marie Curie, Paris, France

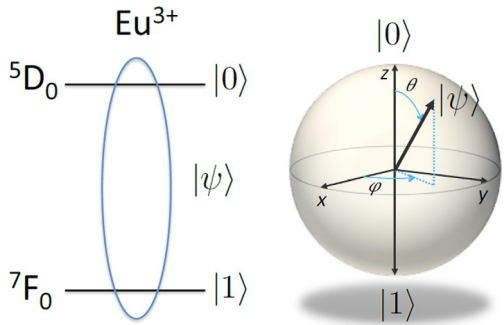

Quantum information processing uses superposition states of photons or atoms to process, store, and transmits data in ways impossible to reach with classical systems. For example, a quantum computer could find the prime factors of large numbers much faster than a classical computer. It could also be used to efficiently simulate a collection of interacting quantum systems. Moreover, quantum communications based on the fundamental laws of quantum mechanics offer unrivaled security for data transmission. Quantum memories have also been developed to transfer quantum states between different systems, like photons and atoms. It is even envisaged that the combination of quantum computing, transmission, and storage could create a quantum internet. Rare-earth-doped crystals have recently emerged as promising solid-state systems for quantum information processing, mainly because they exhibit very narrow optical transitions at low temperature. This allows one to use these materials as quantum light-matter interfaces or to control their quantum states optically. Moreover, many rare earths possess a nonzero nuclear spin, opening perspectives for the use of long-lived quantum states in processing or storage.

After a brief introduction to quantum information processing and coherent light-matter interactions, specific spectroscopic properties of rare-earth-doped crystals are reviewed. This includes hyperfine structures, coherent properties of optical and hyperfine transitions, as well as techniques to extend coherence lifetimes. Two main applications are then dealt with: quantum memories based on light and quantum computing. An example of quantum memory relies on an entangled pair of photons in Y_2SiO_5:Nd(0.0003 at.%), while high-fidelity, long storage can be achieved with $La_2(WO_4)_3$:Pr(0.2 at.%). In the case of quantum computing, single- (Y_2SiO_5:Pr(0.05 at.%)) and two-qubit gates (Y_2SiO_5:Eu(0.02 at.%)) are presented.

CHAPTER 268: REY-RICH MUD: A DEEP-SEA MINERAL RESOURCE FOR RARE EARTHS AND YTTRIUM

By Kentaro Nakamura, Koichiro Fujinaga, Kazutaka Yasukawa, Yutaro Takaya, Junichiro Ohta, Shiki Machida, Satoru Haraguchi, and Yasuhiro Kato

The University of Tokyo, Japan Agency for Marine-Earth Science and Technology, and Waseda University

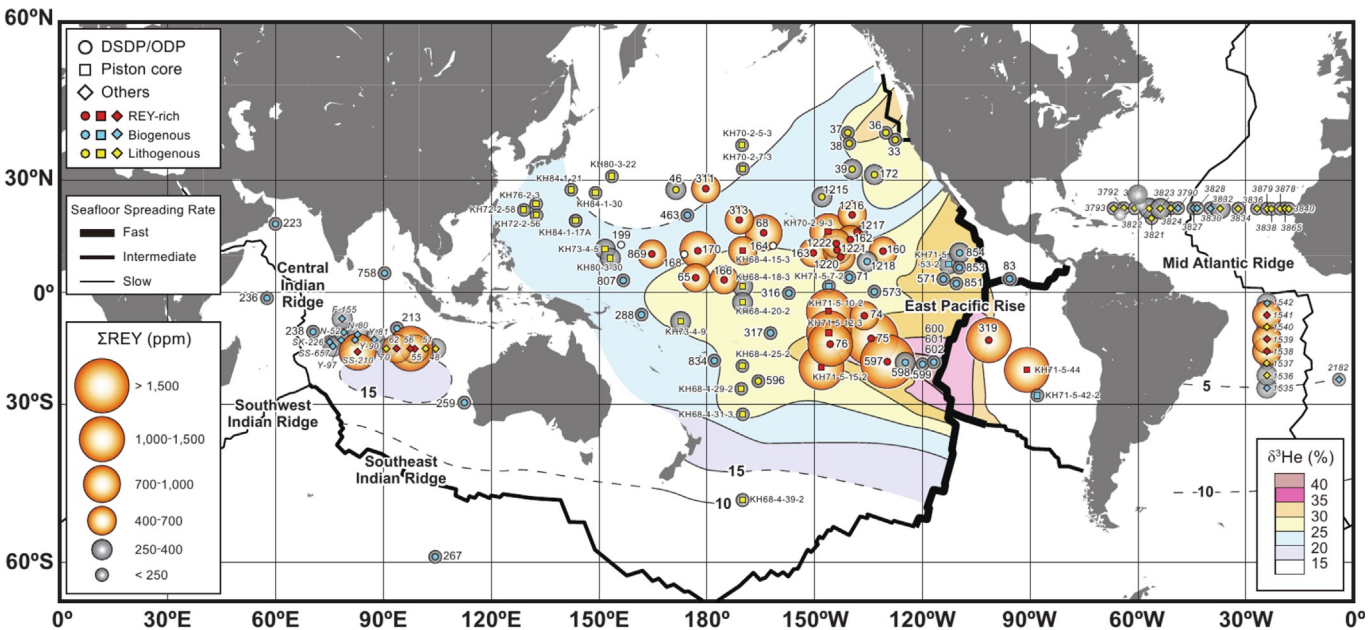
DSDP/ODP
Piston core
Others
REY-rich
Biogenous
Lithogenous
Seafloor Spreading Rate
Fast
Intermediate
Slow
ΣREY (ppm)
> 1,500
1,000-1,500
700-1,000
400-700
250-400
< 250
δ3He (%)
40
35
30
25
20
15
Central Indian Ridge
Southwest Indian Ridge
Southeast Indian Ridge
East Pacific Rise
Mid Atlantic Ridge
60°N
30°N
0°
30°S
60°S
0°
30°E
60°E
90°E
120°E
150°E
180°
150°W
120°W
90°W
60°W
30°W
0°

Rare-earth elements and yttrium (denoted REY in this chapter) are important materials for high-technology applications and green energy technologies (e.g., flat screen televisions, cell phones, electric/hybrid vehicles, and wind power generators). World demand for REY is increasing rapidly, and a stable supply of REY is required for future development of technology and the global economy. Diversification of sources and increased access to REY resources are, therefore, crucial to maintain supply capable of meeting the ever-rising demand. Here, newly discovered extensive deposits of deep-sea mud containing high REY concentrations (called REY-rich mud) are presented. The deep-sea REY-rich muds are characterized by (1) tremendous resource potential by virtue of their wide distribution, (2) high REY concentrations with significant heavy lanthanide enrichment, (3) a stratiform distribution that allows relatively simple and cost-effective exploration, (4) very low concentrations of radioactive elements such as Th and U, and (5) ease of extraction of REY by acid leaching. In addition, a system to mine REY-rich muds can be developed based on a technique developed and tested to mine sulfide-rich muds in the Red Sea and manganese nodules in the Pacific Ocean. These features demonstrate that the REY-rich mud could constitute a highly promising REY resource for the future.

The chapter starts with an introduction on rare-earth elements, their deposits onshore, as well as brief introduction of the new discovery of the REY-rich mud. It then focuses on distribution, lithological and geochemical characteristics, host phases, and genesis of REY-rich muds. The review ends with considerations on resource potential, advantages of developing, and conceivable development systems.

Jean-Claude G. Bünzli
Vitalij K. Pecharsky

Contents of Volumes 1–45

VOLUME 7

1984; ISBN 0-444-86851-8

VOLUME 8

1986; ISBN 0-444-86971-9

VOLUME 9

1987; ISBN 0-444-87045-8

VOLUME 10: High energy spectroscopy

1987; ISBN 0-444-87063-6

VOLUME 11: Two-hundred-year impact of rare earths on science

1988; ISBN 0-444-87080-6

VOLUME 12

1989; ISBN 0-444-87105-5

VOLUME 13

1990; ISBN 0-444-88547-1

VOLUME 18: Lanthanides/Actinides: Chemistry
1994; ISBN 0-444-81724-7

VOLUME 19: Lanthanides/Actinides: Physics – II
1994; ISBN 0-444-82015-9

VOLUME 32

2001; ISBN 0-444-50762-0

VOLUME 33

2003; ISBN 0-444-51323-X

VOLUME 34

2004; ISBN 0-444-51587-9

VOLUME 35

2005; ISBN 0-444-52028-7

VOLUME 36

2006; ISBN 0-444-52142-9

VOLUME 37: Optical Spectroscopy

2007; ISBN 978-0-444-52144-6

VOLUME 38

2008; ISBN 978-0-444-52143-9

VOLUME 44: Including Actinides
2014; ISBN 978-0-444-62711-7

VOLUME 45: Including Actinides
2014; ISBN 978-0-444-63256-2

Index of Contents of Volumes 1–46

D

E

F

G

H

I

K

L

M

N

O

P

Q

R

S

T

U

V

X

Chapter 267

Rare Earth-Doped Crystals for Quantum Information Processing

Philippe Goldner[1], Alban Ferrier[1,2] and Olivier Guillot-Noël[1,*]
[1]*Institut de Recherche de Chimie Paris, CNRS-Chimie, ParisTech, Paris, France*
[2]*Sorbonne Universités, UPMC Univ Paris 06, Paris, France*

Chapter Outline

1 INTRODUCTION

Information in digital form is at the heart of nowadays societies, playing a major role in world-scale organizations down to many individual daily activities. Although technology made extraordinary progresses in terms of communication speed and capacity, data storage, or processing power, most of the

[*]In memoriam

Handbook on the Physics and Chemistry of Rare Earths, Vol. 46. http://dx.doi.org/10.1016/B978-0-444-63260-9.00267-4

fundamental concepts of information science were established in the beginning of the twentieth century. In 1984, a quantum algorithm was discovered by Bennett and Brassard for encrypted data exchange (Bennett and Brassard, 1984) and in 1985, Deutsch pioneered quantum computing theory (Deutsch, 1985). This was the start of quantum information processing (QIP), which is currently a major research topic in physics, computer science, mathematics, and material science. Quantum information is a new paradigm, where the classical bits, which can take only discrete values, are replaced by quantum bits, called qubits, which can assume any superposition state. This fundamentally new resource allows data processing, storage, and communication in ways impossible to achieve with classical systems (Kimble, 2008; Nielsen and Chuang, 2000; Stolze and Suter, 2008).

QIP is however very demanding on physical systems and its development has triggered important advances in quantum system control and design. In turn, QIP theory has emerged as a unified way to describe the behavior of these systems, independently of the details of their nature, structure, or interactions. QIP uses superposition states, which exist for a significant duration only in isolated systems. Interactions with a fluctuating environment, with many degrees of freedom, destroy them. Examples of quantum systems suitable for QIP are photons (Gisin and Thew, 2007; Kok et al., 2007) and nuclear spins (Chuang et al., 1998; Morton et al., 2008), which can have very low interactions with surrounding electromagnetic fields and atoms. QIP is also investigated in many other systems (Ladd et al., 2010; Lvovsky et al., 2009) such as trapped ions (Blatt and Roos, 2012), superconductors (Clarke and Wilhelm, 2008), electronic and nuclear spins in insulators and semiconductors (Hanson et al., 2007; Wrachtrup and Jelezko, 2006), and ultracold atoms (Bloch et al., 2012; Chanelière et al., 2005). As light is an excellent carrier of quantum information, as it is of classical one, there is also a need to interface it to material systems to store and process information (Northup and Blatt, 2014). Moreover, progress in lasers has also set them as efficient devices for controlling efficiently and accurately quantum systems. In these respects, rare earth (R)-doped crystals have very favorable spectroscopic properties among solid-state systems. The main one is to exhibit extremely narrow optical transitions, equivalent to long-lived superposition states, at cryogenic temperatures (Macfarlane, 2002). Depending on the R ions considered, these transitions span the entire visible and infrared range, including the telecom window at 1.5 μm. Moreover, many R ions have isotopes with nonzero nuclear spins, which can be therefore optically controlled or interfaced with photonic qubits. Finally, R-doped crystals are generally very robust, photostable materials, which can be readily cooled down to liquid helium temperatures in closed cycle cryostats. Their synthesis and spectroscopy have been widely developed for applications in photoluminescence, lasers, scintillation, etc. In addition, these materials are studied for classical information

or signal processing, which shares some requirements and schemes with QIP applications (Le Gouët et al., 2006; Li et al., 2008; Thorpe et al., 2011).

In this chapter, we review the applications of R-doped crystals to two specific QIP applications: optical quantum memories and quantum computing. After a brief introduction to QIP, we describe coherent light-atom interactions, which allow creating and controlling atomic quantum states. The spectroscopic properties of R-doped crystals are discussed afterward, with a focus on the specific features used in QIP. Finally, the concepts and studies related to quantum memories and computing are presented. In the two last sections, we chose to emphasize a few representative experiments, underlining important points, rather than to give extensive lists of results. As this field is relatively new to the rare-earth community, we felt that this approach could be more useful for the reader.

2 QUANTUM INFORMATION PROCESSING

2.1 Qubits and Gates

The reader is referred to Nielsen and Chuang (2000) or Stolze and Suter (2008) for a detailed presentation of QIP. In the following, we only review the basic concepts of the field. The qubit, or quantum bit, is the elementary unit of information in QIP. It is the equivalent of the bit in classical computing and communication. The bit can take two values, 0 or 1, and is implemented as different states of a capacitor, a transistor or of a light beam. The qubit is a quantum two-level system (TLS), as depicted in Fig. 1, with eigenstates labeled as $|0\rangle$ and $|1\rangle$ and representing the binary 0 and 1 values. However, in contrast to the classical bit, the qubit can also be in an arbitrary superposition state, which can be expressed as:

$$|\psi\rangle = \cos(\theta/2)|0\rangle + e^{i\phi}\sin(\theta/2)|1\rangle \tag{1}$$

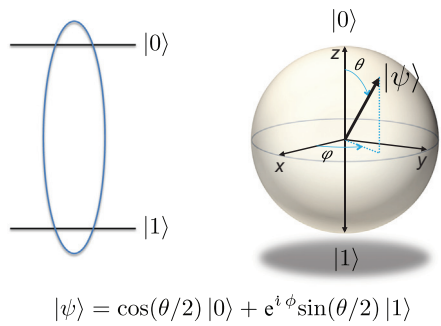

FIGURE 1 A qubit in a superposition state $|\psi\rangle$. Left: ladder-style drawing. The superposition is denoted by an ellipsoid. Right: position of the vector corresponding to $|\psi\rangle$ on the Bloch sphere.

up to a global $e^{i\delta}$ phase factor, since $|\psi\rangle$ and $e^{i\delta}|\psi\rangle$ are equivalent wavefunctions. This property opens the way to data processing and transmission that are impossible to achieve with a classical system, as discussed in Sections 2.2 and 2.3. Superposition states can be visually represented as vectors, which have their origin on a center of a sphere of radius 1 (the Bloch sphere) and their extremity lying on its surface (we normalize all quantum states to 1). When the qubit state is written as in Eq. (1), the angles θ and ϕ correspond to the spherical coordinates of the vector on the sphere (Fig. 1). Thus, the states $|0\rangle$ and $|1\rangle$ point, respectively, to the north and south poles. The $(|0\rangle + |1\rangle)/\sqrt{2}$ state is located on the equatorial plane along the x-axis and $(|0\rangle + i|1\rangle)/\sqrt{2}$ along y. It is important to note that although the qubit can assume an infinity of different states, the only states which can be identified with certainty are $|0\rangle$ and $|1\rangle$, if these states form the measurement basis. A major challenge in QIP is therefore to be able to use superposition states for improved performances, while determining final states with certainty or at least high probability. This is required to get meaningful calculation results or reliable data transmission. Another difficulty is the high sensitivity of superposition states to perturbations, which implies the use of isolated systems, while at the same time, these states should be controlled and read out, which requires some interactions with the environment. Atoms in vapors, photons, or nuclear spins are examples of systems in which superposition states can be long lived and accurately controlled, and are therefore good candidates for qubits (Ladd et al., 2010; Lvovsky et al., 2009). The lifetime of superposition states is related to the so-called coherence lifetime, which is described in more details in Section 3.2.

Atomic qubit states are controlled and read by interactions with electromagnetic fields. These interactions are theoretically represented by operators acting in the Hilbert space of the qubit. In classical information processing, all possible operations on bits are obtained by logical gates, like NOT, which changes 1 in 0 and vice versa. The same situation occurs in QIP, where gates are a set of operators. As an example, the equivalent of the classical NOT gate is the Pauli operator X, which representation in the $(|0\rangle, |1\rangle)$ basis is given in Fig. 2. This operator has the same effect as the classical NOT gate on $|0\rangle$ and $|1\rangle$, i.e., $X|0\rangle = |1\rangle$ and $X|1\rangle = |0\rangle$. However, X can also be applied to superposition states: $X(|0\rangle + i|1\rangle)/\sqrt{2} = (|1\rangle + i|0\rangle)/\sqrt{2}$. The corresponding trajectory on the Bloch sphere is shown in Fig. 2.

Although single qubits can represent a resource large enough to perform tasks unattainable with classical systems, as in quantum communication (Section 2.3), it is often necessary to consider multi-qubit systems. First, they are necessary to create larger superposition states. For example, with two qubits labeled a and b, the state $|\phi\rangle = (|0_a 0_b\rangle + |0_a 1_b\rangle + |1_a 0_b\rangle + |1_a 1_b\rangle)/2$ can be obtained. It contains all possible two-digit binary values, allowing parallel processing (Section 2.2). Another important feature of multi-qubit states is called "entanglement." This highly nonclassical property is among the most

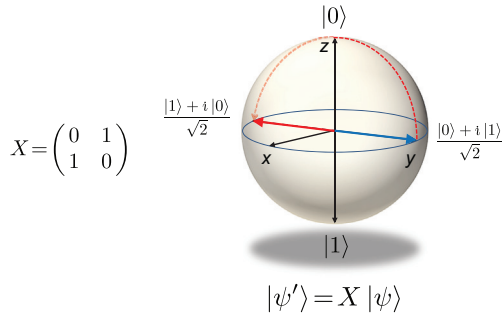

FIGURE 2 Left: representation of the Pauli X operator in the $(|0\rangle, |1\rangle)$ basis. X corresponds to the classical NOT gate. Right: Bloch sphere showing qubit states $|\psi\rangle = (|0\rangle + i|1\rangle)/\sqrt{2}$ and the trajectory leading to $|\psi'\rangle = X|\psi\rangle = (i|0\rangle + |1\rangle)/\sqrt{2}$.

amazing predicted by quantum mechanics and is often considered as the hallmark of "true" quantum systems. Entanglement refers to global states which cannot be separated into individual qubit states. The two-qubit state $|\phi\rangle$ defined above is equal to $|\phi\rangle = (|0_a\rangle + |1_a\rangle)(|0_b\rangle + |1_b\rangle)/2$ and is therefore not entangled, whereas $|\phi'\rangle = (|0_a 0_b\rangle + |1_a 1_b\rangle)/\sqrt{2}$ is an entangled state because it cannot be written as a product of the form $|\psi_a\rangle|\psi_b\rangle$. The main property of entangled states are the correlations which appear between measurements performed on the qubits, even when they are separated by large distances. For example, $|0\rangle$ and $|1\rangle$ can represent two orthogonal linear polarizations of a photon. Once the entangled state $|\phi'\rangle$ is created, the photons can travel in different directions and be detected after some delay. If a horizontal (vertical) polarization is measured on one photon, a subsequent measurement on the other one will result in a horizontal (vertical) polarization too. This is due to the entangled character of $|\phi'\rangle$, which forces the photon states to be completely linked. Because they enable correlations at a distance, entangled states are especially useful in quantum communications (Section 2.3).

2.2 Quantum Computing

Quantum computing aims at outperforming classical computers for some specific calculations. It relies on the additional resource given by the qubit superposition states, which can be used to design more efficient algorithms (Nielsen and Chuang, 2000). The quantum computer applies a series of gates to an ensemble of qubits, much like the classical computer operates on bits. However, for each different input, a classical computer must run again, whereas the quantum computer can directly process states which contain different inputs. As an example, instead of separately treating binary numbers 00, 01, 10, 11, a two-qubit quantum computer can take as an input $|\phi\rangle = (|00\rangle + |01\rangle + |10\rangle + |11\rangle)/2$ and apply gates to this state to perform a calculation. In this way, a quantum computer implements a highly parallel

computing flow. However, as already mentioned, the final state of each qubit on which the result of the calculation is read has to be determined with a very high probability and therefore be very close to $|0\rangle$ or $|1\rangle$. Typical problems of interest are those for which classical algorithms' running time depends exponentially on the size of the numbers to process. A suitable algorithm running on a quantum computer may be able to perform such calculation in a time depending only polynomially on the number size. Finding quantum algorithms turns out to be very difficult and only a handful of them have been discovered for useful tasks, like factoring into prime numbers (Shor, 1994), quantum error correction (Shor, 1996), and search into unclassified databases (Grover, 1997). Another area in which quantum computers can be used is simulation. On a classical computer, simulating even a few 10s interacting quantum systems requires a huge amount of processing power and memory. This is due to the dimension of the total Hilbert space available for the quantum states. On the other hand, an ensemble of qubits does not have this limitation and, if properly controlled to mimic systems and their interactions, can produce accurate simulations. Systems and algorithms for performing quantum simulations are currently actively investigated (Cirac and Zoller, 2012), partly because their requirements are lower than those for quantum computers, which have to be able to run arbitrary operations.

Ensembles of qubits suitable for a quantum computer are very difficult to obtain. First, the lifetime of the qubit's superposition states must be long compared to the time needed to apply a gate. Therefore, the qubit has to be well isolated from environment perturbations, while still allowing control by external fields. However, the superposition state lifetimes do not need to be as long as the total computing time, as algorithms for quantum error corrections exist. Second, in addition to gates applied to single qubits, calculations involve gates that change some qubit states depending on the state of other qubits. They are similar to classical logical operations like AND. These gates can only be obtained by controlled interactions between qubits. All calculations can be performed if (1) any one-qubit gate can be applied to each qubit and (2) a specific two-qubit gate can be applied to each pair of qubits. The most common two-qubit gate is the control-not gate, *CNOT*. Applied to a pair of qubits, called control and target, the gate changes the target state from $|0\rangle$ to $|1\rangle$ and vice versa only if the control qubit is in state $|1\rangle$. Otherwise, the target qubit is left unchanged. Again CNOT can be applied to qubits in superposition states and its representation in the $(|00\rangle,|01\rangle,|10\rangle,|11\rangle)$ base is:

$$\mathrm{CNOT} = \begin{pmatrix} 1 & 0 & 0 & 0 \\ 0 & 1 & 0 & 0 \\ 0 & 0 & 0 & 1 \\ 0 & 0 & 1 & 0 \end{pmatrix}. \tag{2}$$

Finally, a useful quantum computer must be able to treat large numbers or databases and therefore must contain many qubits. Obtaining gates for all

pairs of qubits is especially challenging in this case, as well as being able to separately control each qubit. DiVincenzo has summarized the required properties of a physical system in order to build a quantum computer in five criteria (DiVincenzo, 2000). For convenience, they are given in Section 6 together with the specific schemes developed for rare earth-doped crystals.

Current systems investigated for quantum computing are still limited to about 10 qubits (Monz et al., 2011). While able to run some quantum algorithms, their usefulness as computers is quite limited. A commercial quantum simulation device consisting in hundreds of superconducting qubits and able to find the ground state of interacting spins has also been recently developed (Johnson et al., 2011). The quantum nature of the calculation performed by this system is however still under study (Boixo et al., 2014).

2.3 Quantum Communication

Quantum communications use photons to transmit qubits between remote places. This is because photons are very well isolated from perturbations, which translates into long-lived superposition states for photonic qubits. Moreover, they can propagate with low attenuation (down to 0.2 dB/km at 1.55 μm) in optical fibers. They are therefore ideal "flying" qubits. Quantum communications could be used to connect quantum computers to build a quantum network (Kimble, 2008). This could increase the total computing power, especially if only processors with a few qubits are available at each network node. The most advanced application of quantum communication, and in fact of QIP in general, is however in security.

Quantum cryptography originates in the BB84 exchange protocol (Bennett and Brassard, 1984) for which quantum mechanics laws ensure a completely secure encrypted data transmission. BB84 is based on the exchange and read out of single photonic qubits in superposition states. The security is given by the fact that eavesdropping would require measuring these qubits, which will give only partial information on the qubit states and will moreover change them. The protocol is designed so that communicating parties can easily detect these changes and therefore abort compromised transmissions. BB84 therefore guarantees the secrecy of the communication based on a fundamental property of quantum systems. In this way, encryption keys can be exchanged without fearing interception by third parties and then used for sending secret messages over existing telecom fiber networks. Indeed, quantum cryptography is more accurately called quantum key distribution. It is a very attractive alternative to current encryption schemes, which use public keys. Those are very large numbers, which are very difficult to factor into prime numbers. Without this result, the encrypted messages are impossible to decipher. However, factoring large numbers has not been proven to be a fundamentally slow operation. A fast algorithm could be found, suddenly compromising past and present communications. Interestingly, this is

precisely what a quantum computer could do, if it could be built with enough qubits. In principle, this cannot happen with quantum key distribution, although developments in protocols and implementations are still needed to ensure very high security in real situations (Gisin and Thew, 2007; Gisin et al., 2002; Scarani et al., 2009). Another secure way to transmit data is based on quantum-state entanglement and teleportation (Bennett et al., 1993; Bouwmeester et al., 1997; Ekert, 1991). As shown in Fig. 3, an entangled pair of photons (qubits q1 and q2) is shared by the communicating parties (usually named Alice and Bob). The information that Alice wants to send to Bob is carried by a third photon (qubit q3) located at Alice's place. The quantum state of q3 is arbitrary. When Alice performs a joint measurement M on q1 and q3 photons, the state of Bob's photon is modified. This is due to the entanglement between q1 and q2. The result of Alice's measurement r (which is a simple number) is then communicated by a classical channel to Bob. With this information, Bob applies a gate U_r to q2, which changes its state to the original state of q3. Quantum-state teleportation has thus been achieved between Alice and Bob. This is highly secure because the qubit containing the information to be exchanged is never transmitted between Alice and Bob, whereas a potential eavesdropper cannot reconstruct q3 state by using r. Quantum cryptography based on commercial devices has been tested in a number of telecom fiber networks (Peev et al., 2009; Sasaki et al., 2011; Stucki et al., 2011). It has been demonstrated to work on distances over 250 km in low loss fibers (Stucki et al., 2009). Teleportation has also been achieved using telecom fibers (Marcikic et al., 2003), as well as in free space over 140 km (Ma et al., 2012).

One important limitation of quantum cryptography is the distance over which it can be used. Arbitrary quantum states cannot be copied, a property known as the no-cloning theorem. It is essential to the security of quantum cryptography but also prevents signal amplification to bridge long distances. To overcome this problem, quantum repeaters have been proposed (Briegel et al., 1998; Duan et al., 2001). They use quantum-state teleportation and measurements to propagate entanglement between photons at nodes separated

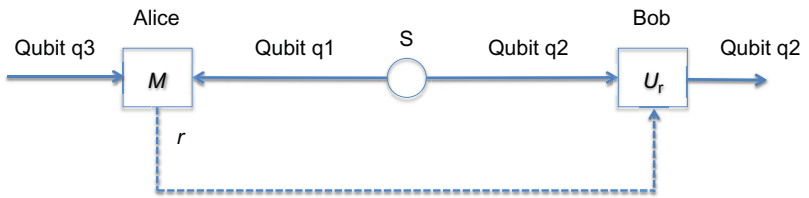

FIGURE 3 Quantum-state teleportation. Qubits q1 and q2, produced by the source S, are entangled and travel toward Alice and Bob. Alice wants to teleport the state of qubit q3 to Bob. She performs a joint measurement M on q1 and q3 and send the result r to Bob. According to r, Bob performs the gate U_r on q2, which is then in the same quantum state as was q3.

by increasing distances. Quantum repeaters use quantum memories, devices able to store and release a photonic qubit on demand, in order to achieve successful measurements and teleportations in different locations. Quantum memories have also applications in quantum computing based on linear optics, as well as in other QIP schemes, metrology, single-photon detection, and fundamental tests of quantum mechanics (Bussières et al., 2013; Lvovsky et al., 2009). Quantum memories are particularly promising applications for rare earth-doped crystals and are the subject of Section 5.

3 COHERENT LIGHT-ATOM INTERACTIONS

Coherent interactions occur between electromagnetic fields and atoms, when a well-defined phase relationship exists between the fields and the atomic wavefunctions. This topic was first studied in nuclear magnetic resonance (NMR) (Bloch, 1946; Rabi, 1937) and later extended to microwave and optical domains. Coherent interactions are used to control atomic qubits and to interface them with photonic qubits. This topic is therefore central to QIP and its main concepts are summarized below. Detailed treatments of light-matter interactions can be found in Allen and Eberly (1987) and Grynberg et al. (2010).

3.1 Quantum-State Control

Quantum-state control can be best understood in the semi-classical model. The atom is a two-level system, which we consider as a qubit, and is in resonant interaction with an oscillating electromagnetic field, like a laser beam. At time $t = 0$, the qubit is in state $|0\rangle$ and light is shone on the sample. At time t, in the approximation of resonant excitation, the qubit is in the state:

$$|\psi(t)\rangle = \cos\left(\frac{\Omega}{2}t\right)|0\rangle - \mathrm{i}\sin\left(\frac{\Omega}{2}t\right)\mathrm{e}^{\mathrm{i}(\omega_0 t+\phi)}|1\rangle, \tag{3}$$

which is completely defined by the exciting field. Ω, called the Rabi frequency, is proportional to the product of the absolute value of the transition matrix element, μ, by the field amplitude E_0, $\Omega = \mu E_0/\hbar$, where h is Planck's constant. The Rabi frequency measures the strength of the field-atom coupling. The transition frequency is ω_0 and the field is written as $E(t) = E_0\cos(\omega_0 t + \phi)$. Note that all frequencies in Eq. (3) are expressed in rad s^{-1}. The qubit state expressed by Eq. (3) is time dependent. For easier viewing of the qubit states, the Bloch sphere is then drawn with respect to a rotating frame at ω_0 frequency, corresponding formally to set $\omega_0 = 0$ in Eq. (3).

On the Bloch sphere, applying a light pulse to the qubit corresponds to a rotation around an axis in the equatorial plane. The axis angle relative to the x axis is given by the phase ϕ and the rotation angle by the product Ωt,

called the pulse area. For example, the state $(|0\rangle + |1\rangle)/\sqrt{2}$ can be obtained from $|0\rangle$ by a rotation of $\pi/2$ around the y axis (Fig. 4). For a given field amplitude, this corresponds to a pulse of duration $t = \pi/(2\Omega)$ with a phase $\phi = \pi/2$. This is called an $Y,\pi/2$ pulse. In the same way, an $X,\pi/2$ pulse is a $\pi/2$ rotation around x ($\phi = 0$) and applied to $|0\rangle$ gives $(|0\rangle - \mathrm{i}|1\rangle)/\sqrt{2}$. In practice, ϕ is at first arbitrary and has only a meaning when relative phases between successive pulses or states are considered. The first pulse applied to the qubit therefore defines the reference phase. Another important pulse is the X,π pulse, which implements the X gate (Fig. 2). A π pulse has a duration of π/Ω and therefore a spectral bandwidth $\approx \Omega/\pi$. The Rabi frequency (expressed in Hz) is therefore the approximate maximum transition width that the pulse can effectively address with an area of π and more generally gives the bandwidth over which coherent interactions can be performed.

When the exciting field is left continuous, the qubit final state describes a circle on the Bloch sphere, periodically reaching $|0\rangle$ and $|1\rangle$. The probability P_1 of the qubit to be in $|1\rangle$ oscillates as a function of time t:

$$P_1 = \sin^2\left(\frac{\Omega}{2}t\right). \tag{4}$$

This phenomenon is called a Rabi oscillation. Such a measurement is used, for example, to determine Ω and in turn allows applying pulses of known area.

Coherent light-matter interactions can be extended to the case of photonics qubits. For example, a single photon can create a superposition state in an atom or in an ensemble of atoms, and vice versa. This allows transferring quantum states between photonic and atomic qubits. An accurate description of these processes requires the quantization of the electromagnetic field, although several effects can be understood in the following way. The absorption of a single photon can be seen as the mapping of a photonic quantum state into an atomic superposition state on the Bloch sphere. This state can then be manipulated using the coherent light-atom interactions we just described.

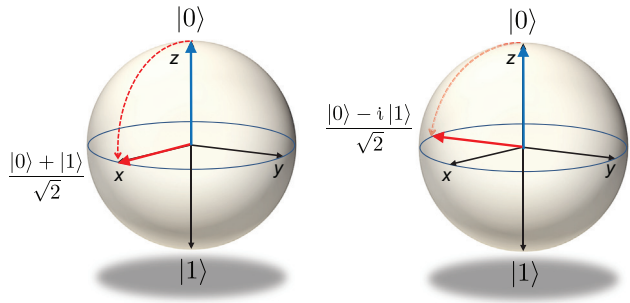

FIGURE 4 Left: a $Y,\pi/2$ pulse corresponds to a rotation of $\pi/2$ around the y axis in the Bloch sphere. It changes $|0\rangle$ into $(|0\rangle + |1\rangle)/\sqrt{2}$. Right: similarly, a $X,\pi/2$ pulse is a $\pi/2$ rotation around x. Applied to $|0\rangle$, it results in $(|0\rangle - \mathrm{i}|1\rangle)/\sqrt{2}$.

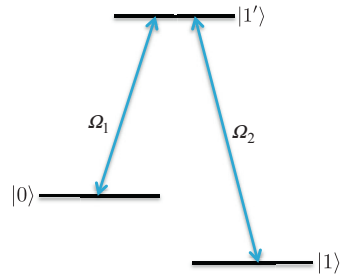

FIGURE 5 A Λ system between two nuclear spin ground-state levels $|0\rangle, |1\rangle$ and an optical excited level $|1'\rangle$. Ω_1 and Ω_2 denote the Rabi frequencies of the two optical transitions.

So far we discussed systems with only two levels. It is however often useful to use additional transitions. A common configuration is the so-called Λ-system, where two low-energy levels ($|0\rangle, |1\rangle$) are connected to an excited one ($|1'\rangle$), typically through two optical transitions (Fig. 5). This allows transferring quantum states between different transitions. As an example, let us assume that the superposition state $|\psi\rangle = (|0\rangle + |1'\rangle)/\sqrt{2}$ is created by applying a $\pi/2$ pulse to the $|0\rangle \leftrightarrow |1'\rangle$ transition. A π pulse is then applied to the $|1'\rangle$–$|1\rangle$ transition resulting in $|\psi'\rangle = (|0\rangle + |1\rangle)/\sqrt{2}$. The initial superposition state has been transferred to a new transition. Usually, $|0\rangle \leftrightarrow |1'\rangle$ is an optical transition able to map a photonic qubit or to be coherently controlled by a laser, but with relatively short-lived superposition states. To overcome this limitation, the quantum state is transferred to the $|0\rangle \leftrightarrow |1\rangle$ transition, which defines the main qubit. This qubit is typically a nuclear spin two-level system, which can maintain superposition states for long times. Such a state transfer therefore takes place across systems with energies differing by seven to eight orders of magnitude and takes advantage of both optical and nuclear spin transitions. An important point for finding a Λ system is that both optical Rabi frequencies Ω_1 and Ω_2 should be large for efficient transfers.

3.2 Coherence and Relaxations

In this section, we consider an atom with only two electronic levels. To get a qualitative understanding of its behavior, it is enough to reduce it to an electric dipole. Superposition states of the atom are equivalent to oscillations of the dipole at the frequency of the transition. These oscillations cause the atom to emit light. If an ensemble of these atoms have identical transition frequencies and oscillate in phase, light emitted by each atom will constructively interfere and give rise to a macroscopic coherent light field called the polarization. However, each dipole can be perturbed by fluctuations in its environment. They can change the atom transition energy and therefore the dipole oscillating frequency. This results in a dephasing between the dipole emissions and a decay of the polarization. Moreover, because the dipoles are

emitting light, or other nonradiative loss channels are present, atoms relax to the ground state, with a characteristic time T_1, which is the excited-state lifetime. The coherence lifetime T_2 describes the polarization decay and takes into account both dephasing and population relaxation. As all atoms are assumed to have the same average frequency, the linewidth of the macroscopic emission is called homogeneous and denoted by Γ_h. It is related by Fourier transform to the decay rates by:

$$\Gamma_h = \frac{1}{\pi T_2} = \frac{1}{2\pi T_1} + \frac{1}{\pi T_{2,d}}, \tag{5}$$

where $T_{2,d}$ corresponds to pure dephasing processes.

A fundamental point is that coherent light-atom interactions can accurately create and control superposition states only in the absence of random perturbations. They can therefore only occur during a time τ for which the coherence decay is negligible, i.e., $\tau \ll T_2$, using a laser with a linewidth much lower than Γ_h. In the same way, useful information can be retrieved from a qubit superposition state only for times much shorter than T_2. The coherence lifetime is therefore a key parameter for designing QIP systems.

Until now, the atoms in the ensemble were assumed to have the same average transition frequency. We now consider the case where transitions are spread over a frequency range. This corresponds to an inhomogeneous broadening Γ_{inh}, which we assume to be much larger than the homogeneous one, $\Gamma_{inh} \gg \Gamma_h$ (Fig. 6). If this ensemble of atoms is initially oscillating coherently, the frequency differences corresponding to Γ_{inh} will induce a dephasing between each atom emission and therefore a decay of the macroscopic polarization with a rate equals to $1/(\pi\Gamma_{inh})$. This effect is called the free-induction decay. Since $\Gamma_{inh} \gg \Gamma_h$, the decay rate of the macroscopic polarization is much larger than the coherence lifetime of each atom transition. Thus, although each dipole is still oscillating in a perfectly well-defined way, no coherent emission can be observed from the ensemble. Fortunately, such an

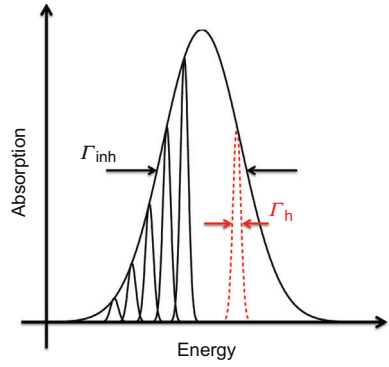

FIGURE 6 Inhomogeneous (solid line) and homogeneous (dotted line) linewidths.

emission can be retrieved by the echo phenomenon, introduced by Hahn for spins (Hahn, 1950), and later extended in the optical domain (Abella et al., 1966).

The two-pulse echo sequence starts with a $\pi/2$ pulse which excites the atoms in the ground state ($|1\rangle$ in this example) to a superposition state in the Bloch sphere equatorial plane (Fig. 7). The pulse is resonant with atoms within a bandwidth $\Delta\omega$ around a central frequency ω_0. As discussed above, the macroscopic polarization of the atom ensemble decays by FID after the pulse with a rate $\approx 1/\Delta\omega$. In the Bloch sphere, the vectors corresponding to the atoms with a frequency different from ω_0 start to rotate with respect to the axis frame (which is rotating itself at a frequency ω_0). This is shown in Fig. 7 as a spreading fan. After a delay τ, a π pulse is applied to the atoms, which in the Bloch sphere corresponds to a π rotation, causing the vectors to rephase, i.e., to gather instead of spreading apart (Fig. 7). At a delay τ after the π pulse, all vectors are again aligned, which corresponds to in-phase oscillations and therefore to a macroscopic polarization. The resulting emission is called an echo. This process can also be described by the evolution of the relative phase ϕ of the superposition states. For a given atom with a transition frequency $\omega_0 + \omega$, $\phi(t) = \omega t$ for $t \leq \tau$. The π pulse reverses the phase evolution and $\phi(t) = \omega\tau - \omega(t - \tau)$ for $\tau \leq t \leq 2\tau$. The macroscopic polarization intensity emitted by the sample is proportional to:

$$\left| \int_{-\Delta\omega/2}^{\Delta\omega/2} e^{i\phi(t,\omega)} d\omega \right|^2 = \left| \int_{-\Delta\omega/2}^{\Delta\omega/2} e^{i[\omega\tau - \omega(t-\tau)]} d\omega \right|^2. \quad (6)$$

The integral vanishes unless the argument of the exponential is independent of ω, which happens at $t = 2\tau$ and corresponds to the echo emission. As the time τ is increased, the echo intensity decays, because more and more atoms are perturbed during the total evolution time 2τ. These atoms cannot emit in phase with unperturbed atoms and do not contribute to the echo emission.

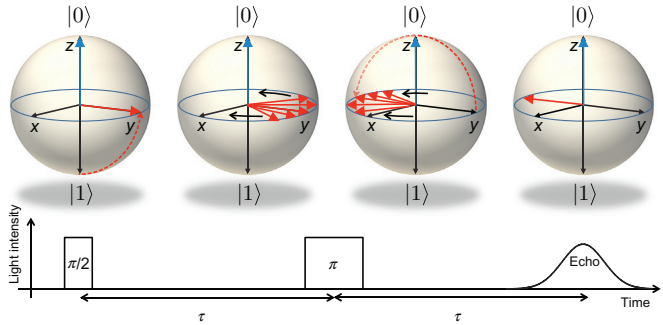

FIGURE 7 The two-pulse echo sequence. Bloch vectors' evolution is shown above the $\pi/2$, π and echo pulses, which are separated by a delay τ.

The echo intensity I_{echo} decays as a function of the delay τ between the $\pi/2$ and π pulses as:

$$I_{echo}(\tau) = \exp\left(-\frac{4\tau}{T_2}\right) \tag{7}$$

and is a convenient way to measure T_2.

4 RARE EARTH-DOPED CRYSTALS

Many spectroscopic properties are important for using an R-doped crystal in QIP. In this section, we will mainly discuss the most specific ones, which are usually not relevant for applications in photoluminescence, lasers, scintillators, etc. We start with an overview of the topic with the example of Pr^{3+}:$La_2(WO_4)_3$, before going into more details. Spectroscopic data for crystals used in QIP experiments are given at the end of the section.

The first step is to identify an optical transition suitable for coherent interactions. Its wavelength should correspond to a narrow linewidth laser emission, and its coherence lifetime and oscillator strength should be large enough to apply a π pulse in a time much shorter than T_2. In this example, the selected transition takes place between the lower energy levels of the ground multiplet ($^3H_4$) and an excited one ($^1D_2$) and is located at 16,590.9 cm^{-1} (602.74 nm in vacuum). Dye lasers with linewidths < 1 kHz are available at this wavelength. At a Pr^{3+} doping level of 1.4 at.%, the maximum transition oscillator strength for light propagating along the crystal b axis is $f \approx 2 \times 10^{-8}$. The peak absorption coefficient, $\alpha = 14.7$ cm^{-1}, is also relevant for narrow laser excitation. It depends, for a given f, on the inhomogeneous broadening of the line, which is $\Gamma_{inh} = 18.8$ GHz (0.023 nm) in this crystal (Section 4.2). These absorption experiments require high resolution and can be performed by scanning a narrow laser. Knowing the oscillator strength, the Rabi frequency can be calculated for a given laser intensity and can reach about $2\pi \times 1$ MHz, corresponding to a π pulse of about 0.5 μs. Optical coherence lifetime, determined by photon echo, is $T_2 = 11$ μs at 3 K, and is about 20 times larger than achievable π pulses. The corresponding homogeneous linewidth is $\Gamma_h = 29$ kHz, nearly six orders of magnitude lower than Γ_{inh}. The excited-state population lifetime is 11.5 μs, giving a contribution to Γ_h of 14 kHz (Section 4.3). These parameters allow designing coherent control schemes of this transition and using it as a qubit. However, ground-state nuclear spin transitions can exhibit longer T_2 and are often preferred to optical ones.

Pr^{3+} has a single isotope with $I = 5/2$ for which hyperfine structures have first to be determined (Section 4.1). This can be achieved by spectral tailoring, resulting in the energy scheme shown in Figs. 8 and 15. Note that the hyperfine splittings are on the order of 10 MHz, three orders of magnitude lower than the optical inhomogeneous linewidth and therefore cannot be seen in

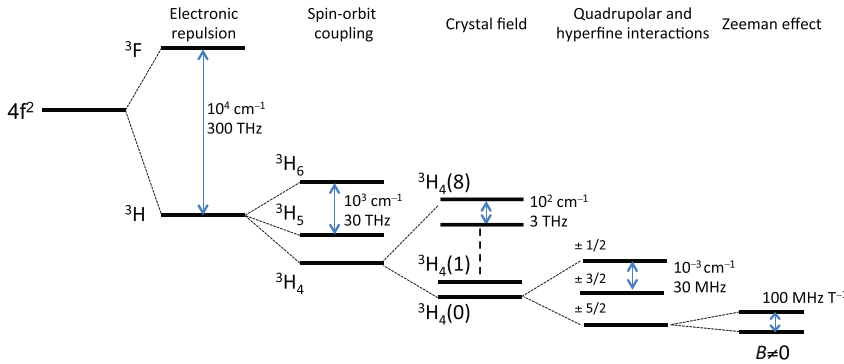

FIGURE 8 Interactions and partial energy-level scheme for Pr^{3+} ($I = 5/2$). The degeneracy of the hyperfine levels $\pm m_I$ is lifted by an external magnetic field ($B \neq 0$).

optical absorption. To be able to optically control the ground-state transitions, oscillator strengths between hyperfine levels of the ground and excited states should be measured using, for example, spectral tailoring. Other properties to be determined are the hyperfine inhomogeneous linewidths (Section 4.2) as well as population and coherence lifetimes (Section 4.3). This can be achieved by optically detected NMR. In Pr^{3+}:$La_2(WO_4)_3$, ground-state $\Gamma_{inh}^{hf} \approx 100$ kHz, $T_1^{hf} = 16$ s, and $T_2^{hf} = 250$ μs. External magnetic fields can also be very useful, for example to modify hyperfine wavefunctions and transitions strengths (Section 4.1.3) or to increase coherence lifetimes (Section 4.3.4). This requires to precisely determine spin Hamiltonians by measuring hyperfine structures under varying magnetic fields (Section 4.1.4). T_2^{hf} can then be increased by several orders of magnitude by decoupling the transitions from host magnetic fluctuations, leading to coherence lifetimes up to $T_2^{hf} = 158$ ms in Pr^{3+}:$La_2(WO_4)_3$. Another technique to extend T_2^{hf} consists in applying a series of π pulses to a hyperfine transition, which also results in a decoupling from environment fluctuations and leads to $T_2^{hf} = 4.2$ ms (Section 4.3.4).

4.1 Electronic and Spin Level Structure

In this section, the energy level structure of R ions is discussed in the context of QIP. This is a quite large topic involving several aspects, e.g.:

- optical transition wavelengths and intensities determine how qubits can be controlled by light as well as the efficiency of quantum state transfer between photonic and atomic qubits.
- nuclear spin (hyperfine) levels can be used to define ground-state qubits with long coherence lifetime.
- optical control of nuclear spin qubits requires Λ systems between hyperfine levels of ground and excited states (Fig. 5). The intensity of the Λ

system optical transitions depends on the nuclear spin wavefunctions, which can be modified by applying a specific external magnetic field.
- external magnetic fields can split and shift levels to obtain optical or spin transitions insensitive to small magnetic field fluctuations. This can have huge effects on transition coherence lifetimes.

4.1.1 Theory

The transitions used in R-based QIP mainly take place within the $4f^N$ configurations of trivalent R ions. Their electronic structure is $[Xe]4f^N$ in which the 4f orbitals have a smaller radial extension than the filled $5s^2$ and $5p^6$ shells. They are therefore shielded from surrounding electric fields, and level energies are mainly determined by the free ion interactions. Electronic repulsion and spin-orbit coupling are of the same order of magnitude and result in multiplets labeled in the Russell-Saunders scheme: $^{2S+1}L_J$. S, L quantum numbers represent however only the dominant wavefunction component and should generally not be considered as good quantum numbers. Inserted in a host, the multiplets split under the crystal field (CF) created by the surrounding ions. In the following, the CF levels are labeled $^{2S+1}L_J(n)$, $n = 0$ corresponding to the lowest energy level of the multiplet. In a few cases, like Eu^{3+} ^7F_J levels, the CF significantly mixes levels of different J. Depending on the site symmetry, the J degeneracy can be lifted to various degrees. However, energy levels of R ions with an odd number of electrons, the so-called Kramers ions, retain at least a twofold degeneracy in zero external magnetic field. The CF is also involved in f–f transitions intensities by mixing the $4f^N$ configuration with others of opposite parity. These properties, which are essential to the fields of R luminescence, have been extensively reviewed in the past (Görller-Walrand and Binnemans, 1996; Henderson and Imbush, 1989; Hufner, 1978; Jacquier and Liu, 2005; Peacock, 1975) and will not be further developed here. We instead focus on more specific points: nuclear spin structures and the effects of external magnetic fields.

A scheme of the energy levels for Pr^{3+} is shown in Fig. 8. As can be seen from the energy scales, the hyperfine structure is about five orders of magnitude smaller than the CF splittings. It can be therefore treated by a perturbation approach, which leads to the so-called spin Hamiltonian modeling (Liu, 2005; Macfarlane and Shelby, 1987a). The general $4f^N$ level structure is modeled by the following Hamiltonian:

$$\mathcal{H} = [\mathcal{H}_{FI} + \mathcal{H}_{CF}] + [\mathcal{H}_{HF} + \mathcal{H}_{Q} + \mathcal{H}_{Z} + \mathcal{H}_{z}], \tag{8}$$

where $\mathcal{H}_{FI}$ is the free ion Hamiltonian, which includes spin-orbit coupling, electronic repulsion as well as the central field Hamiltonian, and $\mathcal{H}_{CF}$ is the CF Hamiltonian. The second bracket gathers the spin and magnetic terms: hyperfine ($\mathcal{H}_{HF}$) and quadrupolar ($\mathcal{H}_{Q}$) interactions, and electronic ($\mathcal{H}_{Z}$) and nuclear ($\mathcal{H}_{z}$) Zeeman effects. $\mathcal{H}_{Q}$ vanishes for nuclear spin $I \leq 1/2$

and the two last terms appear only when an external magnetic field $\boldsymbol{B}$ is applied. The spin Hamiltonian expresses the operators in the second bracket for a singlet or a doublet in a given S, L, J multiplet, which is assumed to be pure, i.e., L, S mixing by the spin-orbit coupling and J mixing by the CF are neglected. Perturbation calculations are also restricted to the S, L, J multiplet of interest. In the following, we discuss the application of the spin Hamiltonian to two types of levels:

1. a singlet CF level of a non-Kramers ion (i.e., an even number of f electrons). For these ions, all CF levels in triclinic (C_1), monoclinic (C_s, C_2), and orthorhombic (C_{2v} and D_2) site symmetries are singlets.
2. a CF doublet of a Kramers ion. For these ions, CF levels are doublets in all site symmetries except cubic ones.

In case 1, first-order electronic Zeeman and hyperfine effects vanish, and the second-order spin Hamiltonian reads (Macfarlane and Shelby, 1987a):

$$\begin{aligned}\mathcal{H}_S = &-g_J^2\mu_B^2\boldsymbol{B}\cdot\Lambda\cdot\boldsymbol{B} - 2A_J g_J\mu_B\boldsymbol{B}\cdot\Lambda\cdot\boldsymbol{I} - \gamma_n\boldsymbol{B}\boldsymbol{I} - A_J^2\boldsymbol{I}\cdot\Lambda\cdot\boldsymbol{I} \\ &+ P\left[I_{z'}^2 - \frac{1}{3}I^2 + \frac{1}{3}\eta\left(I_{x'}^2 - I_{y'}^2\right)\right]\end{aligned} \tag{9}$$

where g_J is the Landé g factor, μ_B the Bohr magneton, A_J the hyperfine coupling constant, and γ_n the nuclear gyromagnetic factor. Λ is a tensor given by:

$$\Lambda_{i,j} = \sum_{n' \neq n} \frac{\langle n|J_i|n'\rangle\langle n'|J_j|n\rangle}{E_{n'} - E_n}, \tag{10}$$

where i,j label the reference x,y,z axes, n, n' denote, respectively, the CF level of interest and the other ones in the J multiplet, and E_m is the energy of level m. P and η are the quadrupolar and asymmetry coupling constants. The x',y',z' axes are the principal axes of the quadrupolar interaction. The two last terms in Eq. (9) can always be combined by diagonalization in new axes (x'',y'',z'') and are expressed as:

$$\mathcal{H}'_Q = D\left(I_{z''}^2 - \frac{1}{3}I^2\right) + E\left(I_{x''}^2 - I_{y''}^2\right), \tag{11}$$

where the D and E parameters combine contributions from second-order hyperfine and quadrupolar interactions, and the asymmetry parameter is $3E/D$. In zero magnetic field, the $2I + 1$ hyperfine levels are doubly degenerate and labeled by the nuclear spin projections $\pm m_I$ along the z'' axis, assuming a small asymmetry factor. However, in triclinic and monoclinic site symmetries, the (x'',y'',z'') axes generally depend on the CF level and the m_I numbers may not be good enough to determine selection rules between hyperfine levels belonging to different CF levels.

The precise form of Eq. (9) depends on the site symmetry, which determines nonzero elements in tensors and the orientation of the principal axes.

For experimental determination of $\mathcal{H}_S$ parameters, it is convenient to rewrite Eq. (9) in terms of three symmetric tensors:

$$\mathcal{H}_S = \boldsymbol{B}\cdot Z\cdot\boldsymbol{B} + \boldsymbol{B}\cdot M\cdot\boldsymbol{I} + \boldsymbol{I}\cdot Q\cdot\boldsymbol{I} \tag{12}$$

where $Z = -g_J^2\mu_B^2\Lambda$. The gyromagnetic tensor $M = -2A_J g_J \mu_B \Lambda - \gamma_n$ has the same principal axes as Z. Q is defined as:

$$Q = R_Q \begin{pmatrix} E - \frac{1}{3}D & 0 & 0 \\ 0 & -E - \frac{1}{3}D & 0 \\ 0 & 0 & \frac{2}{3}D \end{pmatrix} R_Q^T, \tag{13}$$

where R_Q is the rotation matrix relating $\mathcal{H}_Q$ principal axes to the reference ones. In C_1 symmetry, the Λ tensor has six independent and nonzero elements. To determine Z (which does not contribute to hyperfine splittings), M, the three angles of the R_Q matrix and E, D, 12 parameters are needed. In C_s and C_2 symmetries, the CF z axis is common to all tensors (eight parameters in total to be determined) and in higher symmetries, the tensors are diagonal with respect to the CF axes (six parameters in total). In axial symmetries, the M and Z tensors have only two nonzero elements, corresponding to the magnetic field parallel or perpendicular to the z axis. Moreover, the asymmetric part of $\mathcal{H}_Q$ is zero ($E = 0$).

Calculation of the spin Hamiltonian parameters is also possible from CF wavefunctions (Erickson, 1985; Goldner and Guillot-Noël, 2004; Guillot-Noël et al., 2005, 2010). This is straightforward for the Zeeman and hyperfine parts, using the Λ tensor definition of Eq. (10). The quadrupolar interactions are given by more complex formula, as they involve contributions to the electric field gradient at the nucleus from the lattice ions and the 4f electrons (Erickson, 1986; Guillot-Noël et al., 2010; Hansen et al., 1997). Moreover, these contributions must be weighted by different screening coefficients, which take into account, for example, closed shells distortion by the lattice field (Sternheimer, 1966, 1967). It is also possible to compute directly $\mathcal{H}$ Eq. (8), without having to rely on the approximations leading to $\mathcal{H}_S$. This approach, however, requires diagonalization of large matrices once the nuclear spin wavefunctions are added to the electronic ones. The relevant matrix elements are given in Guillot-Noël et al. (2005, 2010).

Kramers ions doublets, with splittings much smaller than the CF ones, can be described by an effective 1/2 spin operator $\boldsymbol{S}$. The spin Hamiltonian reads (Macfarlane and Shelby, 1987a):

$$\begin{aligned} H_S = \; & \mu_B \boldsymbol{B}\cdot g\cdot\boldsymbol{S} + \boldsymbol{I}\cdot A\cdot\boldsymbol{S} + P\left[I_{z'}^2 - \frac{1}{3}I^2 + \frac{1}{3}\eta\left(I_{x'}^2 - I_{y'}^2\right)\right] \\ & -\gamma_n \boldsymbol{B}\boldsymbol{I} - g_J^2\mu_B^2 \boldsymbol{B}\cdot\Lambda\cdot\boldsymbol{B} - 2A_J g_J \mu_B \boldsymbol{B}\cdot\Lambda\cdot\boldsymbol{I} \\ & -A_J^2 \boldsymbol{I}\cdot\Lambda\cdot\boldsymbol{I}, \end{aligned} \tag{14}$$

where g is the effective electronic Zeeman tensor, A the effective hyperfine tensor, P, η, and x',y',z' correspond to the quadrupolar interaction as in Eq. (9) and γ_n is the nuclear gyromagnetic ratio. The first three terms are obtained by first-order perturbation, whereas the last three correspond to second-order terms, with the same definitions as in Eq. (9). It is also possible to rewrite Eq. (14) with five tensors:

$$H_{\text{eff}} = \mu_B \boldsymbol{B}\cdot g\cdot \boldsymbol{S} + \boldsymbol{I}\cdot A\cdot \boldsymbol{S} + \boldsymbol{I}\cdot Q\cdot \boldsymbol{I} + \boldsymbol{B}\cdot M\cdot \boldsymbol{I} + \boldsymbol{B}\cdot Z\cdot \boldsymbol{B}, \tag{15}$$

where Q, M, and Z are given above. Up to 24 independent and nonzero parameters have to be determined for C_1 site symmetry and 14 in axial ones. This can be very challenging and may be possible only by neglecting $\boldsymbol{I} \cdot Q \cdot \boldsymbol{I}$ or $-2A_J g_J \mu_B \boldsymbol{B} \cdot \Lambda \cdot \boldsymbol{I}$ (Guillot-Noël et al., 2006). The term $\boldsymbol{B} \cdot Z \cdot \boldsymbol{B}$ is also not contributing to hyperfine level splittings, but just to a global shift, and may not be relevant or experimentally accessible. One important point to emphasize is the high sensitivity of Kramers ions to magnetic field. As $\mu_B \approx 14$ GHz/T and g principal values can reach 10–15 (e.g., for Er^{3+} ground state (Macfarlane et al., 1991; Sun et al., 2008)), the Zeeman splitting can reach the cm^{-1} range with magnetic fields of a few T and become comparable with the CF splittings. In this case, the spin Hamiltonian approach cannot be applied anymore. Moreover, the effective site symmetry has to take into account the magnetic field direction and will be generally lower than the one at zero or low fields. On the other hand, at zero magnetic field, hyperfine and quadrupolar interactions can split the hyperfine structure of a Kramers doublet up to $2(2I + 1)$ levels. As in the case of non-Kramers ions, calculations of the spin Hamiltonian parameters or hyperfine structures can be performed from CF wavefunctions (Popova et al., 2000).

Hyperfine structures of doublets in non-Kramers ions have also been studied and modeled in several hosts (Chukalina et al., 1999; McLeod and Reid, 1997; Pytalev et al., 2012). Further discussion of hyperfine structure of R ions can also be found in Macfarlane and Shelby (1987a).

4.1.2 Experimental Techniques

Absorption

Absorption gives access to spin structures only when they are larger than the optical inhomogeneous linewidth Γ_{inh}, which is often of the order of a few GHz. Since $\mu_B = 14$ GHz/T, electronic Zeeman transitions can be observed by this technique, although relatively strong magnetic fields may have to be used (Sun et al., 2008). Figure 9 shows an absorption spectrum in Nd^{3+}:YVO_4 where the four transitions between the Zeeman split levels are clearly seen under a magnetic field of 310 mT (Afzelius et al., 2010a). The spectrum spans 0.17 nm and is obtained by monitoring the transmission of a 1 MHz linewidth laser. In a few cases, optical inhomogeneous linewidths are smaller than the hyperfine splittings (Agladze et al., 1991; Chukalina et al., 1999;

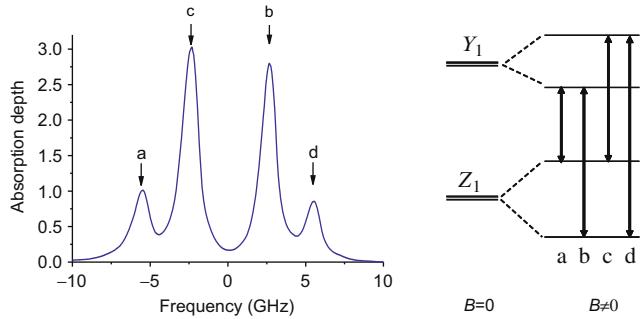

FIGURE 9 Absorption spectrum of Nd^{3+}:YVO_4 ($^4I_{9/2}(0)$ $[Z_1]\rightarrow{}^4F_{3/2}(0)$ $[Y_1]$ transition) under a magnetic field of 310 mT oriented at 45° from the *c*-axis (T=2.8 K). Under the magnetic field, the Kramers doublets split differently, resulting in four distinct transitions (Afzelius et al., 2010a).

Macfarlane et al., 1981, 1998; McLeod and Reid, 1997). In this case, hyperfine structures can also be resolved in absorption experiments. This is especially true with Kramers ions or doublets of non-Kramers ions, where the strong hyperfine interaction results in large splittings, and in halide hosts for which inhomogeneous linewidths can be small (Section 4.2). An example is given in Fig. 10, where the hyperfine structures of ground and excited states of ^{167}Er:^{7}$LiYF_4$ extend over several GHz, whereas the optical inhomogeneous linewidth is about 100 MHz (Macfarlane et al., 1992).

Electron paramagnetic resonance (EPR) of R Kramers ions is also very useful in determining ground-state hyperfine structures. Indeed, inhomogeneous linewidths in the microwave domain are much lower than in the optical one, and linewidths of only a few MHz can be observed at low R concentrations. This allows easy observation of the hyperfine transitions between the ground-state Zeeman levels. By varying the orientation of the crystal in the static magnetic field, one can determine the g, A, Q, M tensors of Eq. (15). An EPR spectrum on Er^{3+}:Y_2SiO_5 is shown in Fig. 11, where the hyperfine lines of $^{167}Er^{3+}$ (I = 7/2) are clearly seen. Although the site symmetry is C_1, the high quality of the spectra enabled a precise determination of the ground-state hyperfine and quadrupolar interactions (Guillot-Noël et al., 2006).

Spectral Holeburning and Tailoring

In many cases, however, hyperfine structures cannot be directly observed. This is the case for singlet levels of non-Kramers ions, for which the hyperfine structures are on the order of 10–100 MHz, too small to be observed by optical absorption. Several techniques can be used to overcome this problem. The simplest one is spectral hole burning, the principle of which is shown in Fig. 12 (Erickson, 1977; Macfarlane and Shelby, 1987a). The optical

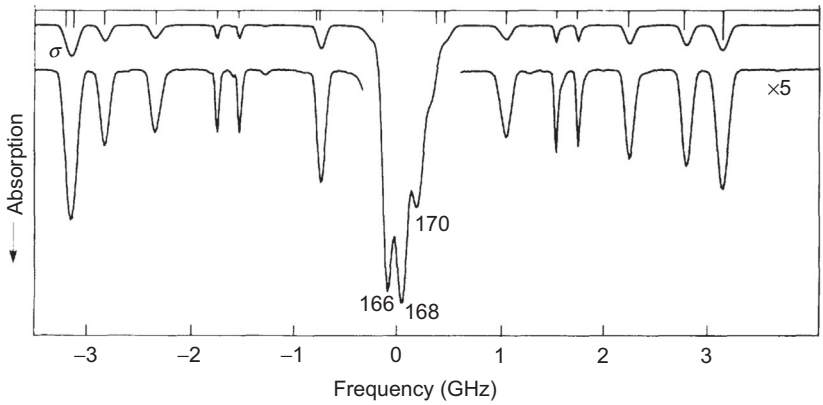

FIGURE 10 Absorption spectrum of Er^{3+}:$^{7}LiYF_4$ ($^{4}I_{15/2}(0) \rightarrow {}^{4}F_{9/2}(0)$ transition centered at 653.49 nm) at zero magnetic field and T=1.6 K. Er^{3+} concentration is ≈ 1 ppm. The central line corresponds to $^{166,168,170}Er^{3+}$ isotopes ($I = 0$) and the side lines to transitions between hyperfine levels of $^{167}Er^{3+}$ ($I = 7/2$). *Reproduced with permission from Macfarlane et al. (1992), © 1992 the American Physical Society (http:/dx.doi.org/10.1103/PhysRevLett.69.542).*

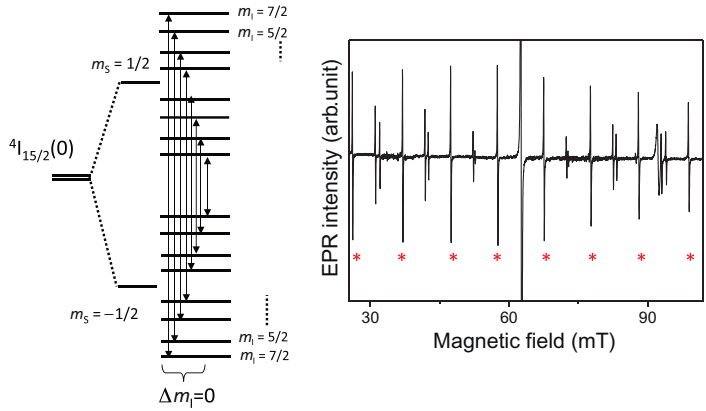

FIGURE 11 EPR spectrum of 0.005 at.% Er^{3+}:Y_2SiO_5 at T=7 K. The central line corresponds to $I = 0$ isotopes and lines denoted by a star to transitions between hyperfine levels of $^{167}Er^{3+}$ ($I = 7/2$) with $\Delta m_I = 0$. Corresponding energy levels and transition are shown on the left. The remaining lines satisfy $\Delta m_I = \pm 1$ and reflect the large quadrupolar interaction (Guillot-Noël et al., 2006).

transition has to be inhomogeneously broadened, i.e., consisting of an envelope of narrow homogeneously broadened lines (Fig. 6). For simplicity, we first assume that the ground state has only two hyperfine levels and the excited state only one. Initially, the ground-state levels are equally populated. When the transition is scanned with a narrow linewidth and low power laser, a smooth absorption profile is recorded (Fig. 12A). The laser is then tuned to

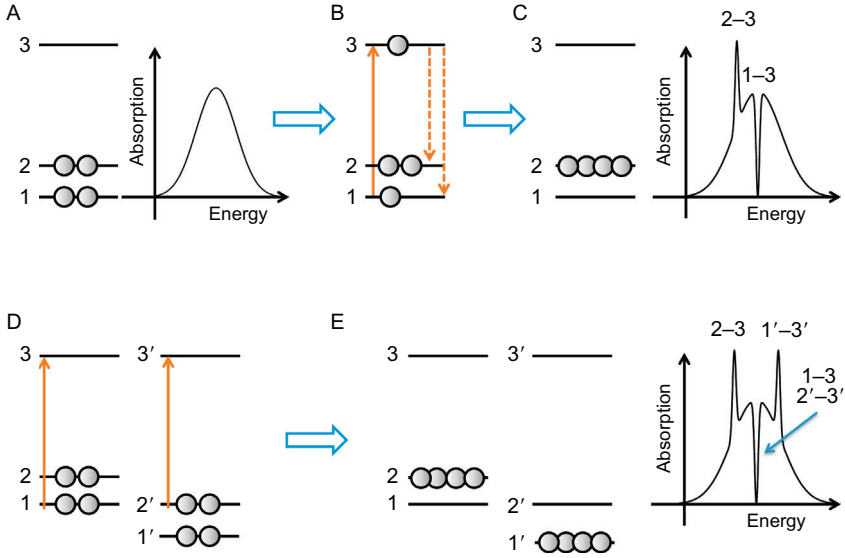

FIGURE 12 Principle of spectral hole burning. Upper and lower rows correspond to one or two classes of ions (see text for details).

the transition 1–3 for a particular class of ions to achieve optical pumping for a narrow part of inhomogeneous line (Fig. 12B). We consider the case where the 1–3 transition of these ions is at the center of the inhomogeneous line. In addition, ions excited into the upper level are assumed to relax equally to levels 1 and 2. Ions in level 2 cannot absorb light anymore, and if levels 1 and 2 have long enough lifetimes compared to level 3, all populations will be eventually "trapped" in level 2, which is the shelving level. If the transition is scanned again, a narrow hole, limited to twice the homogeneous linewidth, appears at the center of the inhomogeneous line, since level 1 is empty and no ions can absorb at the 1–3 frequency (Fig. 12C). Level 2 is also more populated than initially and accordingly, an increase in absorption appears at lower frequency, corresponding to the 2–3 transition. This feature is called an anti-hole. The 1–2 energy can be simply determined from the energy separation between the hole and the anti-hole. However, we did not take yet into account that the 1–2 splitting is much smaller than the inhomogeneous linewidth. This means than the variation of the 1–3 and 2–3 transition energies are much larger than that of the 1–2 transition. For this reason, the laser is also exciting a second class of ions, for which the $2'$–$3'$ transition is at the same energy than the 1–3 for the first class of ions (Fig. 12D). After optical pumping, the populations for the two classes of ions are shown in Fig. 12E as well as the corresponding spectrum. A central hole is observed as well as two anti-holes. Populations initially in the 1 and $2'$ levels are now shelved in the 2 and $1'$ levels.

This pattern generalizes to cases where the ground and excited states have more complex hyperfine structures (Macfarlane and Shelby, 1987a). For example, Pr^{3+} has a single naturally abundant isotope, $^{141}Pr^{3+}$, with $I = 5/2$. Following the same reasoning as in Fig. 12D, nine classes of ions will be resonant at a given laser frequency. After population redistribution in the ground-state hyperfine levels, the spectrum will show three holes on each side of the central one. These holes correspond to transitions from empty ground-state levels to the excited states. There are 27 possible transitions (9 classes $\times$ 3 hyperfine levels) from which 9 correspond to the central hole and 6 correspond to the side holes with 3 classes contributing to each side hole. The anti-hole pattern is much more complex and consists in 42 lines, resulting from transitions from two ground-state levels with increased population to the three excited states for each class of ions (Fig. 13). Hole burning patterns become very complicated when the number of levels increases, because of a high nuclear spin or an applied magnetic field. When the hole burning pattern resolution is high enough and the hole and anti-hole absorption are not distorted by laser frequency and power instabilities, relative intensities of transitions between ground and excited hyperfine states can be determined (Klieber et al., 2003; Nilsson et al., 2004).

An extension of hole burning is spectral tailoring, which also relies on optical pumping and is used in many QIP protocols (Sections 5 and 6) to isolate classes of ions and/or create absorption patterns (Lauritzen et al., 2012; Nilsson et al., 2004; Pryde et al., 2000; Rippe et al., 2005). An example of this technique is shown in Fig. 14 for Pr^{3+}:$La_2(WO_4)_3$ (Guillot-Noël et al., 2009).

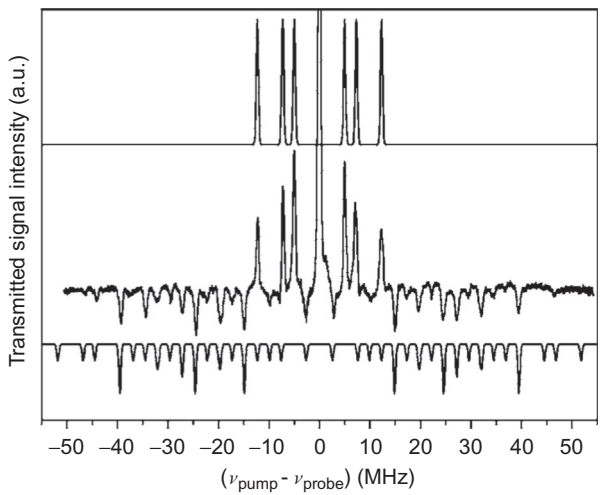

FIGURE 13 Holeburning spectrum in Pr^{3+}:$La_2(WO_4)_3$ at 4 K ($^3H_4(0) \rightarrow {}^1D_2(0)$ transition) (middle row). The upper (lower) row shows the calculated hole (anti-hole) pattern (Guillot-Noël et al., 2007).

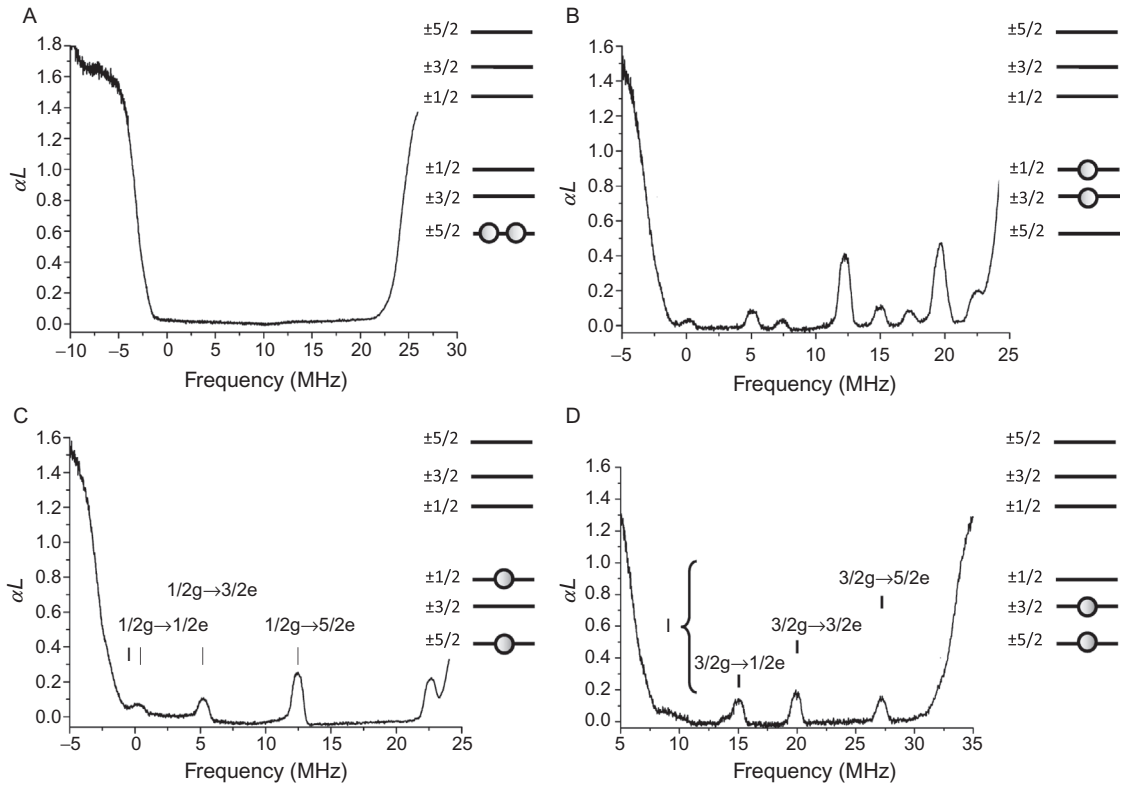

FIGURE 14 Spectral tailoring of the $^3H_4(0) \rightarrow {}^1D_2(0)$ transition in Pr^{3+}:$La_2(WO_4)_3$ at 2 K (Guillot-Noël et al., 2009). Populations are redistributed among ground-state hyperfine levels. (A) Absorption spectrum showing a nonabsorbing spectral pit of 22.5 MHz. α is the absorption coefficient and L the sample thickness. Ground-state populations for ions absorbing at 0 MHz on the $\pm$ 1/2g $\rightarrow \pm$1/2e transition (class I) are shown on the right. (B) Several lines appear in the pit after back-burning. (C) After class-cleaning, only transitions from the ground-state $\pm$ 1/2g level to the excited $\pm$ 1/2e, $\pm$ 3/2e, $\pm$ 5/2e levels are left for ions in class I. (D) A similar procedure can be used to isolate transitions from other hyperfine levels, in this case from the $\pm$ 3/2g level.

First, a large region without absorption is created in the inhomogeneous line by optical pumping and population redistribution among ground-state hyperfine levels. This spectral pit is limited to the difference $\Delta\Gamma$ between the total ground- and excited-state hyperfine splittings. If this limit is exceeded, one repumps ions that have transitions within the pit. $\Delta\Gamma$ sets the upper limit for spectral tailoring and may therefore limit the spectral bandwidth over which QIP can be performed. For Pr^{3+}:$La_2(WO_4)_3$, the pit width is limited to 27.2 MHz, close to the experimental one shown in Fig. 14A. The goal of the tailoring is to isolate transitions for ions in class I, which by definition have their $m_I = \pm 1/2g \rightarrow m_I = \pm 1/2e$ transition at the reference zero frequency, where g and e label ground and excited states (Figs. 14A and 15). After pit burning, all class I ions are in the $\pm 5/2g$ level; otherwise they would absorb into the spectral pit. To achieve line isolation, a spectrally narrow pulse is shone on the $\pm 5/2g \rightarrow \pm 5/2e$ transition to bring some class I ions back into the $\pm 1/2g$ and $\pm 3/2g$ levels (back-burning step). Ions from other classes will also be excited by this pulse, but because of the large pit burned at the beginning, there are only three of such classes. Only a limited number of unwanted lines are therefore appearing in the pit (Fig. 14B). The final step, called class cleaning, consists in scanning again the laser across these unwanted lines to pump corresponding ions to levels where they cannot absorb within the pit. As a result, only transitions from the $\pm 1/2g$ level of class I ions are observed (Fig. 14C). Similar procedures can be applied to isolate lines from the $\pm 3/2g$ and $\pm 5/2g$ levels (Fig. 14D). Once lines are isolated, level ordering can be determined, which is difficult with hole burning. For example, Fig. 14D shows that the energy difference between levels $\pm 1/2e$ and $\pm 3/2e$ is smaller than the one between levels $\pm 3/2e$ and $\pm 5/2e$. This leads to the energy scheme shown in Fig. 15. Another important information deduced from these spectral tailoring experiments is the relative oscillator strengths of transition between ground- and excited-state hyperfine levels (Fig. 15). In particular, this is needed to define Λ systems with large Rabi frequencies. As Pr^{3+} ions are located in sites of low symmetry (C_1) in $La_2(WO_4)_3$, the quadrupolar Q tensors can have different principle axes between ground and excited states. The $\Delta m_I = 0$ selection rule on optical transitions is therefore relaxed (Section 4.1.3), which explains that the transitions

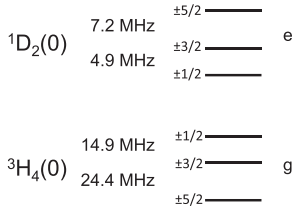

	1/2e	3/2e	5/2e
1/2g	0.09 ± 0.01	0.28 ± 0.01	0.63 ± 0.01
3/2g	0.33 ± 0.01	0.39 ± 0.01	0.28 ± 0.02
5/2g	0.55 ± 0.01	0.36 ± 0.01	0.09 ± 0.01

FIGURE 15 Hyperfine levels for the $^3H_4(0)$ and $^1D_2(0)$ CF levels in Pr^{3+}:$La_2(WO_4)_3$ and corresponding relative oscillator strengths (Guillot-Noël et al., 2009).

$\pm 3/2g \leftrightarrow \pm 3/2e$ and $\pm 5/2g \leftrightarrow \pm 3/2e$ have similar strengths. They could be therefore used as a Λ system. Low R site symmetries are generally favorable to Λ systems, which can also be obtained by applying an external magnetic field (Section 4.1.3). Spectral tailoring is a key point of most of the quantum memories and processors protocols (Sections 5 and 6), and its efficiency (e.g., the level of background absorption) is linked to relative oscillator strengths and lifetimes of the excited and shelving levels (Afzelius et al., 2010a; Lauritzen et al., 2008).

Raman Heterodyne Scattering

Spectral hole burning and tailoring determine hyperfine structures from optical spectra. It is also possible to directly record the transitions between hyperfine levels, but unlike EPR spectroscopy, NMR spectrometers are not sensitive enough to detect R dopant in crystals. However, this can be achieved by optical detection of magnetic resonance. Several techniques fall into this category (Macfarlane and Shelby, 1987a), but in the following we only describe Raman heterodyne scattering (RHS) (Mlynek et al., 1983; Wong et al., 1983), which can also be used to measure hyperfine coherence lifetimes.

The principle of RHS is based on a Λ system (Fig. 5) in which the ground-state transition is directly excited. First, a coherence, i.e., superposition states, is induced in the hyperfine transition of interest ($|0\rangle \leftrightarrow |1\rangle$) by a radiofrequency (rf) field, produced by a coil surrounding the crystal. At the same time, an optical probe is applied to the $|0\rangle \leftrightarrow |1'\rangle$ transition, creating a second coherence. Because coherences are present on transitions sharing a common level, an optical coherence is induced on the $|1\rangle \leftrightarrow |1'\rangle$ transition. The probe and induced optical fields have the same propagation properties and can therefore interfere. The transmitted light will therefore beat with a frequency equals to that of the $|0\rangle \leftrightarrow |1\rangle$ transition. A detector with sufficient bandwidth can detect this beating, which has also a fixed phase relationship with that of the rf excitation. This allows sensitive demodulation techniques to be applied. Radiofrequency sources with narrow linewidths are easily found, leading to high-resolution spectra which are especially useful to separate lines when an external field is applied (see Section 4.1.4). Excited-state hyperfine structures can also be obtained for the excited state. In this case, optical excitation is used to create the necessary excited-state population (Longdell and Sellars, 2004; Lovrić et al., 2011).

In the next sections, we examine two examples where energy-level structures have been determined and modeled for applications to QIP.

4.1.3 Efficient Λ System in Tm^{3+}:$Y_3Al_5O_{12}$

Yttrium aluminum garnet, $Y_3Al_5O_{12}$, is a cubic crystal with six groups of equivalent Y^{3+} sites of D_2 symmetry (i.e., three perpendicular C_2 axes) related by the symmetry operations of the crystal point group. Tm^{3+} has a $4f^{12}$

electronic configuration and a single naturally abundant isotope, ^{169}Tm, with $I = 1/2$. In D_2 symmetry, all CF levels are nondegenerate and the corresponding spin Hamiltonian has the general form given by Eq. (14). Here, all tensors are diagonal with respect to the CF axes x,y,z, which are directed along the three perpendicular C_2 axes. Moreover, as $I = 1/2$, there is no quadrupolar interaction and the spin Hamiltonian reduces to:

$$\begin{aligned}\mathcal{H}_S &= \boldsymbol{B}\cdot M\cdot \boldsymbol{I} \\ &= g_x B_x I_x + g_y B_y I_y + g_z B_z I_z,\end{aligned} \tag{16}$$

if the $\boldsymbol{B}\cdot Z\cdot \boldsymbol{B}$ term is neglected since it only shifts the whole hyperfine structure. The gyromagnetic factors g_i are the principal values of M and include the isotropic nuclear Zeeman interaction as well as a second-order hyperfine one: $g_i = -2A_J g_J \mu_B \Lambda - \gamma_n$ and can therefore depend on the CF level. The transition investigated occurs between the lowest CF levels of the ground $^3H_6$ and excited $^3H_4$ multiplets. Starting from the electronic wavefunctions determined from fitting the energy of CF levels, it was possible to calculate the corresponding Λ tensors and hence the spin Hamiltonian g parameters (Guillot-Noël et al., 2005). They are reported in Table 1.

A strong anisotropy is observed for both CF levels, with a g_y factor much larger than the two others. Moreover, g_y is also about seven times larger in the excited state than in the ground state, whereas the other parameters are closer. This suggests that it should be possible to obtain different spin wavefunctions in the ground and excited states by applying a suitable magnetic field. In turn, this would allow building an efficient Λ system, because transition strengths between ground and excited hyperfine levels are given by matrix elements of the form $\left|\psi_e\psi_n|\boldsymbol{D}|\psi'_e\psi'_n\right|^2$, where $\boldsymbol{D}$ is the electric dipole operator. The wavefunctions can be separated into electronic ψ_e and nuclear ψ_n parts because the spin interactions are much smaller than the electronic ones. As the electric dipole operator does not act on nuclear spins, the transition strengths between hyperfine levels for a given set of CF levels depend only

TABLE 1 Calculated and Experimental Gyromagnetic Factors for the $^3H_6(0)$ and $^3H_4(0)$ Levels in Tm^{3+}:$Y_3Al_5O_{12}$ (de Seze et al., 2006; Guillot-Noël et al., 2005).

Crystal Field Level		g_x (MHz/T)	g_y (MHz/T)	g_z (MHz/T)
$^3H_6(0)$	cal.	19	560	11
	exp.	< 52	403	< 40
$^3H_4(0)$	cal.	22	75	6
	exp.	20	82	14

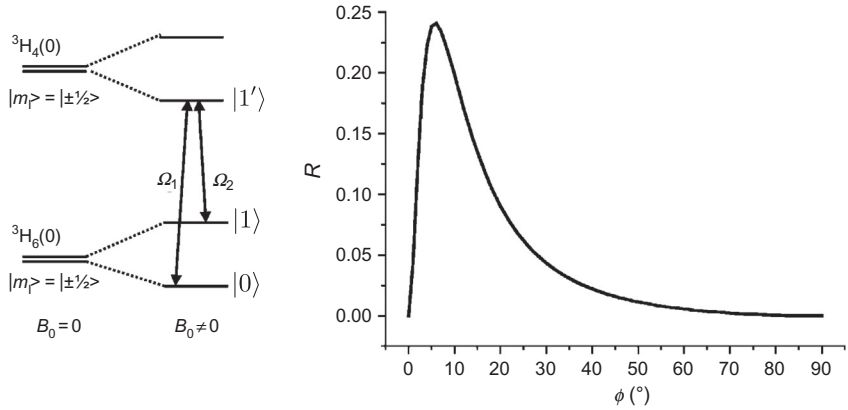

FIGURE 16 Investigated Λ system and calculated ratio R between $|1\rangle \leftrightarrow |1'\rangle$ and $|0\rangle \leftrightarrow |1'\rangle$ transition strengths for a magnetic field in the x,y plane (see text) with an angle ϕ with respect to the x axis in Tm^{3+}:$Y_3Al_5O_{12}$ (Guillot-Noël et al., 2005).

on the overlap of the nuclear wavefunctions $\left|\psi_n|\psi'_n\right|^2$, which can be deduced from Eq. (16) and Table 1 for an arbitrary magnetic field. Figure 16 shows the dependence of the ratio R between $|1\rangle \leftrightarrow |1'\rangle$ and $|0\rangle \leftrightarrow |1'\rangle$ transition strengths. When $\boldsymbol{B}$ is along the x (y) axis, the nuclear wavefunctions correspond to the $\pm m_I$ projections on the x (y) axis and the $|1\rangle \leftrightarrow |1'\rangle$ transition is forbidden. On the other hand, for $\boldsymbol{B}$ close to the x axis, the difference in g_y values has the largest effect. Accordingly, R takes its maximum value for a magnetic field forming an angle $\phi = 6^\circ$ with the x axis.

Experimentally, these predictions were confirmed to a reasonable extent by hole burning and photon-echo experiments as shown in Table 1 (de Seze et al., 2006; Louchet et al., 2007). It should be noted that these experiments are complicated by the six sites, with different x,y,z orientations, which Tm^{3+} ions occupy. In general, these sites become nonequivalent under a magnetic field, resulting in complex hole burning patterns. Additional site selection by polarized light can however be used to address a limited number of sites. Measured g_y values are 403 and 82 MHz/T for the ground and excited states, respectively, and the strong anisotropies of the calculated gyromagnetic factors were confirmed. The maximum ratio R is however only 0.13, compared to the predicted one of 0.25. Although, this value is far from the ideal $R = 1$ case, it still allows excitation of the two transitions of the Λ system, which has been used in determining parameters important for QIP applications, like hyperfine coherence lifetimes (Louchet et al., 2008) and efficiency of population transfer between hyperfine levels (Alexander et al., 2008).

4.1.4 Spin Hamiltonian in Pr^{3+}:$La_2(WO_4)_3$

A specific external magnetic field can also decouple a hyperfine transition from small magnetic field fluctuations and increase coherence lifetimes by

several orders of magnitude (Section 4.3.4). Direct experimental determination of this field can however be very difficult as its amplitude and direction have to be extremely accurate. A more systematic approach consists in first determining the spin Hamiltonian tensors and then calculate suitable magnetic fields. This has been carried out in several Pr^{3+}- and Eu^{3+}-doped crystals (Ahlefeldt et al., 2013d; Longdell et al., 2002, 2006; Lovrić et al., 2012). In the following, we briefly review experiments performed in Pr^{3+}:$La_2(WO_4)_3$ (Lovrić et al., 2011). This crystal has a monoclinic structure with 8 equivalent sites for Pr^{3+} with a C_1 symmetry. These sites are divided into two groups related by a C_2 symmetry along the crystallographic b axis. These groups become nonequivalent when a magnetic field is neither perpendicular or parallel to the b axis. Pr^{3+} ions have a single naturally abundant isotope, ^{141}Pr, with $I = 5/2$. Under a magnetic field, hyperfine structures split into six components, which are extremely difficult to determine by hole burning spectroscopy. Taking into account the magnetically nonequivalent sites, a hole burning spectrum could show up to 60 side holes and 1800 anti-holes! RHS was therefore used to determine ground ($^3H_4(0)$)- and excited ($^1D_2(0)$)-state hyperfine structures. Pr^{3+} g factors (principal values of tensor M, Eq. (12)) are typically in the range of 10–100 MHz/T, so that at low magnetic fields (<20 mT), $\pm m_I$ levels splitting are much smaller than the zero-field quadrupolar splitting (Fig. 17). The $\pm 1/2 \leftrightarrow \pm 3/2$ and $\pm 3/2 \leftrightarrow \pm 5/2$ transitions can therefore be recorded separately on a few MHz range around the zero field values. Figure 17 shows RHS spectra for the ground $^3H_4(0)$ and excited $^1D_2(0)$ states under magnetic fields of about 8 mT. As the fields for the ground and excited states are not applied in a direction for which sites are equivalent, up to eight lines can be resolved in each spectra, corresponding to two sets of the four possible $\pm m_I \leftrightarrow \pm m_I'$ transitions.

Ground- and excited-state spin Hamiltonians, including tensors M and Q, have each 11 unknown coefficients, as Pr^{3+} ions site symmetry is C_1 (Section 4.1.1). Note that E and D values of the quadrupolar interaction are approximately known from the zero-field hole burning spectrum (Fig. 13).

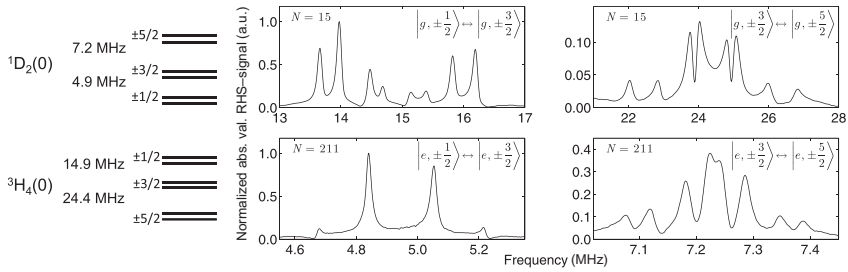

FIGURE 17 Raman heterodyne spectra for the hyperfine transitions of the ground $^3H_4(0)$ (upper row) and excited $^1D_2(0)$ (lower row) levels ($T = 5$ K) under two differently oriented magnetic fields of ≈8 mT in Pr^{3+}:$La_2(WO_4)_3$ (Lovrić et al., 2011).

The orientations of Q principal axes are however unknown. The tensors are determined in the reference axes of the magnetic field but two additional coefficients have also to be introduced to take into account the orientation of the crystal C_2 axis, which relates the nonequivalent sites. The 13 coefficients are fit to a series of spectra obtained with the magnetic field vector describing a spiral on a sphere (Longdell et al., 2002), with a constant magnitude of about 8 mT. This allows an efficient sampling of the M and Q tensors, which helps avoiding local minima in the fit. To further enhance the reliability of the parameters, a simulated annealing algorithm was used, as well as several conventions to avoid ambiguities in the parameters, linked to permutations of the tensors' principal axes. Very good agreements between experimental and calculated transition energies were found, leading to precise parameters. This was a fundamental requirement for accurate prediction of the magnetic fields used to extend coherence lifetimes (see Section 4.3). The principal axes of the Q and M tensors are found to be close to each other in both ground and excited states. However, as expected in a low symmetry site, they significantly differ between these levels. At zero field, the Q tensors' different orientations allow transitions with $\Delta m_I \neq 0$ to be observed (see Fig. 14C and D). Indeed, the oscillator strengths between hyperfine levels determined by spectral tailoring (Fig. 15) are in very good agreement with the nuclear wavefunctions overlap deduced from the fitted Q tensors. The ground-state M tensor is also found to be highly anisotropic, in opposition to the excited-state one. A CF calculation was performed assuming a higher site symmetry, C_{2v}, to reduce the number of CF parameters to be fitted to experimental levels. Although in C_{2v} all tensors have collinear principal axes, the calculated principal values for the M and Q tensors are quite close to the experimentally determined ones (Guillot-Noël et al., 2010; Lovrić et al., 2011). This gives some insight on the contributions to the Q and M tensors. In particular, in the excited state, the second-order hyperfine effect is small, in agreement with the experimental isotropy of the M tensor. The calculated principal values could also be used as a starting point for fitting the RHS spectra.

4.2 Transition Strengths and Inhomogeneous Linewidths

Oscillator strengths of f–f transitions, which are of weakly allowed electric dipole or magnetic dipole nature, are of the order of 10^{-8} to 10^{-6}. As transitions of interest occur between specific energy CF levels (Section 4.3), their strength can significantly vary from host to host. For example, the oscillator strength of the $^3H_4(0)$–$^1D_2(0)$ transition is 2.3×10^{-8} in Pr^{3+}:$La_2(WO_4)_3$ (Guillot-Noël et al., 2007) and 3×10^{-7} in Pr^{3+}:Y_2SiO_5 (site 1) (Equall et al., 1995), although these crystals have the same structure with identical site symmetry for Pr^{3+} ions. To reach a given Rabi frequency, strong transitions require pulses of lower intensity (Section 3.1). Typical Rabi frequencies that can be achieved are $\approx$1–10 MHz with laser intensities in the 100s of W/cm^2 range.

A large absorption is also necessary for efficient quantum memories (Section 5.2). This can be obtained with cavities or long samples, or by using crystals with large absorption coefficients α. For a given transition strength, α can be increased by increasing R concentration. However, this tends to also increase the transition inhomogeneous linewidth Γ_{inh}. The frequency shifts of the homogeneous lines resulting in Γ_{inh} are due to small changes in electric fields at the R site, because of defects, impurities, etc. (Macfarlane, 1990; Meltzer, 2005). Optical transition inhomogeneous linewidths therefore depend on the crystal quality in terms of strains and defects, as well as on the dopant itself. Differences in ionic radii between the dopant and the substituted cation induce strains, typically resulting in a linear dependence of Γ_{inh} as a function of the dopant concentration (Beaudoux et al., 2012; Könz et al., 2003). Lower inhomogeneous linewidths are favored by close ionic radii between dopant and substituted cation. For example, in Pr^{3+}:$La_2(WO_4)_3$, the $^3H_4(0)\rightarrow{}^1D_2(0)$ inhomogeneous linewidth varies with a slope of 10.8 GHz/at.%, about 12 times smaller than that found in Pr^{3+}:Y_2SiO_5 (Beaudoux et al., 2012). This can be explained by the close ionic radii of Pr^{3+} and La^{3+} (1.14 and 1.18 Å, respectively) and the smaller radius of Y^{3+}(1.02 Å). The increase of Γ_{inh} can prevent obtaining large peak absorptions by varying the dopant concentration. For example, in Eu^{3+}:Y_2SiO_5, 10,000- and 1000-ppm-doped crystals have similar peak absorption coefficients for the $^7F_0\rightarrow{}^5D_0$ transition (Fig. 18) (Könz et al., 2003). Low inhomogeneous broadening favors high peak absorption, but in some quantum memory protocols also limits the memory bandwidth (Section 5.2). This can be overcome by using crystals with disorder (due to random vacancies or codoping), which can exhibit linewidths of 100s of GHz (Böttger et al., 2008; Sun et al., 2012; Thiel et al., 2010). Optical inhomogeneous linewidths in high-quality ordered crystals are in the 0.5–20 GHz, although in some halide compounds it can be as low as 10s of MHz (Macfarlane, 2002; Sun, 2005; Thiel et al., 2011). This could be

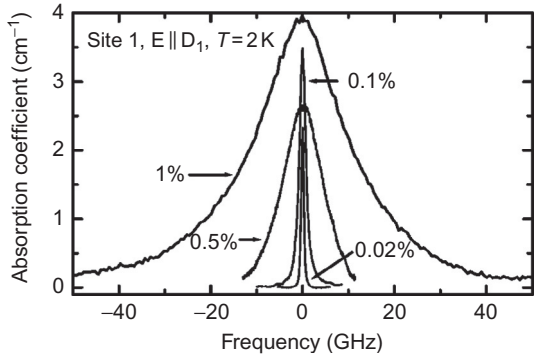

FIGURE 18 Inhomogeneous linewidths of the $^7F_0\rightarrow{}^5D_0$ transition as a function of Eu^{3+} concentration in Y_2SiO_5 at $T = 2$ K. *Reproduced with permission from Könz et al. (2003), © 2003 the American Physical Society (http://dx.doi.org/10.1103/PhysRevB.68.085109).*

explained by a lower defect density in these materials (Macfarlane, 2002). Low inhomogeneous broadening ($\approx$ 100 MHz) has also been observed in the stoichiometric crystal $EuCl_3{\cdot}6H_2O$ (Ahlefeldt et al., 2009). Here, the dopant-related broadening is avoided and this material exhibits at the same time a low Γ_{inh} and a high absorption coefficient.

Hyperfine transition inhomogeneous linewidths have not been studied to the same extent as optical ones. In several Pr^{3+} and Eu^{3+} crystals, hyperfine Γ_{inh} are found in the 10–100 kHz range (Erickson, 1985; Lovrić et al., 2011, 2012; Mitsunaga et al., 1984; Mlynek et al., 1983; Timoney et al., 2012, 2013). These values are several orders of magnitude smaller than optical inhomogeneous broadening, which is due to the fact that hyperfine transition energies are determined by operators which do not directly involve CF parameters. Inhomogeneous broadening is therefore due to variations in CF wavefunctions. Hyperfine transitions with low Γ_{inh} are important for coherence rephasing and control (Section 4.3.4), as they can be fully addressed by rf pulses of larger duration and therefore lower intensity.

4.3 Coherence Lifetimes

Coherence lifetimes T_2 are central to QIP, as they determine the lifetime of the superposition states of qubits. For R ions, long coherence lifetimes are required primarily for qubit transitions, i.e., hyperfine ones, but also for optical transitions, which are used for qubit state control and coherence transfer. The longest coherence lifetimes are found for single crystals, but it has been recently observed that R-doped ceramics (Ferrier et al., 2013) and nanocrystals (Perrot et al., 2013) can exhibit comparable T_2 values. On the other hand, amorphous hosts are generally not favorable to long T_2 (Macfarlane, 2002), as disorder induces strong dephasing (see below).

In this section, we first discuss sources of dephasing in R-doped crystals, then describe the experimental techniques used to determine T_2 as well as the typical dynamics observed, and finally show examples of hyperfine T_2 extension by applying external fields or train of rf pulses.

4.3.1 Population Relaxation

Coherence lifetimes are determined by population and phase relaxation (see Section 3.2). For an isolated ion, a first contribution to T_2 for optical transitions is the excited-state spontaneous emission. In R ions, radiative lifetimes vary approximately between 50 μs and 10 ms. Nonradiative processes can also affect populations of both ground and excited levels. At low temperatures (< 10 K), the dominant mechanism for transitions between CF levels is usually direct one-phonon absorption or emission (Macfarlane, 2002). When only phonon absorption can occur, its contribution to T_2 is usually negligible at temperatures lower than 4–5 K. This is why only $^{2S+1}L_J(0) - {}^{2S'+1}L'_{J'}(0)$, i.e., transitions between CF levels of lower energy in multiplets, are currently used

for QIP applications. Excited states should also be separated from levels immediately below by energies much larger than the phonon cut-off frequency of the host to avoid multiphonon processes (Miyakawa and Dexter, 1970).

Population relaxation can also occur by interactions between different centers, like energy transfers between R ions and impurities or between R ions themselves (Henderson and Imbush, 1989). This second type of energy transfer, so called cross-relaxation, can limit T_2 at high R concentration. For example, two Pr^{3+} ions can exchange energy according to the scheme $(^1D_2, {}^3H_4) \rightarrow (^1G_4, {}^3F_4)$, which strongly reduces $^1D_2$ population lifetime at high Pr^{3+} concentrations. In this case, T_2 can be also strongly reduced, as shown in Fig. 19 (Beaudoux et al., 2012). As the cross-relaxation involves phonon emission, its probability can be large even at low temperatures.

At liquid helium temperatures, hyperfine population lifetimes range from 70 ms (Xu et al., 2004) to 120 s for Pr^{3+} and can reach 23 days in Eu^{3+}:Y_2SiO_5 (Könz et al., 2003). These contributions are generally negligible compared to dephasing mechanisms both for optical and hyperfine transitions. Hyperfine population lifetimes are however important in determining spectral tailoring efficiency (Section 4.1.2).

4.3.2 Pure Dephasing Processes

Dephasing by two-phonon Raman elastic scattering can be important, when population relaxations are negligible (Macfarlane, 2002). An example is

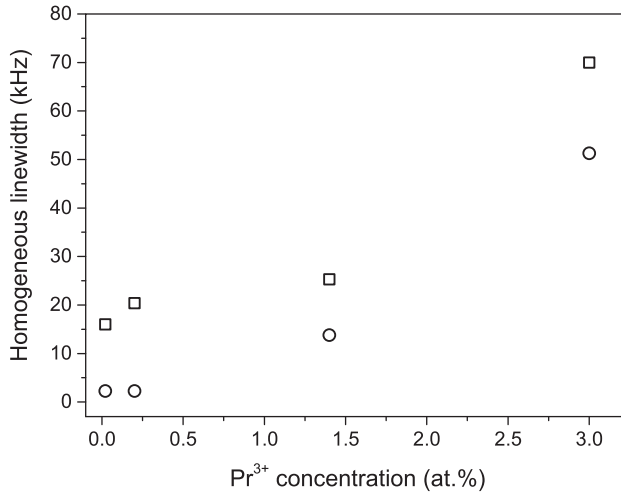

FIGURE 19 Homogeneous linewidth, $\Gamma_h = 1/(\pi T_2)$, of the $^3H_4(0) \leftrightarrow {}^1D_2(0)$ transition (squares) at 3.5 K and contribution $1/(2\pi T_1)$ from the excited-state population lifetime (circles) as a function of Pr^{3+} concentration in $La_2(WO_4)_3$ (Beaudoux et al., 2012).

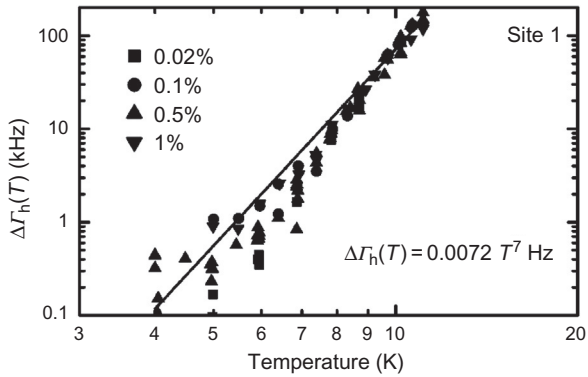

FIGURE 20 Homogeneous linewidth broadening of the $^7F_0 \leftrightarrow {}^5D_0$ transition as a function of temperature T in Eu^{3+}:Y_2SiO_5 for ions in site 1 and at different concentrations. The solid line corresponds to a T^7 two-phonon Raman process. *Reproduced with permission from Könz et al. (2003), © 2003 the American Physical Society (http://dx.doi.org/10.1103/PhysRevB.68.085109).*

shown in Fig. 20, where the broadening of the $^7F_0 \leftrightarrow {}^5D_0$ transition between CF singlets is plotted as a function of temperature T in Eu^{3+}:Y_2SiO_5 (Könz et al., 2003). A T^7 dependence is observed, corresponding to a low-temperature two-phonon Raman process. It becomes the largest dephasing mechanism for temperatures above ≈6–7 K, as the temperature-independent contribution to homogeneous linewidth is about 800 Hz.

At temperatures for which phonon dephasing can be neglected, decoherence occurs through fluctuations of transition frequencies (Macfarlane, 2002). This results in phase fluctuations and therefore in coherence loss. Transition frequencies can be affected by magnetic fields produced by the host spins. For singlets of non-Kramers ions, two terms depend on magnetic fields in the spin Hamiltonian given by Eq. (9). Optical transitions are affected by both $\boldsymbol{B} \cdot Z \cdot \boldsymbol{B}$ and $\boldsymbol{B} \cdot M \cdot \boldsymbol{I}$ through differences in tensors between excited and ground states. On the other hand, hyperfine transitions are only sensitive to the $\boldsymbol{B} \cdot M \cdot \boldsymbol{I}$ term. Within the host, magnetic fields are due to electronic or nuclear spins, which can randomly change states through phonon-induced relaxations or population-conserving mechanisms, in which two spins make simultaneous and opposite transitions (flip-flop). Hosts with low magnetic moment densities therefore favor low dephasing. In Y_2SiO_5, where Y has a low nuclear magnetic moment and other nonzero nuclear spins a low concentration, optical T_2 approaches T_1 for Pr^{3+} ($T_1 = 164\ \mu s$, $T_2 = 152\ \mu s$) and Eu^{3+} ($T_1 = 1.9$ ms, $T_2 = 1.5$ ms) as reported in Equall et al. (1995) and Könz et al. (2003). Low gyromagnetic factors (principal values of M) are also reducing dephasing. As a result, ground-state hyperfine coherence lifetimes are larger for Eu^{3+} than for Pr^{3+}-doped hosts. In Y_2SiO_5, the largest gyromagnetic factor are 113 and 11 MHz/T for Pr^{3+} and Eu^{3+}, respectively (Longdell et al., 2002, 2006), in qualitative agreement with the respective hyperfine T_2 values of 0.5

and 15–19 ms (Alexander et al., 2007; Arcangeli et al., 2014; Fraval et al., 2004). When considering host spins, doping R ions must also be taken into account. The magnetic moments of non-Kramers ions are given by $M \cdot \boldsymbol{I}$ and are therefore of the order of magnitude of nuclear ones. At low doping concentrations, R–R magnetic interactions are therefore generally negligible. As an example, Fig. 21 shows that hyperfine echoes decay as a function of pulse delay independently of Pr^{3+} concentration in $La_2(WO_4)_3$ and dephasing is attributed to flipping La^{3+} nuclear spins (Beaudoux et al., 2012).

In Kramers ions, the main term in the spin Hamiltonian Eq. (14) is $\mu_B \boldsymbol{B} \cdot g \cdot \boldsymbol{S}$. It scales approximately as μ_B, whereas field-dependent terms for non-Kramers ion singlets are of the order of the nuclear magneton and are therefore about 1000 times smaller. Optical and electronic spin transitions of Kramers ions are therefore much more sensitive to magnetic field fluctuations. Moreover, electron spins of doping R ions themselves, which have a moment $\mu_B g \cdot \boldsymbol{S}$, can be a major source of dephasing, even at concentrations as low as 10s of ppm (Böttger et al., 2006; Macfarlane, 2002). Large magnetic fields can be used to reduce this effect (Section 4.3.4).

Flipping spins may lead to complex behaviors for the echo decays of R ions (Böttger et al., 2006; Ganem et al., 1991; Sun et al., 2012; Thiel et al., 2010). When their flipping rate is slower than the echo decay timescale, they produce progressive frequency shifts, an effect known as spectral diffusion (Hu and Hartmann, 1974; Hu and Walker, 1978). It is typically revealed by nonexponential echo decays, where at short times, only few spins flip and the decay is slow and at longer times, the cumulative effect of spin flips

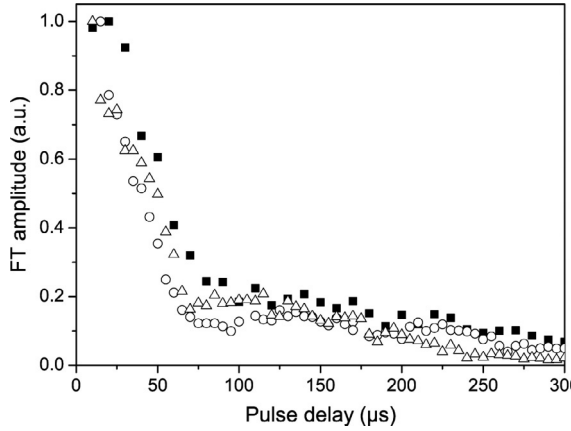

FIGURE 21 Hyperfine echo amplitude as a function of the delay between exciting and rephasing pulses for different Pr^{3+} concentrations in $La_2(WO_4)_3$ (Beaudoux et al., 2012). Squares: 0.02 at.%, circles: 1.4 at.%, and triangles: 3 at.%. The decays at long delays correspond to the hyperfine coherence loss, which is independent of Pr^{3+} concentration ($T_2 = 250\ \mu s$). The rapidly decaying initial part is due to FID.

shortens the decay. The echo decay intensity I can be described by an effective linewidth Γ_{eff} which varies as a function of the pulse delay τ:

$$I(\tau) = I_0 \exp[-4\tau\pi\Gamma_{\text{eff}}(\tau)] \tag{17}$$

or by more phenomenological expressions of the form (Mims, 1968):

$$I(\tau) = I_0 \exp(-4\tau/T_{\text{M}})^x \tag{18}$$

where T_{M} is the phase memory time and x is often found close to 2. Spectral diffusion therefore results in a progressive broadening of the homogeneous linewidth Γ_{eff}. If $x = 1$, the phase memory time is equal to the coherence lifetime, $T_{\text{M}} = T_2$. An example is given in Fig. 22, where the photon-echo decay of Tm^{3+} in LaF_3 is recorded with and without an external magnetic field (Macfarlane, 1993). In this crystal, the flipping nuclear spins of fluorine ions are the main source of dephasing. When an external field is applied, ^{19}F flip-flop rates are slowed down. This results in spectral diffusion and a decay whose rate increases with increasing time. Additional effects can be observed

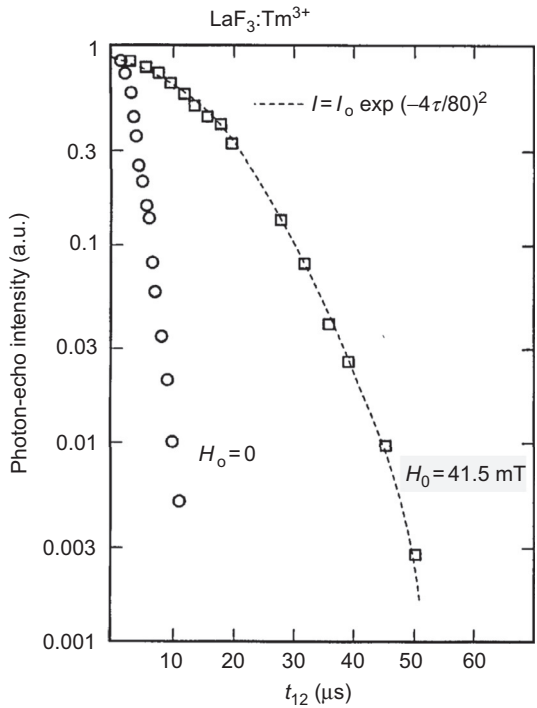

FIGURE 22 Two-pulse photon-echo decay of the $^3H_6(0) \leftrightarrow {}^3H_4(0)$ transition in Tm^{3+}:LaF_3 ($T = 1.5$ K). Applying an external magnetic field ($H_0 = 41.5$ mT) slows down ^{19}F nuclear spin flip-flop, resulting in spectral diffusion and a non exponential decay. *Reproduced with permission from Macfarlane (1993), ©1993 Optical Society of America.*

for R ion with strong magnetic moments like Kramers ions. The magnetic field they produce can be large enough to shift neighboring spins out of resonance compared to more distant spins, reducing flip-flop processes. The R ion is thus surrounded by spins with low flipping rates, the so-called frozen core (DeVoe et al., 1981; Ganem et al., 1991; Macfarlane and Shelby, 1987a). The echo decays are then affected by close spins with large effect on the R transitions, but with a low flipping rate, and by more distant ones, which flip faster but produce smaller fluctuations. Line shifts also occur on timescales longer than T_2 (Böttger et al., 2006). This may prevent exciting the same ions over long times. For example, QIP applications often require that a group of ions is selected by spectral tailoring of the optical absorption line. An optical coherence created in these ions can be transferred to an hyperfine one and can processed for a time as long as the hyperfine coherence lifetime, T_2^{hf}, which can be several orders of magnitude larger than the optical one. Transferring back the hyperfine coherence to the optical one is possible only if the spectral diffusion of the optical transitions is small enough on a timescale of T_2^{hf}. Spectral broadening on long timescales can be probed by three-pulse echoes or time-resolved spectral holeburning (see Section 4.3.3).

Disorder can also affect coherence lifetimes. In single crystals, this can occur through doping, defects, or by random distribution of host cations. Disorder produces a contribution to dephasing varying approximately linearly with temperature (Flinn et al., 1994; Macfarlane et al., 2000). By analogy with amorphous systems (Macfarlane and Shelby, 1987b), it has been suggested that it is due to atoms tunneling between two positions, with broad distributions of tunneling rate and energies, and referred to as two-level systems (TLS). In some cases, crystal growth methods and parameters have large effects on these TLS, as shown in Fig. 23 (Flinn et al., 1994). Only the crystal obtained by flame fusion shows the T^7 temperature dependence expected for a two-phonon Raman process in a Eu^{3+}-doped single crystal. In the other samples, oxygen vacancies have been suggested as the source of disorder. Although disorder generally leads to an increased dephasing, it has also been shown that, at low level, it could actually lengthen coherence lifetimes. In Eu^{3+}, Er^{3+}:Y_2SiO_5, Er^{3+} Zeeman transitions are broadened by the codoping and the resonance condition for flip-flop processes disappears. This slows down spin fluctuations and in turn increases Er^{3+} optical T_2 (Thiel et al., 2012).

4.3.3 Experimental Techniques

Photon and Spin Echoes

Coherence lifetime measurements are usually based on echo techniques (Section 3.2), which are less demanding on excitation source stability and can probe coherence decays over short times compared to spectral hole burning. Optical transitions can be directly measured, as the echo signal is often strong enough for available detectors. Signal-to-noise ratio can be increased

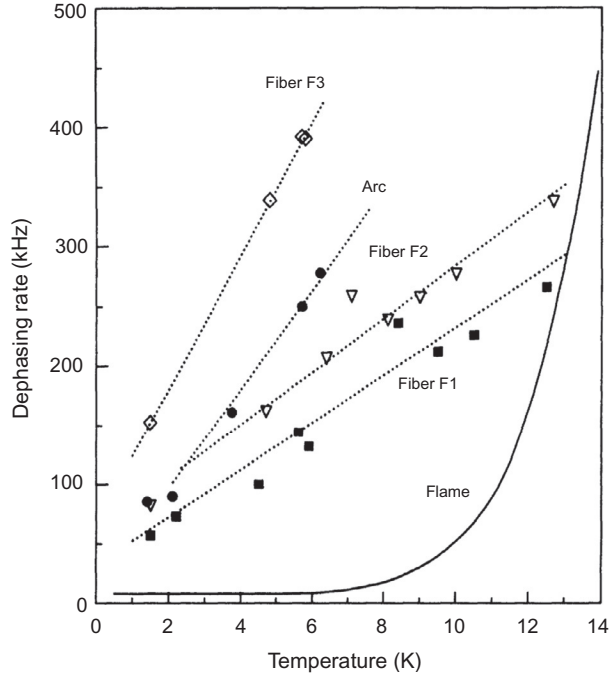

FIGURE 23 Dephasing rate (equivalent to homogeneous linewidth) of the $^7F_0 \leftrightarrow {}^5D_0$ transition as a function of temperature in Eu^{3+}:Y_2O_3 for samples grown by different techniques: arc furnace, flame fusion, and laser-heated pedestal growth for fibers. *Reproduced with permission from Flinn et al. (1994), © 1994 the American Physical Society (http:/dx.doi.org/10.1103/PhysRevB.49.5821).*

by interfering the echo with a local oscillator for heterodyne detection. Optical echoes can even be recorded in strongly scattering samples (Beaudoux et al., 2011; Perrot et al., 2013). Hyperfine transitions are too weak to be detected directly and have to be optically detected, for example using the RHS technique described in Section 4.1.2 (Mlynek et al., 1983). First, an optical pumping sequence empties one of the hyperfine levels, as the coherence which can be created is proportional to their population difference. The transition is then excited and rephased by rf pulses. Finally, at the time when the hyperfine echo forms, an optical probe is shone on the sample, and a new optical field is created. These two fields beat at the frequency of the hyperfine transition, with an amplitude proportional to that of the hyperfine echo. The decay of the beat note amplitude as a function of the rf pulse delay allows retrieving the coherence lifetime of the hyperfine transition. To generate rf pulses with large enough areas and bandwidth, high powers are generally required as well as a tuned circuit acting as a rf resonator. An alternative is to use all-optical excitation, a technique known as Raman echo (Alexander et al., 2007; Guillot-Noël et al., 2009; Hu et al., 1976; Louchet et al., 2008). Here, the hyperfine transition excitation and rephasing are achieved by optical

two-color pulses, with a frequency difference corresponding to that of the hyperfine transition. The hyperfine echo is detected by an optical probe, in the same way as in RHS experiments.

Three-Pulse Echoes

Probing spectral diffusion on timescales longer than T_2 is possible using three-pulse photon echoes (Fig. 24). The sequence starts with two $\pi/2$ pulses, separated by a delay τ. The first pulse, assumed to have an X phase, rotates the atoms' Bloch vectors in the equatorial plane of the Bloch sphere. Atoms then dephase depending on their detuning with respect to the excitation frequency. After a delay τ, the second X $\pi/2$ pulse creates populations depending on the atom dephasing and therefore frequency. If the absolute dephasing is lower (larger) than $\pi/2$ compared to the x axis of the Bloch sphere, an excited- (ground) state population appears. This creates a spectral population grating, with a period of $\approx 1/\tau$. After a delay T_w, a third X $\pi/2$ pulse is applied, resuming the phase evolution interrupted by the second pulse, which results in an echo at a time $2\tau + T_w$. Its intensity is given by:

$$I(2\tau + T_w) = I_0 \exp\left(\frac{-2T_w}{T_1}\right)\exp[-4\tau\pi\Gamma_{eff}(\tau, T_w)], \tag{19}$$

where the effective homogeneous linewidth Γ_{eff} depends on both τ and T_w. Spectral diffusion processes will result in an increase of Γ_{eff}, which reduces

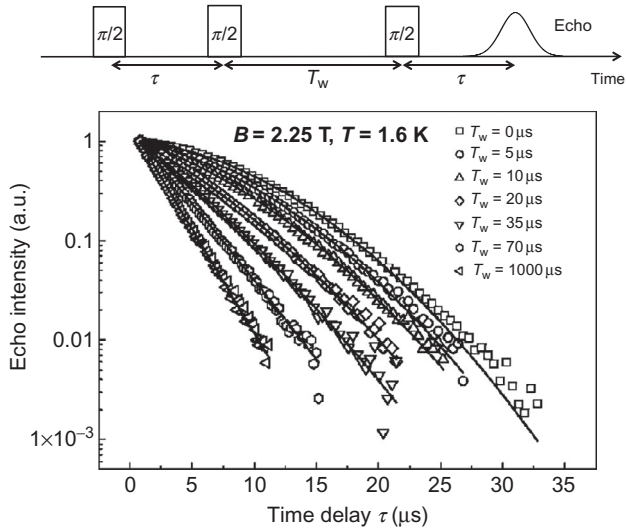

FIGURE 24 Three-pulse photon-echo intensity decays of the $^4I_{15/2}(0) \leftrightarrow {}^4I_{13/2}(0)$ transition in 0.02% Er^{3+}:Y_2SiO_5 as a function of τ and T_w delays. An external magnetic field of 2.25 T is applied to the sample. *Reproduced with permission from Böttger et al. (2006), © 2006 the American Physical Society (http://dx.doi.org/10.1103/PhysRevB.73.075101).*

the echo intensity by washing out the spectral grating. This effect can be probed by varying T_w on a T_1 timescale instead of T_2 or T_M for a two-pulse photon-echo experiment. An example of echo intensity decays as a function of τ and T_w is shown in Fig. 24 for Er^{3+}:Y_2SiO_5 (Böttger et al., 2006). As T_w increases, the decays become faster, clearly showing spectral diffusion effects, which are moreover revealed by their nonexponential dependence on τ. Solid lines are fitted to the decays with Eq. (19), using an expression for Γ_{eff} involving transition fluctuation rates and amplitude. In this material, fluctuations are due to Er^{3+} ions flipping between ground-state electronic Zeeman levels.

Spectral Hole Burning

Spectral hole burning can result in holes with widths twice the homogeneous linewidth, assuming that the laser linewidth is much narrower. This method is however often difficult to use because of the strong requirements on laser frequency and power stability and effects like broadening of the hole when the laser intensity is too high. Moreover, the holes are probed on long timescales because of the duration of the pumping and scanning sequences. Clearly, echo techniques provide more detailed and reliable information. SHB is however very useful to probe homogeneous linewidths on timescales longer than T_1 if population storage occurs on longer-lived levels. In this case, a variable delay is introduced between the pumping and the scanning steps. In Eu^{3+}:Y_2O_3, where population is stored in hyperfine levels, Γ_{eff} has been measured for delays up to 10 s, four orders of magnitude larger than the optical excited-state $^5D_0$ lifetime of about 1 ms (Sellars et al., 1994).

4.3.4 *Increasing Coherence Lifetimes*

High Magnetic Field

Coherence lifetime extension can be achieved either by reducing the environment fluctuations or by reducing the sensitivity of the R ion to them. An example of the first approach is given by the effect of a magnetic field on the $^4I_{15/2}(0) \leftrightarrow {}^4I_{13/2}(0)$ transition in Er^{3+}:Y_2SiO_5 (Böttger et al., 2006). The maximal homogeneous broadening, Γ_{SD}, at temperature T and under a magnetic field $\boldsymbol{B}$ is given by:

$$\Gamma_{SD} = \frac{\pi}{9\sqrt{3}} \frac{\mu_0 |g_{es} - g_{gs}| n_{env}}{h} \operatorname{sech}^2\left(\frac{g_{env}\mu_B B}{2kT}\right), \tag{20}$$

where g_{es} and g_{gs} are the g factors of the $^4I_{13/2}(0)$ excited and $^4I_{15/2}(0)$ ground states, k the Boltzmann constant, and μ_0 the vacuum permeability. Dephasing is due to spins with an n_{env} concentration and a g factor g_{env}. The sech function in Γ_{SD} expression takes into account the spin populations at thermal equilibrium. Γ_{SD} is the broadening which is observed when all spins in Er^{3+}

environment have flipped and is determined by homogeneous linewidth measurements on long timescales using three-pulse photon echoes. At high magnetic field, or equivalently low temperature, spins are mainly in the ground state. Transitions to the upper state are less probable, as is the corresponding induced frequency shift on the optical transition, which is simply proportional to $|g_{es} - g_{gs}|$. In the limit $B \to \infty$, $T \to 0$, Eq. (20) shows that $\Gamma_{SD} \to 0$. Figure 25 shows this effect in Y_2SiO_5 doped at different Er^{3+} concentrations. Y_2SiO_5 is a monoclinic crystal with two C_1 sites for Y^{3+} or Er^{3+} ions. ^{89}Y is 100% abundant, with a $I = 1/2$ nuclear spin and a low magnetic moment $\mu = -0.14\mu_B$. As silicon and oxygen main isotopes have zero nuclear spins, the main contribution to Er^{3+} dephasing is the flipping electronic spins of Er^{3+} ions themselves, even at concentrations as low as 15 ppm. The optical transition probed in the experiments of Fig. 25, $^4I_{15/2}(0) \leftrightarrow {}^4I_{13/2}(0)$, corresponds to Er^{3+} in site 1. Dephasing could be due to Er^{3+} ions in both sites but the ground-state g factor of ions in site 2 is much larger than those in site 1, for the magnetic field direction chosen. Er^{3+} ions in site 1 themselves have therefore the larger contribution to Γ_{SD}, and set n_{env} and g_{env} values. As expected from Eq. (20), the homogeneous broadening decreases with decreasing Er^{3+} concentration, but a much more dramatic effect is obtained by increasing the magnetic field (Fig. 25). As a result, homogeneous linewidths as low as 73 Hz have been obtained at doping level of 15 ppm and under a 7 T magnetic field, approaching the natural linewidth of 14 Hz (Böttger et al., 2009). The remaining dephasing is attributed to host nuclear spins. Effects of large magnetic fields on optical coherence lifetime have been investigated in a number of crystals (Sun, 2005; Thiel et al., 2011).

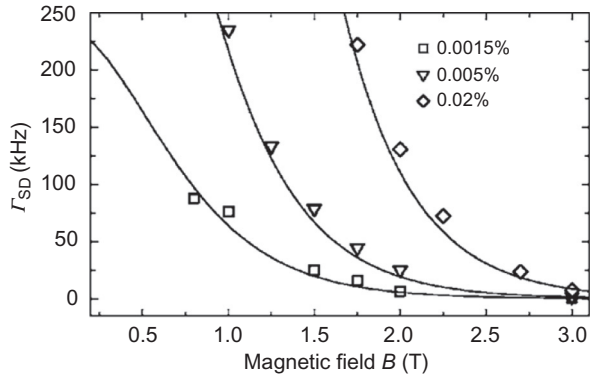

FIGURE 25 Maximum homogeneous broadening Γ_{SD} of the $^4I_{15/2}(0) \leftrightarrow {}^4I_{13/2}(0)$ transition in Er^{3+}: Y_2SiO_5 as a function of the external magnetic field and at different concentrations. $T = 1.6$ K. *Reproduced with permission from Böttger et al. (2006), © 2006 the American Physical Society (http://dx.doi.org/10.1103/PhysRevB.73.075101).*

Zero First-Order Zeeman Shift

Increasing coherence lifetimes by applying a large magnetic field is very efficient when dephasing is due to electronic spins, for which the Zeeman excited state can be strongly depopulated. This is much more difficult to obtain for nuclear spins, and in this case, coherence extension is better performed by decoupling R ions from magnetic field fluctuations. We first discuss the use of transitions showing a zero first-order Zeeman shift (ZEFOZ), also known more generally as "clock" transitions, from their use in atomic clocks (Fraval et al., 2004). A ZEFOZ transition is weakly sensitive to small magnetic field fluctuations because its frequency as a function of the magnetic field $\boldsymbol{B}$ has a zero first-order derivative for all field orientations. To reach this situation, levels involved in the transition should have a nonlinear dependence on $\boldsymbol{B}$ and this is generally found when they are determined by competing interactions. For example, hyperfine transitions in non-Kramers ions with $I > 1/2$ involve quadrupolar and Zeeman interactions (M and Q tensors in Eq. (12)), which can be of the same order of magnitude for high enough magnetic fields. The nuclear wavefunctions' mixing introduced by the Zeeman interaction leads to level anti-crossings. However, since the first-order derivative must vanish for all field directions (or equivalently for three perpendicular ones), a simple anti-crossing situation is not sufficient. An accurate knowledge of the spin Hamiltonian is needed, together with numerical search for ZEFOZ transitions, which should then be chosen to minimize second-order derivatives. This has been performed in several Eu^{3+}, Pr^{3+}, and Er^{3+}-doped compounds (Ahlefeldt et al., 2013d; Fraval et al., 2004; Heinze et al., 2013; Longdell et al., 2006; McAuslan et al., 2012). In the following, we present results obtained in Pr^{3+}:$La_2(WO_4)_3$ (Lovrić et al., 2011). Starting from an accurately determined ground-state spin Hamiltonian (see Section 4.1.4), ZEFOZ transitions can be calculated. An example is given in Fig. 26. The principal values of the M tensor vary approximately between 50 and 150 MHz/T and for a field of 350 mT will lead to ground-state splittings of about 17–50 MHz. On the other hand, the zero-field hyperfine splittings, due to the quadrupolar interaction, are 14.9 and 24.4 MHz and are therefore of the same order of magnitude. This explains the highly nonlinear behavior observed in the transition energies as a function of the magnetic field (Fig. 26). In the energy range displayed, only one ZEFOZ transition is found, lying at 12.6 MHz for a very specific magnetic field orientation and magnitude, which clearly can only be found by calculations based on the spin Hamiltonian. As this transition is weakly sensitive to magnetic field fluctuations, one expects that the related dephasing will be reduced and therefore the coherence lifetime extended. This was investigated using the RHS two-pulse echo technique (see Section 4.3.3). Hyperfine echo decays as a function of the delay between the excitation pulse and the echo are presented in Fig. 27 for three different magnetic fields. When $\boldsymbol{B}$ is set exactly at the ZEFOZ point, the 12.6 MHz transition has a hyperfine T_2^{hf} of 158 ms, nearly three orders of

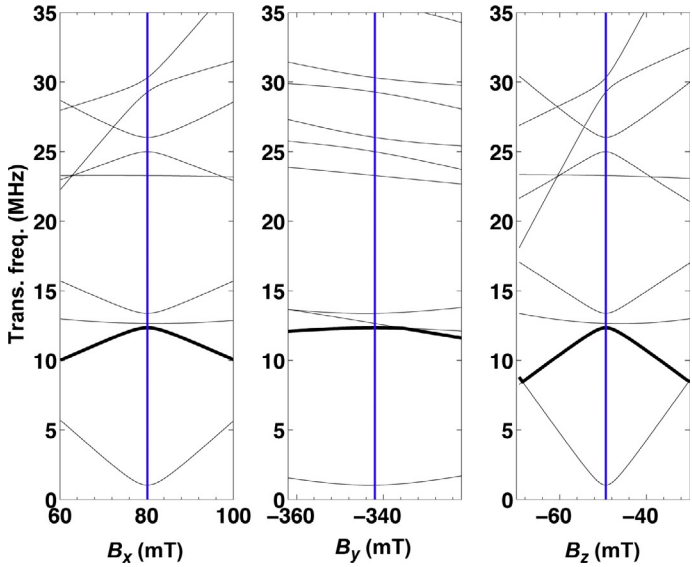

FIGURE 26 Calculated ground-state hyperfine transition frequencies as a function of an external magnetic field in Pr^{3+}:$La_2(WO_4)_3$. The transition denoted by a thick line is a ZEFOZ one for $B_x = 80$ mT, $B_y = -343$ mT, and $B_z = -49$ mT, corresponding to a frequency of 12.6 MHz (Lovrić et al., 2011).

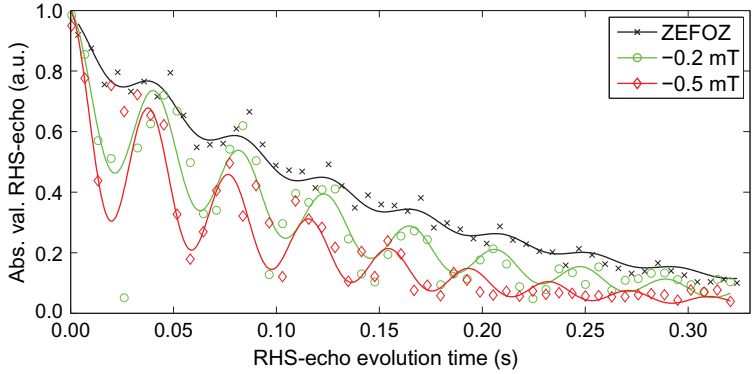

FIGURE 27 Hyperfine echo decays as a function of the delay between the excitation pulse and the echo in Pr^{3+}:$La_2(WO_4)_3$ for the ZEFOZ transition shown in Fig. 26 (Lovrić et al., 2011). Crosses: magnetic field at the ZEFOZ point; circles (diamonds): detuning of 0.2 (0.5) mT for the z component. Echo decay modulations are attributed to coupling with ^{139}La nuclear spins ($T = 2$ K).

magnitude larger than the zero field value of 0.25 ms. This highlights the remarkable efficiency of this technique, which has been also demonstrated in Pr^{3+}:Y_2SiO_5, with an increase in T_2^{hf} by a factor of 1700 (Fraval et al., 2004, 2005). The magnetic field must however be very precisely set, as deviations of a few 100s of μT, or fraction of degrees, lead to a fast decrease of T_2^{hf},

as seen in Fig. 27: a 0.15% decrease in the field magnitude leads to a 40% decrease in T_2^{hf}. Combining the calculated second-order derivatives for the ZEFOZ transition with the effect of small magnetic field detunings on T_2^{hf}, the host magnetic field fluctuations are determined to be about 1 μT and are likely due to flipping $^{139}La^{3+}$ spins. It should be noted that the ZEFOZ transition coherence lifetime is still far to be limited by the hyperfine T_1 contribution, as $T_1^{hf} = 16$ s (Guillot-Noël et al., 2007).

The ZEFOZ technique could also be used for hyperfine transitions of Kramers ions or for optical transitions (Ahlefeldt et al., 2013d; McAuslan et al., 2012). In these cases, T_1 is generally shorter, which would then set the limit on T_2 extension. Inhomogeneous broadening linked to magnetic field variations from one R ion site to another can also be reduced for ZEFOZ transitions (Pascual-Winter et al., 2012b).

Dynamical Decoupling

Although the ZEFOZ technique can extend coherence lifetimes by orders of magnitude, it relies on particular energy-level schemes and application of specific magnetic fields. It is therefore not applicable to all systems. Moreover, the transition structure at the ZEFOZ point can be very complex and dense (see Fig. 26), which makes spectral tailoring very difficult and is generally not favorable to absorption over large bandwidths. This may be a serious limitation in QIP applications. It may therefore be useful to use another technique to extend T_2, dynamical decoupling (DD). Originating from NMR spectroscopy (Carr and Purcell, 1954; Meiboom and Gill, 1958), DD consists typically in sending a train of π pulses after an initial $\pi/2$ one. This can extend the coherence lifetime if the environment fluctuations are slow enough so that they appear as an additional and static inhomogeneous broadening during the delay between the π pulses. This static broadening is then constantly refocused by the π pulses, resulting in an increased T_2 (Viola and Lloyd, 1998). Several DD sequences have been proposed to maximize T_2 for nonideal systems (inhomogeneous broadened transitions, pulse area errors, etc.) by using pulses with varying phases (Souza et al., 2012; Yang et al., 2010). In general, the relative phase of the pulses has to be defined very precisely, which explains that this technique is well suited to rf excitation and coherence extension of hyperfine or electronic Zeeman transitions.

An example of DD in a R-doped crystal is given in Fig. 28 (Fraval et al., 2005). In these experiments, a ground-state hyperfine transition of Pr^{3+}:Y_2SiO_5 is investigated under an external magnetic field tuned to a ZEFOZ point. This dramatically extends the coherence lifetimes from 0.5 to 860 ms. A DD sequence is then applied to the transition to further increase T_2^{hf}. It consists in a X $\pi/2$ pulse, followed by a train of N pairs of X and $-X$ π pulses, separated by a delay τ_c (Fig. 28). The alternating phases of the π pulses avoid accumulating rotation angle errors which would drive Bloch vectors out of the equatorial plane. The total cycling time is defined as $2N\tau_c$ and, for large N,

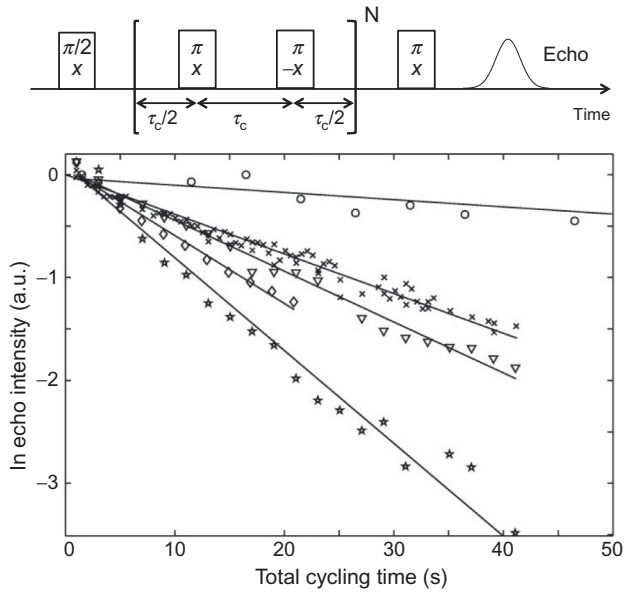

FIGURE 28 Echo intensity decays as a function of cycling time ($2N\tau_c$) for a ZEFOZ hyperfine transition in Pr^{3+}:Y_2SiO_5 under dynamical decoupling. The delay between π pulses is $\tau_c = 7.5$ (crosses), 10 (triangles), 15 (diamonds), and 20 ms (stars), corresponding to $T_2 = 27.9$, 21.1, 15.2, and 10.9 s. Population lifetime (circles) is $T_1 = 145$ s, $T = 1.5$ K. *Reproduced with permission from Fraval et al. (2005), © 2005 the American Physical Society (http://dx.doi.org/10.1103/PhysRevLett.95.030506).*

corresponds approximately to the time between the initial excitation and the echo. The echo signal is detected by the RHS technique (see Section 4.3.3). For a given τ_c, the final echo decay is recorded as a function of the total cycling time, obtained by increasing the number of pulses. As seen in Fig. 28, T_2^{hf} increases with decreasing τ_c. This is expected for low pulse error accumulation and corresponds to pulse delays becoming shorter than the characteristic times of the environment fluctuations. In this case, these fluctuations are due to magnetic field variations due to flipping ^{89}Y spins. In this example, the longest T_2^{hf} observed was 27.9 s, a 30-fold increase compared to the initial ZEFOZ value. Also shown in Fig. 28 is the hyperfine population lifetime decay, $T_1^{hf} = 145$ s, which sets an upper limit for T_2^{hf} of 290 s.

DD has also been used in Tm^{3+}:$Y_3Al_5O_{12}$ (Pascual-Winter et al., 2012b), Pr^{3+}:$La_2(WO_4)_3$ (Lovrić et al., 2013), and Eu^{3+}:Y_2SiO_5 (Arcangeli et al., 2014). On the other hand, it has been shown that pulses could be optimized to provide higher echo intensities after DD in Pr^{3+}:Y_2SiO_5 (Mieth et al., 2012). These pulses are in particular chirped in frequency to efficiently address the hyperfine inhomogeneous linewidth, a technique known as rapid adiabatic passage, which was also investigated in Tm^{3+}:$Y_3Al_5O_{12}$ (Lauro et al., 2011; Pascual-Winter et al., 2012a).

Although decoupling sequences can be very effective, it should be noted that QIP applications have specific requirements, compared to standard NMR spectroscopy. One important point is that DD sequences should preserve coherences for arbitrary input states. States created by pulses with $\pm X$, $\pm Y$ phases should therefore behave in the same way. Complex sequences have been designed to combine insensitivity to initial state, pulse errors, and long T_2 (Genov et al., 2014; Peng et al., 2011; Souza et al., 2011).

4.4 Currently Used Crystals

Properties of R-doped crystals such as optical coherence lifetime, inhomogeneous linewidth as well as oscillator strengths can be found for several dopant–host combinations in reviews and book chapters by Macfarlane and Shelby (1987a), Macfarlane (2002), Sun (2005), and Thiel et al. (2011). In this section, we give in Table 2 the optical and hyperfine parameters, when available, for a number of crystals which have been used in QIP experiments, including those used in the experiments discussed in Sections 5 and 6.

5 QUANTUM MEMORIES FOR LIGHT

5.1 Requirements

The most basic requirement for quantum memories for light (QML) is the ability to store and release a photonic qubit on demand. The second one is high fidelity, which means that the QML should operate as an identity operator. Input and output qubit states should therefore be as close as possible, a property measured by the fidelity parameter in QIP (Nielsen and Chuang, 2000). In rare earth-based QML, photonic qubits are usually implemented using single-photon polarization states (Clausen et al., 2012; Rieländer et al., 2014) or presence in time windows (time-bin qubits) (Usmani et al., 2010). In both cases, the quantum information signal is very weak and an important concern is that it can be easily buried into noise, i.e., photons without any relationship with the input state and present at the memory output. A fundamental source for these noise photons is spontaneous emission, which should be therefore strongly suppressed. High fidelity also requires high efficiency for the memory, i.e. a large probability to retrieve a photonic qubit after storage. Ideally, all input photons should be absorbed into the memory, whereas output photons should not. The next requirements are more dependent on the exact applications considered for a QML. For quantum repeaters for example, a long storage time is necessary, as well as a large bandwidth (Lvovsky et al., 2009; Tittel et al., 2010). The latter translates into storage of short light pulses and therefore of many qubit states during a given time interval. Storage of many qubits in a QML is called multimode storage and, for example, is important to obtain useful quantum repeaters (Afzelius et al., 2009).

TABLE 2 Optical and Ground-State Hyperfine Properties of Some R-Doped Crystals Used in QIP Experiments

	Optical					Hyperfine					
Crystal	λ (nm)	f ($\times 10^8$)	Γ_{inh} (GHz)	T_1 (μs)	T_2 (μs)	I	Γ_{inh} (kHz)	T_1 (s)	T_2 (ms)	$\Delta\Gamma$ (MHz)	γ_{max} (MHz/T)
$Pr^{3+}:Y_2SiO_5$[a]	605.977	30	4.4	164	111 152 (7 mT)	5/2	50	145	0.5 4.2×10^4 (Z+DD)	27.3	116
Pr^{3+}: $La_2(WO_4)_3$[b]	602.74	2	10.4	64	16	5/2	105	17	0.25 158 (Z), 4.2 (DD)	27.2	147
$Eu^{3+}:Y_2SiO_5$[c]	580.04	1.3	1.7	1970	1300 2600 (10 mT)	5/2	21	2×10^6	19 474 (DD)	96	11
$Er^{3+}:Y_2SiO_5$[d]	1536.48	26	0.18	11,000	3 4400 (7 T)						
Tm^{3+}: $Y_3Al_5O_{12}$[e]	793.38	8	17	800	81 110 (10 mT)	1/2	500 (0.5 T) 105 (1 T)	4.5 (0.45 T)	0.3 (0.15 T) 230 (1 T, DD)		400
Tm^{3+}: $LiNbO_3$[f]	794.22	200	300	160	11 23 (35 mT)						
$Nd^{3+}:Y_2SiO_5$[g]	883	30	6	300	90 (0.3 T)						
$Nd^{3+}:YVO_4$[h]	879.94	800	2	100	27 (1.5 T)						

The reader is referred to references for details on experimental conditions (magnetic field orientation, temperature, etc.). λ, wavelength (vac.); f, oscillator strength; Γ_{inh}, inhomogeneous linewidth; T_1, T_2, population and coherence lifetimes; $\Delta\Gamma$, maximum spectral hole width; I, nuclear spin; γ_{max}, maximal principal value of the Z gyromagnetic tensor; Z, ZEFOZ; DD, dynamical decoupling.
[a] *Site 1, 0.02% (Equall et al., 1995; Fraval et al., 2005; Heinze et al., 2013; Longdell et al., 2002; Lovrić et al., 2012; Nilsson et al., 2004).*
[b] *0.2% (Beaudoux et al., 2012; Guillot-Noël et al., 2007, ,2009; Lovrić et al., 2011, ,2013).*
[c] *Site 1, 0.1%, hyperfine data for ^{151}Eu (Arcangeli et al., 2014; Könz et al., 2003; Longdell et al., 2006).*
[d] *Site 1, 0.0015% (Böttger et al., 2009; Thiel et al., 2011).*
[e] *0.1% (Louchet et al., 2007, ,2008; Pascual-Winter et al., 2012b; Thiel et al., 2011).*
[f] *0.1% (Sun et al., 2012).*
[g] *Site 1, 0.003% (Usmani et al., 2010).*
[h] *0.001% (de Riedmatten et al., 2008; Sun et al., 2002).*

5.2 Protocols

A series of protocols designed to meet the above requirements in R crystals has been proposed over the past few years, with specific advantages and drawbacks. In the following, we briefly describe the main ones and in the next section discuss in more details a few experimental examples. Other schemes have been proposed but have not been developed to the same extent so far (Beavan et al., 2012; Goldschmidt et al., 2013; Lauro et al., 2009; Ledingham et al., 2012; Moiseev, 2013).

Electromagnetically Induced Transparency

The first protocol which was investigated for light storage in R-doped crystals is based on electromagnetically induced transparency (EIT) (Fleischhauer et al., 2005; Kuznetsova et al., 2002; Lukin, 2003). In a Λ system, a strong control light field is applied along one optical transition, creating a transparency window for a probe beam tuned to the other optical transition (Fig. 29). A coherence is also created between the two ground states as the probe beam propagates inside the sample. Moreover, the narrow transparency window results in a strong refractive index variation, which in turn slows down the probe pulse. If this effect is large enough, the probe pulse may be

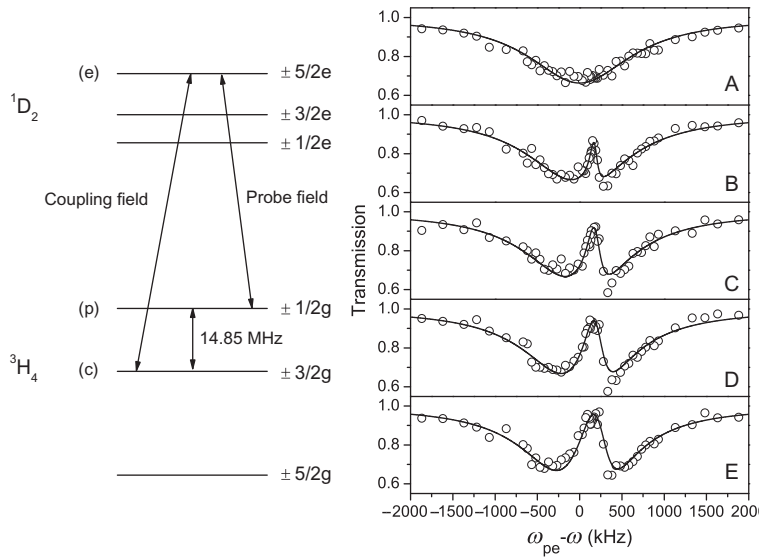

FIGURE 29 A transparency window obtained in Pr^{3+}:$La_2(WO_4)_3$ by EIT (Goldner et al., 2009). After spectral tailoring of the $^3H_4(0) \rightarrow {}^1D_2(0)$ inhomogeneous linewidth, a control (coupling) beam resonant with the $\pm 3/2g \leftrightarrow \pm 5/2e$ transition is shone on the crystal (left). When a probe beam of frequency ω scans the 1 MHz $\pm 1/2g \leftrightarrow \pm 5/2e$ transition centered at ω_{pe} (right), a transparency window appears in the center of the line. Its depth and width depend on the control field Rabi frequency ($\Omega/2\pi = 30$ (A), 150 (B), 230 (C), 280 (D), and 340 (E) kHz). $T = 2$ K.

entirely contained in the sample at a given time. If the control field is then slowly turned off, the optical coherence created by the probe pulse is transferred to a coherence between the ground state levels. When the control field is turned on again, the process is reversed and the probe pulse leaves the sample. If photonic qubits are used as the probe pulse, this stopped light process effectively constitutes a QML with a storage time corresponding to the coherence lifetime of the ground-state transition, typically involving hyperfine levels (Turukhin et al., 2001).

The efficiency and bandwidth of the EIT-based QML depend on the depth and width of the transparency window, which should be as high as possible. This requires a large Rabi frequency for the control field as well as a highly absorbing sample. EIT is therefore well adapted to systems with very strong optical transitions, like atomic vapors (Liu et al., 2001). In these cases, the optical coherence lifetime is short, dominated by T_1, but this plays no role in the EIT process. In opposition, the low f–f oscillator strengths make efficient and large bandwidths EIT memories very challenging to obtain in R-doped crystals (Ham et al., 1997; Heinze et al., 2013; Longdell et al., 2005). On the other hand, EIT directly stores quantum states in hyperfine levels, the coherence lifetimes of which are long and moreover can be efficiently extended (Section 4.3). Indeed, using a combination of ZEFOZ and DD techniques (Section 4.3.4), an EIT-based memory with very long storage time, up to 40 s, has been demonstrated in Pr^{3+}:Y_2SiO_5 (Heinze et al., 2013), following other experiments in the same host (Longdell et al., 2005; Turukhin et al., 2001).

Photon Echo

A second type of protocols is based on the two-pulse photon echo (Section 4.3). Here, an ensemble of R ions with an inhomogeneously broadened absorption line absorbs the incoming photonic qubit, i.e., a single photon. This is equivalent to the first step of the photon-echo scheme, except that the exciting pulse has now a very small area instead of $\pi/2$. If a π pulse is then applied after a time τ, an echo is emitted at 2τ and corresponds to the output of the memory. As a photonic qubit, the echo quantum state is identical to that of the input state, expect for a π-phase shift (Fig. 7). The storage time τ_s is limited by the transition coherence lifetime T_2, although for high efficiency, it should be significantly shorter. For example, to get an echo with 90% of the intensity extrapolated at zero storage time, τ_s cannot exceed $0.05T_2$. It can be however extended by transferring the optical coherence to a hyperfine one (see below). Despite these favorable properties, the two-pulse photon echo cannot work as a high-fidelity QML because of output noise (Ruggiero et al., 2009). After absorption of a single photon, the R ions are still mainly in the ground state. After the rephasing π pulse, they are driven to the excited state and will start to relax through spontaneous emission and amplify the reemitted echo by stimulated emission. Both processes produce additional

photons, i.e., noise, at the output of the memory which degrades its fidelity. QML protocols have therefore to achieve rephasing without creating a large population in the excited state (Sangouard et al., 2010) and some examples are discussed below.

Controlled Line Broadening: CRIB and GEM

In the photon-echo scheme, the π pulse reverses the atomic phase evolution (see Section 3.2): before the π pulse, $\phi(t) = \omega t$ and after it $\phi(t) = \phi_0 - \omega t$. The same effect can be obtained without a π pulse by changing the sign of ω. This is achieved by the CRIB (controlled reversible inhomogeneous broadening) (Nilsson and Kröll, 2005) and GEM (gradient echo memory) (Alexander et al., 2006) protocols.

Here, an inhomogeneous transition of center frequency ω_0 and width $\Delta\omega$ is broadened by an electric field gradient by the linear Stark effect. An ion at frequency $\omega_0 + \omega$ is shifted to $\omega_0 + \omega + c_S(\omega - \omega_0)$, where c_S is the Stark coefficient. Then, the input signal is absorbed and after a delay τ, the ion has a relative phase of $\phi(t) = [\omega + c_S(\omega - \omega_0)]\tau$. The electric field is now reversed and at a later time t, the phase is $\phi(t) = [\omega + c_S(\omega - \omega_0)]\tau + [\omega - c_S(\omega - \omega_0)](t - \tau)$. At $t = 2\tau$, $\phi(t) = 2\tau\omega$ and an echo is emitted. Its intensity is proportional to the integral given in Eq. (6) and decays as $T_2^* \approx 1/\Delta\omega$. The memory storage time τ_s is therefore determined by the width of the transition before broadening by the electric field and $\tau_s \ll 1/\Delta\omega$ is required for high efficiency. The initial peak, which is limited by the homogeneous linewidth, should therefore be as narrow as possible, with Γ_h as a lower limit.

The protocol starts with a narrow peak created by optical pumping within the inhomogeneous linewidth. It is then broadened to match the bandwidth of the incoming pulse. As Stark coefficients in R-doped crystals are typically in the range of 10s of kHz/(V/cm), MHz bandwidths can be reached by about 100 V across a few mm (Macfarlane, 2007). The width of the absorption peak which can be created may however be limited by the levels used for population storage, as in spectral tailoring experiments (Section 4.1.2). CRIB and GEM differ by the direction of the electric field gradient applied to the sample: in CRIB, the gradient is transverse with respect to the light propagation, whereas in GEM it is longitudinal, potentially achieving higher bandwidths for crystals with very low inhomogeneous linewidths. In the case of CRIB, for an absorption coefficient α after broadening and a sample thickness L, the memory efficiency, i.e., the ratio between output and input pulse intensities, is given at zero storage time by:

$$\eta_{\mathrm{CRIB}} = (\alpha L)^2(1 - \exp(-\alpha L)) \tag{21}$$

and by

$$\eta_{\mathrm{GEM}} = (1 - \exp(-\alpha L))^2 \tag{22}$$

in the case of GEM (Tittel et al., 2010). It can be seen that at high optical density, the GEM protocol reaches unit efficiency, but is limited to 54% for $\alpha L = 2$ in CRIB, unless transfer pulses are added to the protocol (see below). It should also be noted that high opacity (αL product) coupled to large bandwidths is difficult to obtain in the CRIB/GEM protocols. The initial narrow line, needed to increase storage time, is likely to be weakly absorbing and furthermore has to be broadened to match the requested bandwidth. As an example, to reach 90% efficiency, the broadened line should have an opacity $\alpha L = 3$ Eq. (22), which translates into an opacity of $\alpha L = 300$ for an initial 10 kHz linewidth ($T_2^* = 30\mu s$) broadened to 1 MHz.

CRIB/GEM has been studied in Pr^{3+}:Y_2SiO_5 (Hedges et al., 2010; Hétet et al., 2008), Eu^{3+}:Y_2SiO_5 (Alexander et al., 2006), and Er^{3+}:Y_2SiO_5 (Lauritzen et al., 2010).

Double Rephasing: ROSE and HYPER

Another approach consists in extending the two-pulse photon-echo scheme by adding a second π pulse after the first one (Fig. 30). The echo observed after this second pulse is produced in a ensemble of ions in the ground state so that the noise created by spontaneous emissions disappears. For this scheme to work as a QML, it is however necessary to avoid the echo emission at the time 2τ, i.e., after the first π pulse. In the ROSE (revival of silenced echo) protocol (Damon et al., 2011), the two π pulses are propagating in opposite direction with respect to the input signal, which cancels the first echo but not the second one, due to spatial phase matching conditions (Fig. 30). An electric field gradient is used in the HYPER (hybrid photon-echo rephasing) protocol to broaden the transition between the input and the first π pulse (McAuslan et al., 2011b). This broadening is not rephased and reduces the first, unwanted, echo to an arbitrary low intensity. Another electric field gradient applied between the two π pulses cancels the phase shifts produced by the first electric field. An echo therefore appears after the second π pulse (Fig. 31). In ROSE and HYPER, the storage time is directly determined by the optical coherence lifetime T_2. At zero storage time, efficiency is given by Eq. (21) when the echo is emitted in the forward direction (i.e., in the same direction as the input pulse). Unit efficiencies can be obtained for backward echo emission but require more complex beam configurations in ROSE. A major advantage of these protocols is that no spectral tailoring is needed, which allows directly using the inhomogeneous linewidth and therefore the total available optical density and bandwidth. High efficiency is therefore easier to obtain (Dajczgewand et al., 2014). On the other hand, low noise at the memory output can be achieved only if the π pulses can invert population efficiently, which appears to be quite difficult in strongly absorbing samples.

ROSE/HYPER has been investigated in Tm^{3+}:$Y_3Al_5O_{12}$ and Er^{3+}:Y_2SiO_5 (Dajczgewand et al., 2014; Damon et al., 2011) as well as in Pr^{3+}:Y_2SiO_5 (McAuslan et al., 2011b).

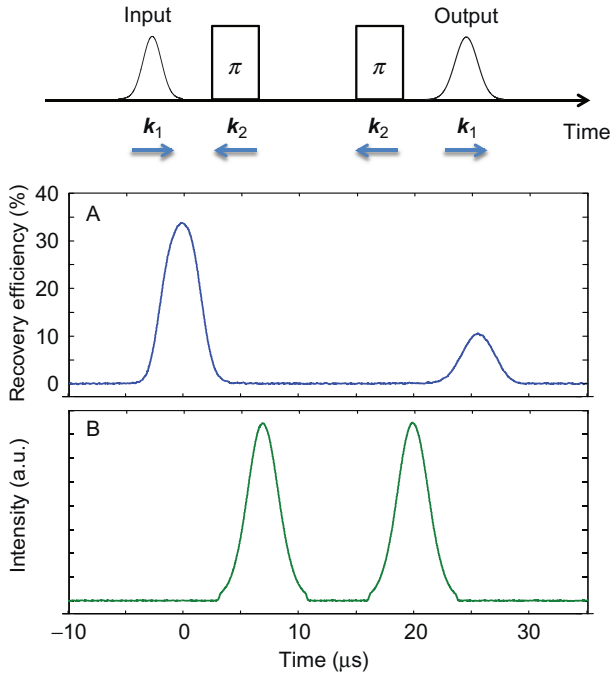

FIGURE 30 Storage by the ROSE (revival of silenced echo) protocol. Two π pulses avoid producing an echo within an inverted ensemble of ions. To cancel the intermediate echo, the input and output pulses propagate in a direction opposite to that of the π pulses as shown by the $\boldsymbol{k}_i$ wave vectors under the protocol scheme. Experimental data recorded in Tm^{3+}:$Y_3Al_5O_{12}$ ($T = 2.8$ K): transmitted input and output pulses (A) and π pulses (B). *Reproduced with permission from Damon et al. (2011), © 2011 IOP Publishing & Deutsche Physikalische Gesellschaft. CC BY-NC-SA.*

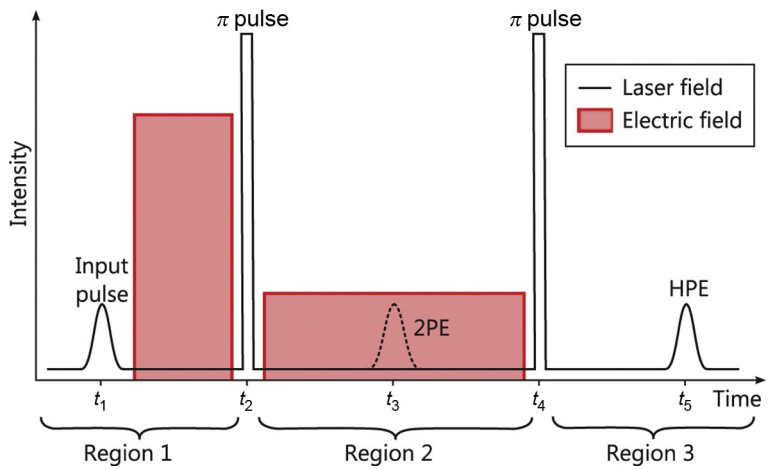

FIGURE 31 The HYPER (hybrid photon-echo rephasing) protocol. The echo after the first π pulse (dotted line) is canceled by the first electric field pulse. The second electric field pulse cancels the phase shift produced by the first one and an echo (labeled HPE) is observed after the second π pulse. *Reproduced with permission from McAuslan et al. (2011b), © 2011 the American Physical Society (http://dx.doi.org/10.1103/PhysRevA.84.022309).*

Atomic Frequency Comb

An echo can also be produced by a proper spectral tailoring of the inhomogeneous broadening, as shown by the AFC (atomic frequency comb) protocol (Afzelius et al., 2009; de Riedmatten et al., 2008). Here, a number of absorbing peaks of width γ and frequency separation $\Delta\omega$ are created by spectral tailoring (Fig. 32). The total bandwidth spanned by the comb should be larger than the input pulse one. At a delay τ after absorption, ions in peak N have an additional dephasing $\phi = N\Delta\omega\tau$ compared to ions in peak $N = 0$. At time $\tau = 2\pi/\Delta\omega$, dephasing in all peaks are multiples of 2π, the integral in Eq. (6) is nonzero, and an echo is emitted. This scheme has similarities with the three-pulse echo (Section 4.3.3), where the third pulse is diffracted by the spectral grating created by the first two pulses. In opposition to the previous protocols, the AFC only introduces a delay and the storage time given by the frequency comb separation is fixed, $\tau_s = 2\pi/\Delta\omega$. It can be converted to the required on-demand protocol by transferring the optical coherence to a spin one (see below). As CRIB/GEM, AFC is a low-noise protocol, as no π pulse is used for rephasing. Another advantage of this protocol is its bandwidth, which corresponds to the comb that can be created by optical pumping and is independent of the memory efficiency. However, the bandwidth which can be effectively obtained may be limited by the levels used for population storage, as in CRIB/GEM. This can be overcome if the comb period coincides

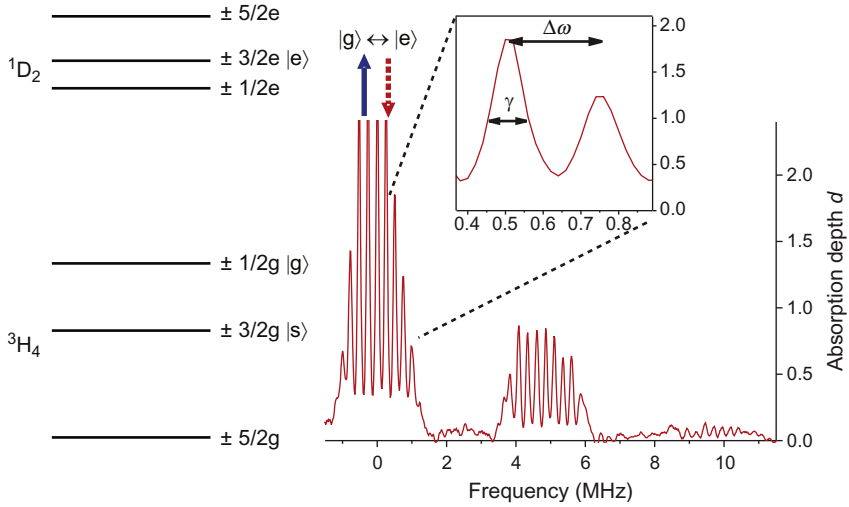

FIGURE 32 Spectral tailoring for the AFC (atomic frequency comb) protocol in Pr^{3+}:Y_2SiO_5. The input signal is absorbed along the $\pm 1/2g \leftrightarrow \pm 3/2e$ transition between ground and excited hyperfine levels. Optical pumping stores population in the ± 5/2g ground-state hyperfine level ($T = 2$ K). *Reproduced with permission from Afzelius et al. (2010b), © 2010 the American Physical Society (http://dx.doi.org/10.1103/PhysRevLett.104.040503).*

with level splittings (Bonarota et al., 2011). The efficiency of the AFC memory depends on the width of the comb teeth, since this broadening is not rephased in the protocol. The echo intensity is proportional to $\exp(-c/F^2)$ where $F = \Delta\omega/\gamma$ is the comb finesse and c a constant depending on the teeth spectral shape. A large finesse is therefore favorable to low dephasing and large efficiency. On the other hand, for a given comb spectral structure, zero storage time efficiency in the forward direction is given by Eq. (21), where αL is divided by the comb finesse F. A compromise has therefore to be found between reducing the dephasing effects due to the teeth width (large F), and high comb absorption (low F). A high absorbing, high finesse comb therefore requires a sample with a large opacity prior to spectral tailoring. As an example, with $F = 10$, 90% efficiency is obtained with $\alpha L = 40$, using a backward scheme with transfer pulses (see below). As an alternative to high absorbing samples, it is possible to place the crystal into a cavity, which transmission is adjusted to the sample opacity so that the incoming light is completely absorbed (Afzelius and Simon, 2010; Sabooni et al., 2013).

AFC storage has been obtained in Nd^{3+}:YVO_4 (de Riedmatten et al., 2008; Zhou et al., 2012), Nd^{3+}:Y_2SiO_5 (Bussières et al., 2014; Clausen et al., 2011, 2012; Usmani et al., 2010, 2012), Tm^{3+}:$Y_3Al_5O_{12}$ (Bonarota et al., 2010, 2011; Chanelière et al., 2010), Pr^{3+}:Y_2SiO_5 (Afzelius et al., 2010b; Gündoğan et al., 2012; Rieländer et al., 2014; Sabooni et al., 2013), Eu^{3+}:Y_2SiO_5 (Timoney et al., 2012, 2013), and Tm^{3+}:$LiNbO_3$ waveguides (Jin et al., 2013; Saglamyurek et al., 2011).

Coherence Transfer to Hyperfine Transitions

In contrast to EIT, the photon echo-based schemes have storage times limited by the optical T_2 in the best cases. To reach longer times, additional pulses can be inserted in the previous protocols to transfer quantum states between optical and hyperfine transitions (Afzelius et al., 2009; Damon et al., 2011; Nilsson and Kröll, 2005). As described in Section 3.1, this can be achieved by using a Λ system. It is then possible to take advantage of the long nuclear spin coherence lifetimes (Section 4.3). Furthermore, hyperfine T_2 extension methods (Section 4.3.4) can also provide dramatic improvement of storage times. As mentioned above, transfer pulses also enable backward emission of the echo in CRIB/GEM and AFC, a configuration for which unit efficiency can be reached. Photon echo-based memories with transfer to hyperfine coherences have been reported in Pr^{3+}:Y_2SiO_5 (Afzelius et al., 2010b), Eu^{3+}:Y_2SiO_5 (Timoney et al., 2012, 2013), and Pr^{3+}:$La_2(WO_4)_3$ (Lovrić et al., 2013).

5.3 Entanglement Storage in Nd:Y_2SiO_5

The first example we describe is a QML based on a 30-ppm at.% Nd^{3+}:Y_2SiO_5 crystal, using an AFC protocol (Clausen et al., 2011). The photonic

qubit to store is part of an entangled pair of photons (signal and idler) generated by spontaneous downconversion in a nonlinear crystal. The state of the pair is of the form $|0_a\rangle|0_b\rangle + |1_a\rangle|1_b\rangle$, where a,b label the photons. One photon of the pair (the signal) is stored in the crystal where a comb has been created by spectral tailoring. The transition used is the $^4I_{9/2}(0) \leftrightarrow {}^4F_{3/2}(0)$ of Nd^{3+} isotopes with zero nuclear spins. Its inhomogeneous linewidth is 6 GHz with a peak absorption coefficient of $\alpha \approx 3\ cm^{-1}$. A magnetic field of 300 mT is applied to the sample perpendicular to the crystal b axis, resulting in an electronic Zeeman splitting of the excited and ground states of, respectively, 2.1 and 10 GHz. Two lines can therefore be separated in absorption, both with $\alpha \approx 1.5\ cm^{-1}$. The ground-state upper Zeeman level has a population lifetime of 100 ms at 3 K, which is large enough, compared to the excited-state lifetime of 300 μs, to allows population storage. A comb with a bandwidth of 120 MHz and with a finesse of $F = 2$ is then created by spectral tailoring and used in a double-pass configuration to increase absorption (Fig. 33). The teeth width ($\gamma = 2\pi \times 20$ MHz) largely exceeds the transition homogeneous linewidth (3.5 kHz). With these parameters, the storage time is $\tau_s = 2\pi/\Delta\omega = 2\pi/(F\gamma) = 25$ ns and the efficiency reaches 21%. It should be noted that one challenging aspect of the experiment is that the bandwidth of the signal photon, emitted from a parametric downconversion source, has to be reduced by a factor of 10^4 to match the memory bandwidth.

The photon reemitted from the memory is then detected as well as the one which was not stored (idler). The states $|0\rangle$ and $|1\rangle$ correspond to different times of creation of the photons. Because of entanglement, if one photon is detected at a given time, so is the other one. Entanglement between the stored and retrieved signal and idler photons is therefore revealed by coincidence measurements. When the probability of coincidence detection P_{si} is larger

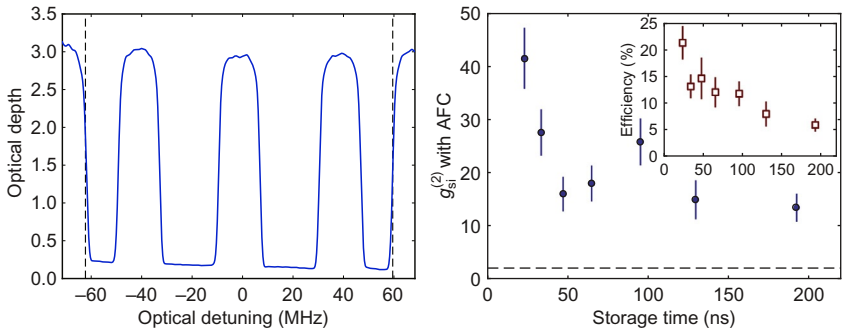

FIGURE 33 AFC quantum memory in Nd^{3+}:Y_2SiO_5. Left: comb created in the $^4I_{9/2}(0) \rightarrow {}^4F_{3/2}(0)$ transition by spectral tailoring and population storage in the upper electronic Zeeman ground state. Right: nonclassical correlations ($g^{(2)} > 2$, dashed line) for an entangled photon pair after storage and retrieval of one of the photon. At long storage times, the reduced memory efficiency (inset) reduces $g^{(2)}$. $T = 3$ K. *Reproduced with permission from Clausen et al. (2011), © 2011 Macmillan Publishers Ltd: Nature.*

than twice the product of the probabilities of signal (P_s) or idler (P_i) detection, nonclassical correlations occur, as measured by $g^{(2)} = P_{si}/(P_sP_i)$. This is observed for storage times up to 200 ns (Fig. 33), demonstrating that the memory preserves entanglement. Further analysis also shows that entanglement also exists between the idler photon and the atoms during storage. Similar experiments were performed at the same time in Tm^{3+}:$LiNbO_3$ waveguides (Saglamyurek et al., 2011).

5.4 High Efficiency Memory in Pr:Y_2SiO_5

The second memory we discuss uses the GEM protocol in a 500-ppm, 20-mm long, Pr^{3+}:Y_2SiO_5 crystal (Hedges et al., 2010). This length is chosen to obtain high absorption, and after spectral tailoring, a narrow peak with a width of 140 kHz and an opacity of 32 is created in the $^3H_4(0)\rightarrow{}^1D_2(0)$ transition of ions in site 1. In Pr^{3+}:Y_2SiO_5, the ground-state hyperfine levels have a population lifetime of about 100 s, very long compared to the excited-state lifetime of 164 μs, which is favorable to efficient optical pumping (Equall et al., 1995; Nilsson et al., 2004). Moreover, as in Pr^{3+}:$La_2(WO_4)_3$ (Section 4.1.4), the low site symmetry (C_1) of Pr^{3+} site results in significant branching ratios between ground- and excited-state hyperfine levels even at zero external magnetic field (Nilsson et al., 2004). The spectral tailoring is performed using a highly stabilized laser (1 kHz bandwidth) exciting the sample from the side, so that its intensity, and therefore the spectral tailoring process, does not vary along the sample. This is necessary given the high absorption of the sample. The electric field gradient is produced by electrodes in a quadrupole configuration and voltages up to $\pm$20 V, allowing broadening of the absorption to 1.6 MHz. This corresponds to the memory bandwidth, whereas the storage time is determined by the initial peak width, corresponding to $T_2^* = 3$ μs. For a storage time of about 1.4 μs, the echo produced by inverting the electric field intensity is 69% of that of the input pulse, which is one of the largest efficiencies reported for any quantum memory (Fig. 34). Finally, measurements with strongly attenuated input pulses show that the memory output noise is negligible, validating the quantum nature of the memory.

5.5 Long Storage with High Fidelity in Pr:$La_2(WO_4)_3$

Storage time extension by transferring the optical coherence to a spin one, and then use the coherence control techniques discussed in Section 4.3.4, has been studied in a 0.2 at.%-doped Pr^{3+}:$La_2(WO_4)_3$ crystal (Lovrić et al., 2013). The level scheme used is shown in Fig. 35 and takes advantage of the favorable branching ratios between the $\pm$1/2g $\rightarrow\pm$5/2e and $\pm$3/2g $\rightarrow\pm$5/2e transitions, due to the low site symmetry of Pr^{3+}, to obtain a Λ system (Fig. 15 and Section 4.1.4). First, spectral tailoring is used to isolate the $\pm$1/2g $\rightarrow\pm$5/2e and $\pm$3/2g $\rightarrow\pm$5/2e transitions and produce a large population in the

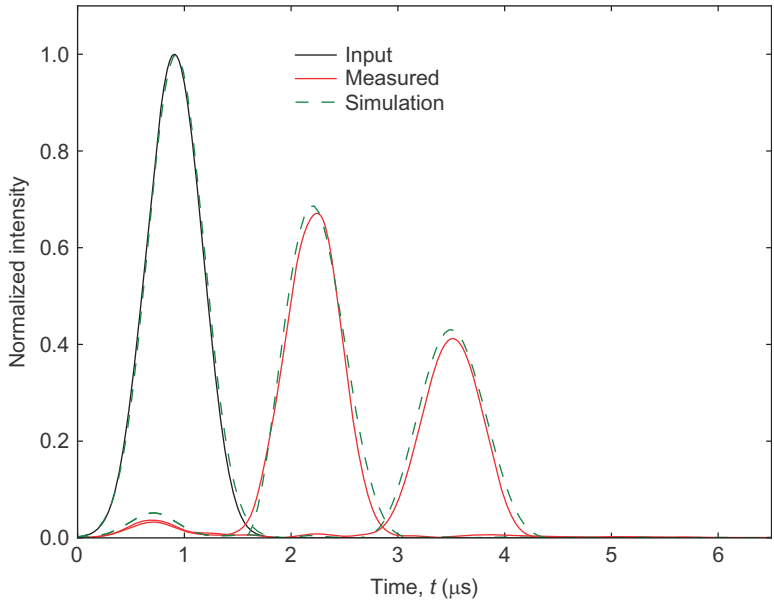

FIGURE 34 Input pulse (centered at ≈1 μs) and echo intensities obtained with the GEM protocol in Pr^{3+}:Y_2SiO_5 on the $^1D_2(0)\leftrightarrow{}^3H_4(0)$ transition after storage times of 1.4 and 2.8 μs. $T = 3$ K. *Reproduced with permission from Hedges et al. (2010), © 2010 Macmillan Publishers Ltd.: Nature.*

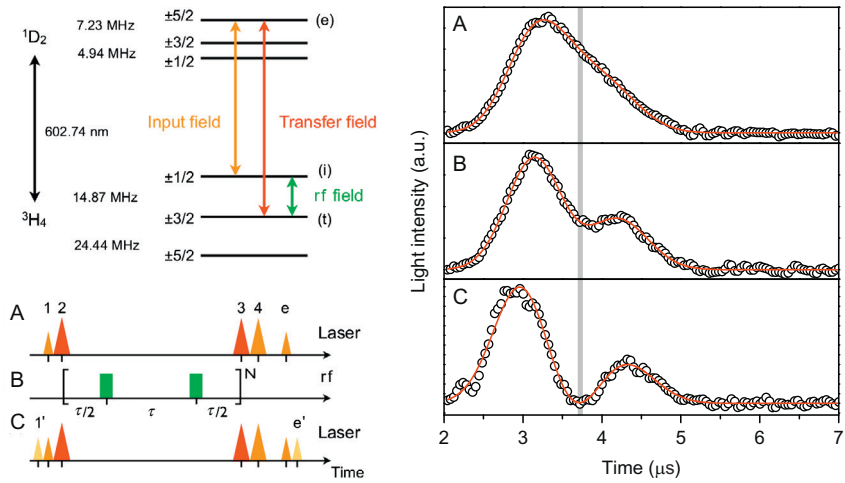

FIGURE 35 Left: energy levels and transitions used in a two-pulse photon-echo memory with coherence transfer to spin states (Lovrić et al., 2013). (A–C) Laser and rf pulse sequences (see text). Right: output signal of the memory when two input pulses with varying relative phase ϕ are stored. The corresponding output pulses overlap because of the limited memory bandwidth. As ϕ is preserved by the memory, a high visibility interference is observed at the time denoted by the vertical gray line. $\phi = 0^\circ$ (A), -270° (B), -180° (C). $T = 5$ K.

$\pm 1/2g$ level, whereas $\pm 3/2g$ is empty. The resulting memory bandwidth is 1.5 MHz. The input field (pulse 1 in Fig. 35, sequence A) is then absorbed along the (i)–(e) transition and the resulting optical coherence transferred to the ground states by applying a π pulse to (t)–(e) (pulse 2). Coherence control by DD is achieved by applying rf π pulses to the (t) $\leftrightarrow$ (i) hyperfine transition (sequence B). The hyperfine coherence is transferred back to the optical transition by pulse 3 and the optical dephasing reversed by pulse 4. The echo which is finally emitted (pulse e) is the memory output. The protocol used is the two-photon echo, which is too noisy to be used directly as a QML protocol (Section 5.2). Results should be however applicable to photon echo-based QML protocols.

Without transfer to the hyperfine transition, the memory storage time is determined by the optical coherence lifetime $T_2 = 11.5$ μs. The sequence described above allows increasing the effective T_2 of the memory to 8.4 ms. This is obtained by a simple series of rf π pulses, which is not efficient as preserving arbitrary quantum states (see Section 4.3.4). Since the optical and rf pulses have no phase relationship, the hyperfine quantum state which has to be controlled is indeed arbitrary. To achieve a better control, a more complex rf sequence is used and indeed the memory efficiency increases at short storage times. Fidelity of the memory could be checked by measuring the optical phase of the output pulse with respect to the input one. However, the laser stability is not good enough over storage times of several ms. Instead, two input pulses are stored in the memory (sequence c in Fig. 35, additional input and output pulses $1'$ and e'). The relative phase of the optical pulses is then varied, producing an interference between the output pulses, which overlap due to the broadening induced by the memory bandwidth (Fig. 35). The interference visibility of ≈ 1 shows that the DD sequence does not alter the memory fidelity.

5.6 Other Results

Recent achievements in QML in R-doped crystals include light-matter teleportation (Bussières et al., 2014), entanglement storage (Clausen et al., 2011; Saglamyurek et al., 2011), entanglement of two crystals (Usmani et al., 2012), memory efficiencies above 50% (Hedges et al., 2010; Sabooni et al., 2013), GHz bandwidth storage (Bonarota et al., 2011; Saglamyurek et al., 2011), as well as storage times over 1 min (Heinze et al., 2013). All these parameters are individually close or higher than the requirements for applications like quantum repeaters. However, it has not been yet possible to achieve them simultaneously in the same crystal/dopant configuration. Progress in this direction is likely to result from improved material and protocols but also from better quantum states control and transfer, narrower single-photon sources (Fekete et al., 2013), and high-efficiency detectors (Marsili et al., 2013).

Nd^{3+}- and Er^{3+}-doped crystals have also been recently proposed and studied as quantum memories for microwave photons (Afzelius et al., 2013; Probst et al., 2013; Staudt et al., 2012). In this case, protocols such as ROSE could be applied to an electronic Zeeman transition set at the microwave photon energy (a few GHz) by a magnetic field. In this way, a R-doped crystal could provide a memory for superconducting quantum processors, with the added advantage of a possible quantum interface with light.

6 QUANTUM COMPUTING

6.1 Schemes

As mentioned in Section 2.2, Di Vincenzo has summarized the requirements for a quantum computer into five essential criteria (DiVincenzo, 2000):

1. the qubits are well characterized and can be addressed individually. The system properties do not change with the number of qubits, i.e., the system is scalable.
2. qubits can be initialized to a well-defined state.
3. the qubit coherence lifetime is long enough compared to gate operation so that error correction codes can be used.
4. the qubit state can be measured at the end of the computation.
5. a universal set of quantum gates exist between any pair of qubits.

In well-chosen R-doped crystals, a qubit defined as a transition between ground-state hyperfine level can fulfill these criteria, if a Λ system including an excited state is available (Ohlsson et al., 2002). The relevant level scheme is shown in Fig. 5. First of all, static and dynamical properties of hyperfine transitions can be accurately determined by various techniques, as described in Sections 4.1 and 4.3. Combined rf and optical excitations are a highly useful tool in this respect. The qubit is therefore well characterized (1). Individual addressing of qubits can be achieved by optical excitation. The number of qubits which can be selected is proportional to the ratio between inhomogeneous and homogeneous linewidths but a stronger limitation comes from the interactions between qubits that are necessary to implement two-qubit gates. The scalability criterion is discussed below.

Qubit initialization (2) is obtained by optical pumping which can efficiently transfer populations between hyperfine levels (Section 4.1.2). If further spectral tailoring is needed to isolate the optical transitions corresponding to a qubit within the inhomogeneous linewidth, an additional storage level is required, like a third ground-state hyperfine level. Hyperfine coherence lifetimes (3) can reach 10s of ms and up to 10s of seconds, if coherence control techniques are used (Section 4.3.4). As the typical optical π pulse duration is about 1 μs, which gives the order of magnitude of a gate duration, a large number of operations can be performed, before superposition states are lost. Qubit state readout (4) can also be obtained by optical excitation. Quantum algorithms designs

require unambiguous determination of states $|0\rangle$ and $|1\rangle$ (Nielsen and Chuang, 2000). For this purpose, a laser is applied to the $|0\rangle \leftrightarrow |1'\rangle$ transition (Fig. 5). If the qubit to be read is in state $|0\rangle$, it is excited by the laser to $|1'\rangle$ and fluorescence can be detected, whereas if it is in state $|1\rangle$, the laser is not absorbed and no fluorescence is emitted.

Single-qubit gates (5) can be implemented using the optical transitions of the Λ system. As an example, we describe a pulse sequence corresponding to a NOT gate (Fig. 36). The initial state is assumed to be $(|0\rangle + \mathrm{i}|1\rangle)/\sqrt{2}$. A first π pulse is applied to the $|0\rangle \leftrightarrow |1'\rangle$ transition, producing the $(|1'\rangle + \mathrm{i}|1\rangle)/\sqrt{2}$ state. A second π pulse on the $|1'\rangle \leftrightarrow |1\rangle$ transition results in the state $(|1\rangle + \mathrm{i}|1'\rangle)/\sqrt{2}$, which is finally changed to $(|1\rangle + \mathrm{i}|0\rangle)/\sqrt{2}$ by a third π pulse applied to $|0\rangle \leftrightarrow |1'\rangle$. The complete sequence exchanges the $|0\rangle$ and $|1\rangle$ coefficients in the initial qubit state and performs a NOT gate. By varying the pulse phases, it is possible to perform an arbitrary single-qubit logic gate.

A two-qubit gate, which is a key requirement in a quantum computer, is also possible, if permanent electric dipole moments differ between ground and excited states (Macfarlane, 2007). As an example, a CNOT gate implementation is shown in Fig. 37. A laser resonant with the $|0\rangle \leftrightarrow |1'\rangle$ transition is first applied to the control qubit. When the control qubit is in state $|1\rangle$, it is not affected by this excitation. A NOT gate is then applied to the target qubit. On the other hand, when the control qubit is in state $|0\rangle$, it is excited to $|1'\rangle$ by the laser. The permanent electric dipole moment in $|1'\rangle$ is different from the one in $|0\rangle$ or $|1\rangle$ and shifts the optical transitions of the target qubit out of resonance with respect to the pulses of the NOT gate. The control qubit stays therefore in its initial state. This scheme performs a NOT gate on the target qubit only when the control qubit is in the $|0\rangle$ state, and corresponds to a CNOT gate (Ohlsson et al., 2002).

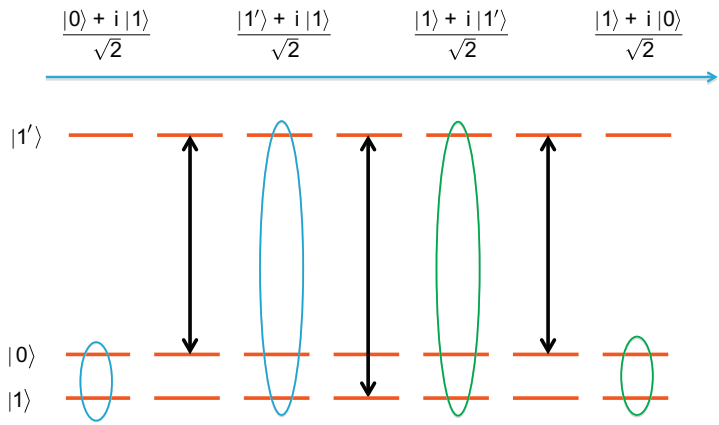

FIGURE 36 Pulse sequence corresponding to a NOT gate. Initial $(|0\rangle + \mathrm{i}|1\rangle)/\sqrt{2}$, final $(|1\rangle + \mathrm{i}|0\rangle)/\sqrt{2}$, and intermediate states are shown above the level schemes. Ellipsoids denote superposition states and arrows the transitions excited by the pulses.

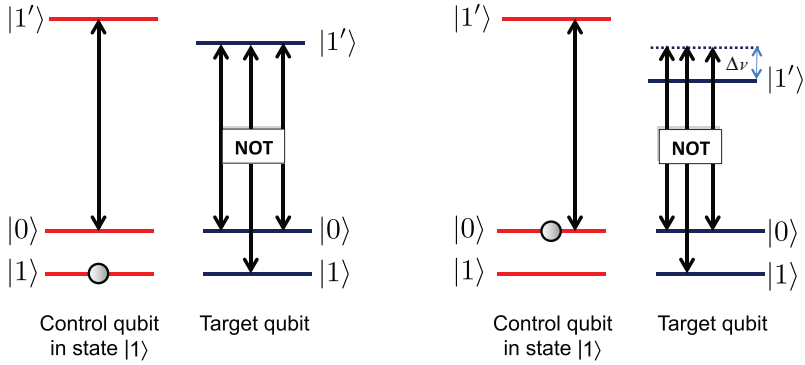

FIGURE 37 A CNOT gate between two qubits (see text).

The Di Vincenzo criteria for qubit control can, at least in principle, be fulfilled using these schemes which address hyperfine qubits by optical transitions. The remaining requirement is scalability and is the most difficult to satisfy. In general, two approaches can lead to a system with a large number of qubits. The first one defines the qubit as an ensemble of identical physical systems. Here, it would be the R ions in a given sample volume having their optical transitions at the same frequency. A first problem is that all optical pulses used to control the qubit states must act on all ions representing the qubit in the same way. Effect of inhomogeneous laser intensity, and therefore Rabi frequencies, due to absorption along the sample and transverse beam profile, must be kept very low. Moreover, the hyperfine inhomogeneous broadening of the ion ensemble is also a concern since it creates ion-dependent phase shifts on the hyperfine coherences. These effects can be greatly reduced by using schemes based on composite pulse sequences, which are robust against these different inhomogeneities (Genov et al., 2014; Roos and Mølmer, 2004). The next difficulty comes from the electric interaction which enables the two-qubit gate. First of all, interacting ions have to be close enough to produce frequency shifts larger than the optical homogeneous linewidth. This is however not a too stringent requirement (Ahlefeldt et al., 2013a; Longdell and Sellars, 2004; Ohlsson et al., 2002). A more serious one is encountered in doped crystals, where no correlation exists between the optical frequencies and the spatial distribution of ions. In this case, the number of ions representing a qubit decreases exponentially with the number of qubits (Wesenberg et al., 2007). Indeed, the fraction $p(N)$ of clusters of N ions separated by the same distance and having the same optical frequencies varies approximately as $[p(2)]^{N-1}$. The readout operation, which is based on fluorescence, becomes very difficult with increasing N and an alternative scheme with an auxiliary ion has to be used (see below). To create a position–frequency correlation for a large number of qubits, it has been proposed to use a "stoichiometric" crystal, i.e., fully doped with the qubit ions

(Ahlefeldt et al., 2013a). When such a material is doped with an impurity, the qubit ions close to it will have their optical frequencies shifted in the form of satellite lines. Each of these satellite lines corresponds to ions in a well-defined position relative to the impurity. Relative positions between ions in different satellite lines are therefore also well defined, which achieves the desired correlation. The number of qubits corresponds approximately to the resolved satellite lines.

An opposite approach to scalability consists in considering only one ion, a single instance, per qubit (Wesenberg et al., 2007). In this case, the problem of inhomogeneity disappears as the excitation parameters can be adjusted for each ion. However, the read out of a qubit state depends now on detecting the fluorescence of a single ion. This is possible with strong transitions for which the excited state decays primarily to the ground state (closed transitions). The transition can then be excited enough times to reliably detect a photon. f–f transitions are weak and emission rates are small, making them difficult to detect in single ions. Detecting a single-qubit ion is also not easy: if a laser excites an ion in the $|0\rangle$ state, it may then decay to another hyperfine ground state, which prevents a reliable measurement of its initial state. An additional "bus" ion has therefore to be used. It should have a strong closed transition, like a 4f–5d one, to enable single ion detection. The qubit readout is then performed by combining fluorescence with an interaction-induced frequency shift. First, as in the ensemble approach, a laser is tuned to the $|0\rangle \leftrightarrow |1'\rangle$ transition and excites the qubit ion only if it is in the $|0\rangle$ state. A second laser excites the bus ion and its fluorescence is detected. When the qubit ion is excited, the difference in permanent electric dipole moments, between excited and ground states, shifts the bus ion frequency out of resonance and no fluorescence is detected during the excited-state lifetime of the qubit ion. This allows identification of the $|0\rangle$ state of the qubit. Conversely, if the qubit ion is in state $|1\rangle$, it is not excited by the first laser, but the bus ion is, and fluorescence is detected.

6.2 Single-Qubit Gate in Pr:Y_2SiO_5

We first describe arbitrary logic gates performed on a single qubit in Pr^{3+}:Y_2SiO_5 (Rippe et al., 2008). In this work, an ensemble approach is followed. The qubit is defined as a ground-state hyperfine transition of $^{141}Pr^{3+}$ (100% natural abundance, $I = 5/2$). To reduce inhomogeneities in optical frequencies of ions representing the qubit, spectral tailoringof the $^3H_4(0) \rightarrow {}^1D_2(0)$ inhomogeneous linewidth (5 GHz) is used to create narrow (170 kHz) optical transitions between ground and excited hyperfine levels. These transitions are still inhomogeneously broadened as $\Gamma_h \approx 3$ kHz (Equall et al., 1995). Figure 38 shows the absorption to the three excited-state hyperfine levels, from level $|0\rangle$, when $|1\rangle$ is empty, and vice versa. Absorption from the emptied level is negligible as well as background absorption, showing the efficiency of optical pumping in this system, as already mentioned in Section 5.4.

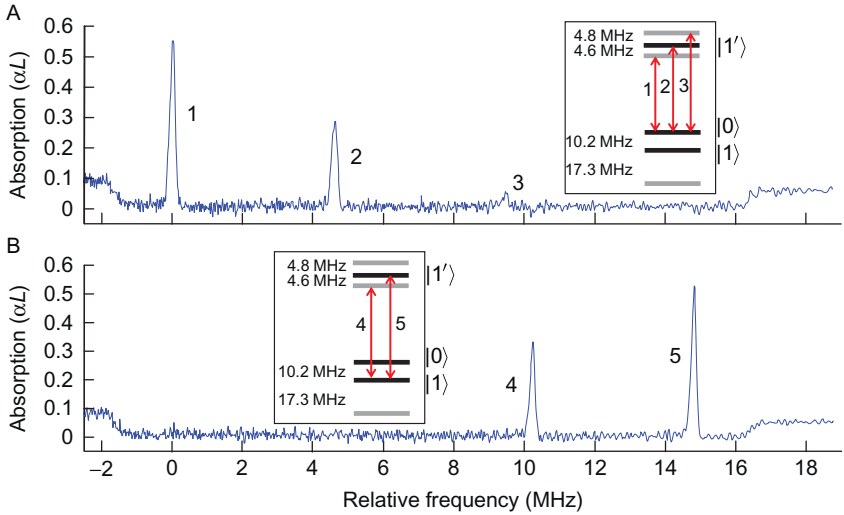

FIGURE 38 Absorption spectra following spectral tailoring of the $^3H_4(0) \rightarrow {}^1D_2(0)$ transition in $Pr^{3+}:Y_2SiO_5$. Narrow lines are created to isolate an ensemble of ions which represent a qubit. The lines correspond to transitions to the three excited-state hyperfine levels from $|0\rangle$ (A) or $|1\rangle$ (B), when $|1\rangle$, resp. $|0\rangle$, is empty. *Reproduced with permission from Rippe et al. (2008), © 2008 the American Physical Society (http:/dx.doi.org/10.1103/PhysRevA.77.022307).*

Arbitrary gates can be applied to the qubit using two-color composite pulses with appropriate relative phases and resonant with the $|0\rangle \leftrightarrow |1'\rangle$ and $|1\rangle \leftrightarrow |1'\rangle$ transitions (labeled 2 and 5 in Fig. 38). These pulses reduce the effect of the hyperfine transition inhomogeneous broadening of ≈ 10 kHz (Roos and Mølmer, 2004). After initializing the qubit in the $|0\rangle$ state, several gates are applied to produce different states on the equatorial plane of the Bloch sphere. The components of the final qubit states on the Bloch sphere are then determined, a process known as quantum-state tomography (Nielsen and Chuang, 2000). This is done by absorption experiments, i.e., population measurements, following further rotations of the final qubit state. The results show that the final qubit states are in excellent agreement with the theoretical ones, showing that single ion arbitrary gates can be performed with high accuracy in a R-doped crystal.

6.3 Two-Qubit Gate in Eu:Y_2SiO_5

The second example demonstrates a two-qubit gate in $Eu^{3+}:Y_2SiO_5$ (Longdell and Sellars, 2004). The qubits are not defined by ground-state hyperfine transitions, but by optical transitions between ground- and excited-state hyperfine levels. In this case too, a ensemble approach is taken and two narrow lines (100 kHz) are created by spectral tailoring in the $^7F_0$–$^5D_0$ inhomogeneous linewidth (2 GHz). This allows selecting ions which can be driven in the same way to represent the control and target qubits. Further selection is then carried

out to retain only the target ions which shift by the same frequency when control ions are excited. The gate is a control-phase gate, for which the phase of the target qubit is modified depending on the state of the control qubit. To demonstrate it, the target qubit is initially set to a point in the equatorial plane of the Bloch sphere by a $\pi/2$ pulse. After a delay τ, a π pulse is shone on the sample to rephase the inhomogeneous dephasing corresponding to the 100-kHz transition width. The emitted echo determines the final state of the qubit. A π pulse is also applied to the control qubit just after the one applied to the target qubit (Fig. 39). When the control qubit is in the excited state, the target one experiences a frequency shift and therefore a phase shift which affects the phase of the final echo. Depending on the initial state of the control qubit, this phase shift occurs either before or after the π pulse applied to the target qubit. This gives a different phase shift to the echo, i.e., the final state of the target qubit (Fig. 39), which is the effect expected from a control-phase gate.

6.4 Other Results

Experiments related to quantum computing focus on Pr^{3+}- and Eu^{3+}-doped crystals since their $I = 5/2$ nuclear spins allow defining a qubit with hyperfine levels as well as storing population in an auxiliary hyperfine level. Spectral tailoring sequences for qubit isolation, as well as selection of interacting ions, have been studied in details in Pr^{3+}- and Eu^{3+}-doped Y_2SiO_5 (Longdell and Sellars, 2004; Nilsson et al., 2004; Rippe et al., 2005). For the ensemble approach, the stoichiometric crystal $EuCl_3 \cdot 6H_2O$, codoped with various R ions, has been investigated with respect to inhomogeneous and homogeneous linewidths and electric interactions between ions in satellite lines

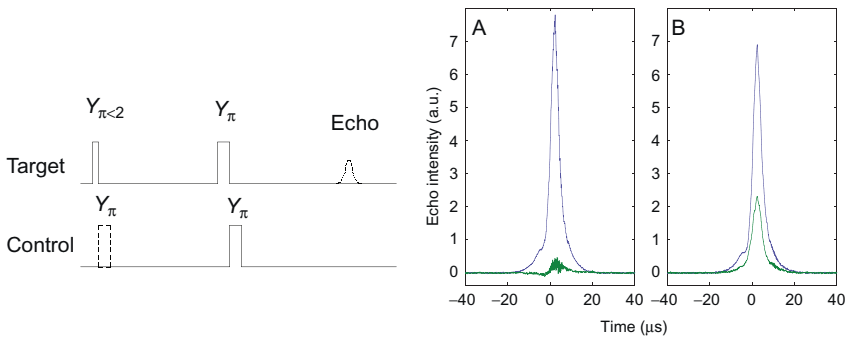

FIGURE 39 A two-qubit control-phase gate. Left: sequence of pulses on the control and target qubits to demonstrate a control-phase gate. The dashed line indicates the π pulse used to set the control qubit to state $|1\rangle$. Right: in-phase and quadrature signals of the echo observed on the target qubit measured by heterodyne detection. Control qubit in the $|0\rangle$ (A) and $|1\rangle$ (B) states. *Reproduced with permission from Longdell et al. (2004), © 2004 the American Physical Society (http:/dx.doi.org/10.1103/PhysRevLett.93.130503).*

(Ahlefeldt et al., 2013a,b,c). Ce^{3+}, Pr^{3+} and Ce^{3+}, Eu^{3+} interactions have also been characterized in Y_2SiO_5 for a single-instance approach where Ce^{3+} is the bus ion (Serrano et al., 2014; Yan et al., 2013). Although these results suggest that quantum computing could be experimentally demonstrated for a few qubits using both approaches, several important points, like high-fidelity two-qubit gates or more than two interacting qubits, have not been shown yet. However, recent results have reported detection of single R ions in Er^{3+}:Y_2SiO_5 (Yin et al., 2013), Pr^{3+}:$Y_3Al_5O_{12}$ (Kolesov et al., 2012), and Pr^{3+}:Y_2SiO_5 (Utikal et al., 2014). Moreover, in $Y_3Al_5O_{12}$, a single Ce^{3+} electronic spin coherence has been optically detected and manipulated (Kolesov et al., 2013; Siyushev et al., 2014). This suggests that the qubit readout operation in the single-instance approach is possible. Stronger coupling between light and a single R ion could also be achieved in high Q cavities (McAuslan et al., 2009, 2011a).

7 CONCLUSION AND OUTLOOK

R-doped crystals fulfill many of the requirements for an efficient QIP system. Protocols exist that take advantage of their specific spectroscopic properties, which can be moreover enhanced and tailored by a number of techniques. In particular, R-doped crystals can provide interfaces between photonic quantum bits, in the optical and microwave ranges, and solid-state qubits. As these qubits can be further processed by optical control, a complete quantum network node could be obtained. However, a QIP system outperforming a classical system in current information processing tasks is extremely demanding. Still, R-based quantum memories seem much closer to reach the required operating parameters than quantum computers, which are clearly much more complex devices. Strong theoretical and experimental improvements are needed, including development of new materials. Here, bulk single crystals are the preferred choice because of their outstanding spectroscopic properties, although some parameters have still to be improved. Attractive alternatives, like nanostructured materials, may provide additional and important features. In particular, this could allow coupling R ions to other atomic quantum systems, nanoscale quantum mechanical oscillators, or nanocavities. In such hybrid quantum systems, one could expect to combine efficient processing and storage functionalities, and interface quantum states of different physical nature. This approach may not only benefit QIP but also open the way to fundamental studies in quantum physics.

ACKNOWLEDGMENTS

The authors thank T. Chanelière and R. Ahlefeldt for stimulating discussions and careful reading of the manuscript. This work is supported by the European Union's Seventh Framework Program FP7/2007-2013/ under REA grant agreement No. 287252 (CIPRIS, People Program-Marie Curie Actions) and ANR project RAMACO (No. 12-BS08-0015-01).

ACRONYMS AND ABBREVIATIONS

AFC	atomic frequency comb
$\mathbf{A}_J$	hyperfine coupling constant
CF	crystal field
CNOT	control not gate
CRIB	controlled reversible inhomogeneous broadening
DD	dynamical decoupling
EIT	electromagnetically induced transparency
EPR	electron paramagnetic resonance
f	oscillator strength
FID	free-induction decay
GEM	gradient echo memory
g_J	Landé's factor
HYPER	hybrid photon-echo rephasing
I	nuclear spin quantum number
J	total angular momentum quantum number
L	orbital angular momentum quantum number
NMR	nuclear magnetic resonance
P	quadrupolar coupling constant
QIP	quantum information processing
QML	quantum memories for light
rf	radiofrequency
RHS	Raman heterodyne scattering
ROSE	revival of silenced echo
S	electron spin quantum number
sech	hyperbolic secant function
SHB	spectral hole burning
T_1	population lifetime
T_2	coherence lifetime
T_{2hf}	hyperfine coherence lifetime
T_M	phase memory time
TLS	two-level system
ZEFOZ	zero first-order Zeeman shift
α	absorption coefficient
η	asymmetry coupling constant
γ_n	nuclear gyromagnetic factor
Γ_{eff}	effective homogeneous linewidth
Γ_h	homogeneous linewidth
Γ_{inh}	inhomogeneous linewidth
μ_B	Bohr magneton
Ω	Rabi frequency (rad s^{-1})

REFERENCES

Abella, I.D., Kurnit, N.A., Hartmann, S.R., 1966. Photon echoes. Phys. Rev. 141 (1), 391.

Afzelius, M., Simon, C., 2010. Impedance-matched cavity quantum memory. Phys. Rev. A 82 (2), 022310.

Afzelius, M., Simon, C., de Riedmatten, H., Gisin, N., 2009. Multimode quantum memory based on atomic frequency combs. Phys. Rev. A 79 (5), 052329.

Afzelius, M., Staudt, M.U., de Riedmatten, H., Gisin, N., Guillot-Noël, O., Goldner, P., Marino, R., Porcher, P., Cavalli, E., Bettinelli, M., 2010a. Efficient optical pumping of Zeeman spin levels in Nd^{3+}: YVO_4. J. Lumin. 130 (9), 1566–1571.

Afzelius, M., Usmani, I., Amari, A., Lauritzen, B., Walther, A., Simon, C., Sangouard, N., Minář, J., de Riedmatten, H., Gisin, N., Kröll, S., 2010b. Demonstration of atomic frequency comb memory for light with spin-wave storage. Phys. Rev. Lett. 104 (4), 040503.

Afzelius, M., Sangouard, N., Johansson, G., Staudt, M.U., Wilson, C.M., 2013. Proposal for a coherent quantum memory for propagating microwave photons. New J. Phys. 15 (6), 065008.

Agladze, N., Popova, M.N., Zhizhin, G., Egorov, V., Petrova, M., 1991. Isotope structure in optical spectra of $LiYF_4$:Ho^{3+}. Phys. Rev. Lett. 66 (4), 477–480.

Ahlefeldt, R., Smith, A., Sellars, M.J., 2009. Ligand isotope structure of the optical $^7F_0$–$^5D_0$ transition in $EuCl_3 6H_2O$. Phys. Rev. B 80 (20), 205106.

Ahlefeldt, R., McAuslan, D.L., Longdell, J.J., Manson, N.B., Sellars, M.J., 2013a. Precision measurement of electronic ion-ion interactions between neighboring Eu^{3+} optical centers. Phys. Rev. Lett. 111 (24), 240501.

Ahlefeldt, R.L., Hutchison, W.D., Manson, N.B., Sellars, M.J., 2013b. Method for assigning satellite lines to crystallographic sites in rare-earth crystals. Phys. Rev. B 88 (18), 184424.

Ahlefeldt, R.L., Manson, N.B., Sellars, M.J., 2013c. Optical lifetime and linewidth studies of the $^7F_0$–$^5D_0$ transition in $EuCl_3$ $6H_2O$: a potential material for quantum memory applications. J. Lumin. 133, 152–156.

Ahlefeldt, R.L., Zhong, M., Bartholomew, J.G., Sellars, M.J., 2013d. Minimizing Zeeman sensitivity on optical and hyperfine transitions in $EuCl_3$ $6H_2O$ to extend coherence times. J. Lumin. 143, 193–200.

Alexander, A.L., Longdell, J.J., Sellars, M.J., Manson, N.B., 2006. Photon echoes produced by switching electric fields. Phys. Rev. Lett. 96 (4), 043602.

Alexander, A.L., Longdell, J.J., Sellars, M.J., 2007. Measurement of the ground-state hyperfine coherence time of $^{151}Eu^{3+}$:Y_2SiO_5. J. Opt. Soc. Am. B 24 (9), 2479–2482.

Alexander, A., Lauro, R., Louchet, A., Chanelière, T., Le Gouët, J.-L., 2008. Stimulated Raman adiabatic passage in Tm^{3+}:YAG. Phys. Rev. B 78 (14), 144407.

Allen, L., Eberly, J.H., 1987. Optical Resonance and Two-Level Atoms. Dover, New-York.

Arcangeli, A., Lovrić, M., Tumino, B., Ferrier, A., Goldner, P., 2014. Spectroscopy and coherence lifetime extension of hyperfine transitions in $^{151}Eu^{3+}$:Y_2SiO_5. Phys. Rev. B 89 (18), 184305.

Beaudoux, F., Ferrier, A., Guillot-Noël, O., Chanelière, T., Le Gouët, J.-L., Goldner, P., 2011. Emission of photon echoes in a strongly scattering medium. Opt. Express 19 (16), 15236–15243.

Beaudoux, F., Guillot-Noël, O., Lejay, J., Ferrier, A., Goldner, P., 2012. Concentration dependence of absorption and optical and hyperfine transition dynamics in Pr^{3+}:$La_2(WO_4)_3$. J. Phys. B At. Mol. Opt. Phys. 45 (12), 124014.

Beavan, S.E., Hedges, M.P., Sellars, M.J., 2012. Demonstration of photon-echo rephasing of spontaneous emission. Phys. Rev. Lett. 109 (9), 093603.

Bennett, C.H., Brassard, G., 1984. Quantum cryptography: public key distribution and coin tossing. In: Int. Conf. Comput. Syst. Signal Process. Bangalore, India, pp. 175–179.

Bennett, C.H., Brassard, G., Crépeau, C., Jozsa, R., Peres, A., Wootters, W.K., 1993. Teleporting an unknown quantum state via dual classical and Einstein-Podolsky-Rosen channels. Phys. Rev. Lett. 70 (13), 1895–1899.

Blatt, R., Roos, C.F., 2012. Quantum simulations with trapped ions. Nat. Phys. 8 (4), 277–284.

Bloch, F., 1946. Nuclear induction. Phys. Rev. 70 (7–8), 460–474.

Bloch, I., Dalibard, J., Nascimbène, S., 2012. Quantum simulations with ultracold quantum gases. Nat. Phys. 8 (4), 267–276.

Boixo, S., Rønnow, T.F., Isakov, S.V., Wang, Z., Wecker, D., Lidar, D.A., Martinis, J.M., Troyer, M., 2014. Evidence for quantum annealing with more than one hundred qubits. Nat. Phys. 10 (3), 218–224.

Bonarota, M., Ruggiero, J., Le Gouët, J.-L., Chanelière, T., 2010. Efficiency optimization for atomic frequency comb storage. Phys. Rev. A 81 (3), 033803.

Bonarota, M., Le Gouët, J.-L., Chanelière, T., 2011. Highly multimode storage in a crystal. New J. Phys. 13 (1), 013013.

Böttger, T., Thiel, C.W., Sun, Y., Cone, R., 2006. Optical decoherence and spectral diffusion at 1.5μm in Er^{3+}:Y_2SiO_5 versus magnetic field, temperature, and Er^{3+} concentration. Phys. Rev. B 73 (7), 075101.

Böttger, T., Thiel, C.W., Cone, R., Sun, Y., 2008. Controlled compositional disorder in Er^{3+}:Y_2SiO_5 provides a wide-bandwidth spectral hole burning material at 1.5μm. Phys. Rev. B 77 (15), 155125.

Böttger, T., Thiel, C.W., Cone, R., Sun, Y., 2009. Effects of magnetic field orientation on optical decoherence in Er^{3+}:Y_2SiO_5. Phys. Rev. B 79 (11), 115104.

Bouwmeester, D., Pan, J.-W., Mattle, K., Eibl, M., Weinfurter, H., Zeilinger, A., 1997. Experimental quantum teleportation. Nature 390 (6660), 575–579.

Briegel, H.J., Dür, W., Cirac, J.I., Zoller, P., 1998. Quantum repeaters: the role of imperfect local operations in quantum communication. Phys. Rev. Lett. 81 (26), 5932–5935.

Bussières, F., Sangouard, N., Afzelius, M., de Riedmatten, H., Simon, C., Tittel, W., 2013. Prospective applications of optical quantum memories. J. Mod. Opt. 60 (18), 1519–1537.

Bussières, F., Clausen, C., Tiranov, A., Korzh, B., Verma, V.B., Nam, S.W., Marsili, F., Ferrier, A., Goldner, P., Herrmann, H., Silberhorn, C., Sohler, W., Afzelius, M., Gisin, N., 2014. Quantum teleportation from a telecom-wavelength photon to a solid-state quantum memory. Nat. Photonics 8, 775–778.

Carr, H., Purcell, E., 1954. Effects of diffusion on free precession in nuclear magnetic resonance experiments. Phys. Rev. 94 (3), 630–638.

Chanelière, T., Matsukevich, D.N., Jenkins, S.D., Lan, S.Y., Kennedy, T.A.B., Kuzmich, A., 2005. Storage and retrieval of single photons transmitted between remote quantum memories. Nature 438 (7069), 833–836.

Chanelière, T., Ruggiero, J., Bonarota, M., Afzelius, M., Le Gouët, J.-L., 2010. Efficient light storage in a crystal using an atomic frequency comb. New J. Phys. 12 (2), 023025.

Chuang, I.L., Vandersypen, L.M.K., Zhou, X., Leung, D.W., Lloyd, S., 1998. Experimental realization of a quantum algorithm. Nature 393 (6681), 143–146.

Chukalina, E.P., Popova, M.N., Antic-Fidancev, E., Chaminade, J.P., 1999. Hyperfine structure in optical spectra of $CsCdBr_3$: Pr^{3+}. Phys. Lett. A 258 (4–6), 375–378.

Cirac, J.I., Zoller, P., 2012. Goals and opportunities in quantum simulation. Nat. Phys. 8 (4), 264–266.

Clarke, J., Wilhelm, F.K., 2008. Superconducting quantum bits. Nature 453 (7198), 1031–1042.

Clausen, C., Usmani, I., Bussières, F., Sangouard, N., Afzelius, M., de Riedmatten, H., Gisin, N., 2011. Quantum storage of photonic entanglement in a crystal. Nature 469 (7331), 508–511.

Clausen, C., Bussières, F., Afzelius, M., Gisin, N., 2012. Quantum storage of heralded polarization qubits in birefringent and anisotropically absorbing materials. Phys. Rev. Lett. 108 (19), 190503.

Dajczgewand, J., Le Gouët, J.-L., Louchet-Chauvet, A., Chanelière, T., 2014. Large efficiency at telecom wavelength for optical quantum memories. Opt. Lett. 39 (9), 2711–2714.

Damon, V., Bonarota, M., Louchet-Chauvet, A., Chanelière, T., Le Gouët, J.-L., 2011. Revival of silenced echo and quantum memory for light. New J. Phys. 13 (9), 093031.

de Riedmatten, H., Afzelius, M., Staudt, M.U., Simon, C., Gisin, N., 2008. A solid-state light–matter interface at the single-photon level. Nature 456 (7223), 773–777.

de Seze, F., Louchet, A., Crozatier, V., Lorgeré, I., Bretenaker, F., Le Gouët, J.-L., Guillot-Noël, O., Goldner, P., 2006. Experimental tailoring of a three-level $\wedge$ system in Tm^{3+}:YAG. Phys. Rev. B 73 (8), 085112.

Deutsch, D., 1985. Quantum theory, the Church-Turing principle and the universal quantum computer. Proc. R. Soc. A 400 (1818), 97–117.

DeVoe, R., Wokaun, A., Rand, S., Brewer, R., 1981. Monte Carlo theory of optical dephasing in LaF_3:Pr^{3+}. Phys. Rev. B 23 (7), 3125–3138.

DiVincenzo, D.P., 2000. The physical implementation of quantum computation. Fortschr. Phys. 48 (9–11), 771–783.

Duan, L.M., Lukin, M.D., Cirac, J.I., Zoller, P., 2001. Long-distance quantum communication with atomic ensembles and linear optics. Nature 414 (6862), 413–418.

Ekert, A.K., 1991. Quantum cryptography based on Bell's theorem. Phys. Rev. Lett. 67 (6), 661–663.

Equall, R.W., Cone, R.L., Macfarlane, R.M., 1995. Homogeneous broadening and hyperfine structure of optical transitions in Pr^{3+}:Y_2SiO_5. Phys. Rev. B 52 (6), 3963.

Erickson, L.E., 1977. Optical measurement of the hyperfine splitting of the $^1D_2$ metastable state of Pr^{3+} in LaF_3 by enhanced and saturated absorption spectroscopy. Phys. Rev. B 16 (11), 4731–4736.

Erickson, L.E., 1985. NMR measurement of an ion in an excited state by indirect optical detection: a $^1G_4$ level of $LiYF_4$: Pr^{3+}. Phys. Rev. B 32 (1), 1.

Erickson, L., 1986. Lattice and electronic contributions to the quadrupole interaction of trivalent europium. Phys. Rev. B 34 (1), 36–40.

Fekete, J., Rieländer, D., Cristiani, M., de Riedmatten, H., 2013. Ultranarrow-band photon-pair source compatible with solid state quantum memories and telecommunication networks. Phys. Rev. Lett. 110 (22), 220502.

Ferrier, A., Thiel, C.W., Tumino, B., Ramírez, M.O., Bausá, L.E., Cone, R.L., Ikesue, A., Goldner, P., 2013. Narrow inhomogeneous and homogeneous optical linewidths in a rare earth doped transparent ceramic. Phys. Rev. B 87 (4), 041102.

Fleischhauer, M., Imamoglu, A., Marangos, J.P., 2005. Electromagnetically induced transparency: optics in coherent media. Rev. Mod. Phys. 77 (2), 633–673.

Flinn, G.P., Jang, K.W., Ganem, J., Jones, M.L., Meltzer, R.S., Macfarlane, R.M., 1994. Sample-dependent optical dephasing in bulk crystalline samples of Y_2O_3: Eu^{3+}. Phys. Rev. B 49 (9), 5821.

Fraval, E., Sellars, M.J., Longdell, J.J., 2004. Method of extending hyperfine coherence times in Pr^{3+}:Y_2SiO_5. Phys. Rev. Lett. 92 (7), 077601.

Fraval, E., Sellars, M.J., Longdell, J.J., 2005. Dynamic decoherence control of a solid-state nuclear-quadrupole qubit. Phys. Rev. Lett. 95 (3), 030506.

Ganem, J., Wang, Y.P., Boye, D., Meltzer, R.S., Yen, W.M., Macfarlane, R.M., 1991. Nonexponential photon-echo decays of paramagnetic ions in the superhyperfine limit. Phys. Rev. Lett. 66 (6), 695–698.

Genov, G.T., Schraft, D., Halfmann, T., Vitanov, N.V., 2014. Correction of arbitrary field errors in population inversion of quantum systems by universal composite pulses. Phys. Rev. Lett. 113 (4), 043001.

Gisin, N., Thew, R., 2007. Quantum communication. Nat. Photonics 1 (3), 165–171.

Gisin, N., Ribordy, G., Tittel, W., Zbinden, H., 2002. Quantum cryptography. Rev. Mod. Phys. 74 (1), 145–195.

Goldner, P., Guillot-Noël, O., 2004. Magnetic interactions in Pr^{3+}:$LiYF_4$ for quantum manipulation: search for an efficient three-level Λ system. Mol. Phys. 102 (11–12), 1185–1192.

Goldner, P., Guillot-Noël, O., Beaudoux, F., Le Du, Y., Lejay, J., Chanelière, T., Rippe, L., Amari, A., Walther, A., Kröll, S., 2009. Long coherence lifetime and electromagnetically induced transparency in a highly-spin-concentrated solid. Phys. Rev. A 79 (3), 033809.

Goldschmidt, E.A., Beavan, S.E., Polyakov, S.V., Migdall, A.L., Sellars, M.J., 2013. Storage and retrieval of collective excitations on a long-lived spin transition in a rare-earth ion-doped crystal. Opt. Express 21 (8), 10087.

Görller-Walrand, C., Binnemans, K., 1996. Rationalization of crystal-field parametrization. In: Geschneider, K.A., Eyring, L. (Eds.), Handbook on the Physics and Chemistry of Rare Earths. Elsevier, Amsterdam, pp. 121–283.

Grover, L.K., Dec. 1997. Quantum computers can search arbitrarily large databases by a single query. Phys. Rev. Lett. 79 (23), 4709–4712.

Grynberg, G., Aspect, A., Fabre, C., 2010. Introduction to quantum optics. Cambridge University Press, Cambridge, UK.

Guillot-Noël, O., Goldner, P., Antic-Fidancev, E., Le Gouët, J.-L., 2005. Analysis of magnetic interactions in rare-earth-doped crystals for quantum manipulation. Phys. Rev. B 71 (17), 174409.

Guillot-Noël, O., Goldner, P., Du, Y., Baldit, E., Monnier, P., Bencheikh, K., 2006. Hyperfine interaction of Er^{3+} ions in Y_2SiO_5: an electron paramagnetic resonance spectroscopy study. Phys. Rev. B 74 (21), 214409.

Guillot-Noël, O., Goldner, P., Du, Y., Loiseau, P., Julsgaard, B., Rippe, L., Kröll, S., 2007. Hyperfine structure, optical dephasing, and spectral-hole lifetime of single-crystalline Pr^{3+}:$La_2(WO_4)_3$. Phys. Rev. B 75 (20), 205110.

Guillot-Noël, O., Goldner, P., Beaudoux, F., Le Du, Y., Lejay, J., Amari, A., Walther, A., Rippe, L., Kröll, S., 2009. Hyperfine structure and hyperfine coherent properties of praseodymium in single-crystalline $La_2(WO_4)_3$ by hole-burning and photon-echo techniques. Phys. Rev. B 79 (15), 155119.

Guillot-Noël, O., Le Du, Y., Beaudoux, F., Antic-Fidancev, E., Reid, M.F., Marino, R.A., Lejay, J., Goldner, P., 2010. Calculation and analysis of hyperfine and quadrupole interactions in praseodymium-doped $La_2(WO_4)_3$. J. Lumin. 130 (9), 1557–1565.

Gündoğan, M., Ledingham, P.M., Almasi, A., Cristiani, M., de Riedmatten, H., 2012. Quantum storage of a photonic polarization qubit in a solid. Phys. Rev. Lett. 108 (19), 190504.

Hahn, E., 1950. Spin echoes. Phys. Rev. 80 (4), 580–594.

Ham, B.S., Hemmer, P.R., Shahriar, M.S., 1997. Efficient electromagnetically induced transparency in a rare-earth doped crystal. Opt. Commun. 144 (4–6), 227–230.

Hansen, P.C., Leask, M.J.M., Wanklyn, B.M., Sun, Y., Cone, R.L., Abraham, M.M., 1997. Spectral hole burning and optically detected nuclear quadrupole resonance in flux-grown stoichiometric europium vanadate crystals. Phys. Rev. B 56 (13), 7918–7929.

Hanson, R., Petta, J.R., Tarucha, S., Vandersypen, L.M.K., 2007. Spins in few-electron quantum dots. Rev. Mod. Phys. 79 (4), 1217–1265.

Hedges, M.P., Longdell, J.J., Li, Y., Sellars, M.J., 2010. Efficient quantum memory for light. Nature 465 (7301), 1052–1056.

Heinze, G., Hubrich, C., Halfmann, T., 2013. Stopped light and image storage by electromagnetically induced transparency up to the regime of one minute. Phys. Rev. Lett. 111 (3), 033601.

Henderson, B., Imbush, G.F., 1989. Optical Spectroscopy of Inorganic Solids. Oxford University Press, New-York, USA.

Hétet, G., Longdell, J.J., Alexander, A., Lam, P., Sellars, M.J., 2008. Electro-optic quantum memory for light using two-level atoms. Phys. Rev. Lett. 100 (2), 023601.

Hu, P., Hartmann, S.R., 1974. Theory of spectral diffusion decay using an uncorrelated-sudden-jump model. Phys. Rev. B 9 (1), 1.

Hu, P., Walker, L., 1978. Spectral-diffusion decay in echo experiments. Phys. Rev. B 18 (3), 1300–1305.

Hu, P., Geschwind, S., Jedju, T., 1976. Spin-flip Raman echo in n-type CdS. Phys. Rev. Lett. 37 (20), 1357–1360.

Hufner, S., 1978. Optical Spectra of Transparent Rare-Earth Compounds. Academic Press, New York, USA.

Jacquier, B., Liu, G. (Eds.), 2005. Spectroscopic Properties of Rare Earths in Optical Materials. Springer, Berlin, Germany.

Jin, J., Slater, J.A., Saglamyurek, E., Sinclair, N., George, M., Ricken, R., Oblak, D., Sohler, W., Tittel, W., 2013. Two-photon interference of weak coherent laser pulses recalled from separate solid-state quantum memories. Nat. Commun. 4, 2386.

Johnson, M.W., Amin, M.H.S., Gildert, S., Lanting, T., Hamze, F., Dickson, N., Harris, R., Berkley, A.J., Johansson, J., Bunyk, P., Chapple, E.M., Enderud, C., Hilton, J.P., Karimi, K., Ladizinsky, E., Ladizinsky, N., Oh, T., Perminov, I., Rich, C., Thom, M.C., Tolkacheva, E., Truncik, C.J.S., Uchaikin, S., Wang, J., Wilson, B., Rose, G., 2011. Quantum annealing with manufactured spins. Nature 473 (7346), 194–198.

Kimble, H.J., 2008. The quantum internet. Nature 453 (7198), 1023–1030.

Klieber, R., Michalowski, A., Neuhaus, R., Suter, D., 2003. Nuclear quadrupole resonance of an electronically excited state from high-resolution hole-burning spectroscopy. Phys. Rev. B 67 (18), 184103.

Kok, P., Nemoto, K., Ralph, T.C., Dowling, J.P., Milburn, G.J., 2007. Linear optical quantum computing with photonic qubits. Rev. Mod. Phys. 79 (1), 135–174.

Kolesov, R., Xia, K., Reuter, R., Stöhr, R., Zappe, A., Meijer, J., Hemmer, P.R., Wrachtrup, J., 2012. Optical detection of a single rare-earth ion in a crystal. Nat. Commun. 3, 1029.

Kolesov, R., Xia, K., Reuter, R., Jamali, M., Stöhr, R., Inal, T., Siyushev, P., Wrachtrup, J., 2013. Mapping spin coherence of a single rare-earth ion in a crystal onto a single photon polarization state. Phys. Rev. Lett. 111 (12), 120502.

Könz, F., Sun, Y., Thiel, C.W., Cone, R., Equall, R., Hutcheson, R., Macfarlane, R.M., 2003. Temperature and concentration dependence of optical dephasing, spectral-hole lifetime, and anisotropic absorption in Eu^{3+}:Y_2SiO_5. Phys. Rev. B 68 (8), 085109.

Kuznetsova, E., Kocharovskaya, O., Hemmer, P., Scully, M., 2002. Atomic interference phenomena in solids with a long-lived spin coherence. Phys. Rev. A 66 (6), 063802.

Ladd, T.D., Jelezko, F., Laflamme, R., Nakamura, Y., Monroe, C., O'Brien, J.L., 2010. Quantum computers. Nature 464 (7285), 45–53.

Lauritzen, B., Hastings-Simon, S.R., de Riedmatten, H., Afzelius, M., Gisin, N., 2008. State preparation by optical pumping in erbium-doped solids using stimulated emission and spin mixing. Phys. Rev. A 78 (4), 043402.

Lauritzen, B., Minář, J., de Riedmatten, H., Afzelius, M., Sangouard, N., Simon, C., Gisin, N., 2010. Telecommunication-wavelength solid-state memory at the single photon level. Phys. Rev. Lett. 104 (8), 80502.

Lauritzen, B., Timoney, N., Gisin, N., Afzelius, M., de Riedmatten, H., Sun, Y., Macfarlane, R.M., Cone, R., 2012. Spectroscopic investigations of Eu^{3+}:Y_2SiO_5 for quantum memory applications. Phys. Rev. B 85 (11), 115111.

Lauro, R., Chanelière, T., Le Gouët, J.-L., 2009. Spectral hole burning for stopping light. Phys. Rev. A 79 (5), 053801.

Lauro, R., Chanelière, T., Le Gouët, J.-L., 2011. Adiabatic refocusing of nuclear spins in Tm^{3+}:YAG. Phys. Rev. B 83 (3), 035124.

Ledingham, P.M., Naylor, W.R., Longdell, J.J., 2012. Experimental realization of light with time-separated correlations by rephasing amplified spontaneous emission. Phys. Rev. Lett. 109 (9), 093602.

Le Gouët, J.-L., Bretenaker, F., Lorgeré, I., 2006. Atomic processing of optically carried RF signals. In: Berman, P.R., Lin, C.C., Arimondo, E. (Eds.), Advances in Atomic, Molecular and Optical Physics. Elsevier, Amsterdam, pp. 549–613.

Li, Y., Zhang, H., Kim, C., Wagner, K.H., Hemmer, P., Wang, L.V., 2008. Pulsed ultrasound-modulated optical tomography using spectral-hole burning as a narrowband spectral filter. Appl. Phys. Lett. 93 (1), 011111.

Liu, G., 2005. Electronic energy level structure. In: Liu, G., Jacquier, B. (Eds.), Spectroscopic Properties of Rare Earths in Optical Materials. Springer, Berlin.

Liu, C., Dutton, Z., Behroozi, C.H., Hau, L.V., 2001. Observation of coherent optical information storage in an atomic medium using halted light pulses. Nature 409 (6819), 490–493.

Longdell, J.J., Sellars, M.J., 2004. Experimental demonstration of quantum-state tomography and qubit-qubit interactions for rare-earth-metal-ion-based solid-state qubits. Phys. Rev. A 69 (3), 032307.

Longdell, J.J., Sellars, M.J., Manson, N.B., 2002. Hyperfine interaction in ground and excited states of praseodymium-doped yttrium orthosilicate. Phys. Rev. B 66 (3), 035101.

Longdell, J.J., Sellars, M.J., Manson, N.B., 2004. Demonstration of conditional quantum phase shift between ions in a solid. Phys. Rev. Lett. 93 (13), 130503.

Longdell, J.J., Fraval, E., Sellars, M.J., Manson, N.B., 2005. Stopped light with storage times greater than one second using electromagnetically induced transparency in a solid. Phys. Rev. Lett. 95 (6), 063601.

Longdell, J.J., Alexander, A., Sellars, M.J., Nov. 2006. Characterization of the hyperfine interaction in europium-doped yttrium orthosilicate and europium chloride hexahydrate. Phys. Rev. B 74 (19), 195101.

Louchet, A., Habib, J.S., Crozatier, V., Lorgeré, I., Goldfarb, F., Bretenaker, F., Le Gouët, J.-L., Guillot-Noël, O., Goldner, P., 2007. Branching ratio measurement of a Λ system in Tm^{3+}:YAG under a magnetic field. Phys. Rev. B 75 (3), 035131.

Louchet, A., Le Du, Y., Bretenaker, F., Chanelière, T., Goldfarb, F., Lorgeré, I., Le Gouët, J.-L., Guillot-Noël, O., Goldner, P., 2008. Optical excitation of nuclear spin coherence in a Tm^{3+}:YAG crystal. Phys. Rev. B 77 (19), 195110.

Lovrić, M., Glasenapp, P., Suter, D., Tumino, B., Ferrier, A., Goldner, P., Sabooni, M., Rippe, L., Kröll, S., 2011. Hyperfine characterization and spin coherence lifetime extension in Pr^{3+}:$La_2(WO_4)_3$. Phys. Rev. B 84 (10), 104417.

Lovrić, M., Glasenapp, P., Suter, D., 2012. Spin Hamiltonian characterization and refinement for Pr^{3+}:$YAlO_3$ and Pr^{3+}:Y_2SiO_5. Phys. Rev. B 85 (1), 014429.

Lovrić, M., Suter, D., Ferrier, A., Goldner, P., 2013. Faithful solid state optical memory with dynamically decoupled spin wave storage. Phys. Rev. Lett. 111, 020503.

Lukin, M.D., 2003. Colloquium: trapping and manipulating photon states in atomic ensembles. Rev. Mod. Phys. 75 (2), 457–472.

Lvovsky, A.I., Sanders, B.C., Tittel, W., 2009. Optical quantum memory. Nat. Photonics 3 (12), 706–714.

Ma, X.-S., Herbst, T., Scheidl, T., Wang, D., Kropatschek, S., Naylor, W., Wittmann, B., Mech, A., Kofler, J., Anisimova, E., Makarov, V., Jennewein, T., Ursin, R., Zeilinger, A., 2012. Quantum teleportation over 143 kilometres using active feed-forward. Nature 489 (7415), 269–273.

Macfarlane, R.M., 1990. Inhomogeneous broadening of spectral lines in doped insulators. J. Lumin. 45 (1–6), 1–5.

Macfarlane, R.M., 1993. Photon-echo measurements on the trivalent thulium ion. Opt. Lett. 18 (22), 1958–1960.

Macfarlane, R.M., 2002. High-resolution laser spectroscopy of rare-earth doped insulators: a personal perspective. J. Lumin. 100 (1), 1–20.

Macfarlane, R.M., 2007. Optical Stark spectroscopy of solids. J. Lumin. 125 (1–2), 156–174.

Macfarlane, R.M., Shelby, R.M., 1987a. Coherent transient and holeburning spectroscopy of rare earth ions in solids. In: Kaplyanskii, A.A., Macfarlane, R.M. (Eds.), Spectroscopy of Solids Containing Rare Earth Ions. North Holland, Amsterdam, pp. 51–184.

Macfarlane, R.M., Shelby, R.M., 1987b. Homogeneous line broadening of optical transitions of ions and molecules in glasses. J. Lumin. 36 (4), 179–207.

Macfarlane, R.M., Shelby, R.M., Burum, D.P., 1981. Optical hole burning by superhyperfine interactions in CaF_2:Pr^{3+}. Opt. Lett. 6 (12), 593–594.

Macfarlane, R.M., Wannemacher, R., Boye, D., Wang, Y.P., Meltzer, R.S., 1991. Nonexponential photon echo decay of Er^{3+} in fluorides. J. Lumin. 48, 313–317.

Macfarlane, R.M., Cassanho, A., Meltzer, R.S., 1992. Inhomogeneous broadening by nuclear spin fields: a new limit for optical transitions in solids. Phys. Rev. Lett. 69 (3), 542–545.

Macfarlane, R.M., Meltzer, R.S., Malkin, B.Z., 1998. Optical measurement of the isotope shifts and hyperfine and superhyperfine interactions of Nd in the solid state. Phys. Rev. B 58 (9), 5692–5700.

Macfarlane, R.M., Könz, F., Sun, Y., Cone, R.L., 2000. Spectral hole burning and optical dephasing in disordered crystals–Pr^{3+}:$LiNbO_3$ and Pr^{3+}:$Sr_{.6}Ba_{.4}Nb_2O_6$(SBN). J. Lumin 86 (3), 311–315.

Marcikic, I., de Riedmatten, H., Tittel, W., Zbinden, H., Gisin, N., 2003. Long-distance teleportation of qubits at telecommunication wavelengths. Nature 421 (6922), 509–513.

Marsili, F., Verma, V.B., Stern, J.A., Harrington, S., Lita, A.E., Gerrits, T., Vayshenker, I., Baek, B., Shaw, M.D., Mirin, R.P., Nam, S.W., 2013. Detecting single infrared photons with 93% system efficiency. Nat. Photonics 7 (3), 210–214.

McAuslan, D.L., Longdell, J.J., Sellars, M.J., 2009. Strong-coupling cavity QED using rare-earth-metal-ion dopants in monolithic resonators: what you can do with a weak oscillator. Phys. Rev. A 80 (6), 062307.

McAuslan, D.L., Korystov, D., Longdell, J.J., 2011a. Coherent spectroscopy of rare-earth-metal-ion-doped whispering-gallery-mode resonators. Phys. Rev. A 83 (6), 063847.

McAuslan, D.L., Ledingham, P.M., Naylor, W.R., Beavan, S.E., Hedges, M.P., Sellars, M.J., Longdell, J.J., 2011b. Photon-echo quantum memories in inhomogeneously broadened two-level atoms. Phys. Rev. A 84 (2), 022309.

McAuslan, D.L., Bartholomew, J., Sellars, M.J., Longdell, J.J., 2012. Reducing decoherence in optical and spin transitions in rare-earth-metal-ion–doped materials. Phys. Rev. A 85 (3), 032339.

McLeod, D.P., Reid, M.F., 1997. Intensities of hyperfine transitions of Pr^{3+} and Ho^{3+} in CaF_2. J. Alloys Compd. 250 (1–2), 302–305.

Meiboom, S., Gill, D., 1958. Modified spin-echo method for measuring nuclear relaxation times. Rev. Sci. Instrum. 29 (8), 688.

Meltzer, R.S., 2005. Line broadening mechanisms and their measurement. In: Jacquier, B., Liu, G. (Eds.), Spectroscopic Properties of Rare Earths in Optical Materials. Springer, Berlin, pp. 191–265.

Mieth, S., Schraft, D., Halfmann, T., Yatsenko, L.P., 2012. Rephasing of optically driven atomic coherences by rapid adiabatic passage in Pr^{3+}:Y_2SiO_5. Phys. Rev. A 86 (6), 063404.

Mims, W.B., 1968. Phase memory in electron spin echoes, lattice relaxation effects in $CaWO_4$: Er, Ce, Mn. Phys. Rev. 168 (2), 370.

Mitsunaga, M., Kintzer, E., Brewer, R., 1984. Raman heterodyne interference of inequivalent nuclear sites. Phys. Rev. Lett. 52 (17), 1484–1487.

Miyakawa, T., Dexter, D.L., 1970. Phonon sidebands, multiphonon relaxation of excited states, and phonon-assisted energy transfer between ions in solids. Phys. Rev. B 1 (7), 2961–2969.

Mlynek, J., Wong, N.C., DeVoe, R.G., Kintzer, E.S., Brewer, R.G., 1983. Raman heterodyne detection of nuclear magnetic resonance. Phys. Rev. Lett. 50 (13), 993–996.

Moiseev, S.A., 2013. Off-resonant Raman-echo quantum memory for inhomogeneously broadened atoms in a cavity. Phys. Rev. A 88 (1), 012304.

Monz, T., Schindler, P., Barreiro, J.T., Chwalla, M., Nigg, D., Coish, W.A., Harlander, M., Hänsel, W., Hennrich, M., Blatt, R., 2011. 14-Qubit entanglement: creation and coherence. Phys. Rev. Lett. 106 (13), 130506.

Morton, J.J.L., Tyryshkin, A.M., Brown, R.M., Shankar, S., Lovett, B.W., Ardavan, A., Schenkel, T., Haller, E.E., Ager, J.W., Lyon, S.A., 2008. Solid-state quantum memory using the ^{31}P nuclear spin. Nature 455 (7216), 1085–1088.

Nielsen, M.A., Chuang, I.L., 2000. Quantum Computation and Quantum Information. Cambridge University Press, Cambridge, UK.

Nilsson, M., Kröll, S., 2005. Solid state quantum memory using complete absorption and re-emission of photons by tailored and externally controlled inhomogeneous absorption profiles. Opt. Commun. 247 (4–6), 393–403.

Nilsson, M., Rippe, L., Kröll, S., Klieber, R., Suter, D., 2004. Hole-burning techniques for isolation and study of individual hyperfine transitions in inhomogeneously broadened solids demonstrated in Pr^{3+}:Y_2SiO_5. Phys. Rev. B 70 (21), 214116.

Northup, T.E., Blatt, R., 2014. Quantum information transfer using photons. Nat. Photonics 8 (5), 356–363.

Ohlsson, N., Krishna Mohan, R., Kröll, S., 2002. Quantum computer hardware based on rare-earth-ion-doped inorganic crystals. Opt. Commun. 201 (1–3), 71–77.

Pascual-Winter, M., Tongning, R., Lauro, R., Louchet-Chauvet, A., Chanelière, T., Le Gouët, J.-L., 2012a. Adiabatic passage with spin locking in Tm^{3+}:YAG. Phys. Rev. B 86 (6), 064301.

Pascual-Winter, M., Tongning, R.C., Chanelière, T., Le Gouët, J.-L., 2012b. Spin coherence lifetime extension in Tm^{3+}:YAG through dynamical decoupling. Phys. Rev. B 86 (18), 184301.

Peacock, R.D., 1975. The intensities of lanthanide f-f transitions. Struct. Bond. 22, 83.

Peev, M., Pacher, C., Alléaume, R., Barreiro, C., Bouda, J., Boxleitner, W., Debuisschert, T., Diamanti, E., Dianati, M., Dynes, J.F., Fasel, S., Fossier, S., Fürst, M., Gautier, J.-D., Gay, O., Gisin, N., Grangier, P., Happe, A., Hasani, Y., Hentschel, M., Hübel, H., Humer, G., Länger, T., Legré, M., Lieger, R., Lodewyck, J., Lorünser, T., Lütkenhaus, N., Marhold, A., Matyus, T., Maurhart, O., Monat, L., Nauerth, S., Page, J.-B., Poppe, A., Querasser, E., Ribordy, G., Robyr, S., Salvail, L., Sharpe, A.W., Shields, A.J., Stucki, D., Suda, M., Tamas, C., Themel, T., Thew, R.T., Thoma, Y., Treiber, A., Trinkler, P., Tualle-Brouri, R., Vannel, F., Walenta, N., Weier, H., Weinfurter, H., Wimberger, I., Yuan, Z.L., Zbinden, H., Zeilinger, A., 2009. The SECOQC quantum key distribution network in Vienna. New J. Phys. 11 (7), 075001.

Peng, X., Suter, D., Lidar, D.A., 2011. High fidelity quantum memory via dynamical decoupling: theory and experiment. J. Phys. B At. Mol. Opt. Phys. 44 (15), 154003.

Perrot, A., Goldner, P., Giaume, D., Lovrić, M., Andriamiadamanana, C., Gonçalves, R.R., Ferrier, A., 2013. Narrow optical homogeneous linewidths in rare earth doped nanocrystals. Phys. Rev. Lett. 111 (20), 203601.

Popova, M.N., Chukalina, E.P., Malkin, B.Z., Saikin, S.K., 2000. Experimental and theoretical study of the crystal-field levels and hyperfine and electron-phonon interactions in $LiYF_4$: Er^{3+}. Phys. Rev. B 61 (11), 7421.

Probst, S., Rotzinger, H., Wünsch, S., Jung, P., Jerger, M., Siegel, M., Ustinov, A.V., Bushev, P.A., 2013. Anisotropic rare-earth spin ensemble strongly coupled to a superconducting resonator. Phys. Rev. Lett. 110 (15), 157001.

Pryde, G., Sellars, M.J., Manson, N.B., Feb. 2000. Solid state coherent transient measurements using hard optical pulses. Phys. Rev. Lett. 84 (6), 1152–1155.

Pytalev, D.S., Chukalina, E.P., Popova, M.N., Shakurov, G.S., Malkin, B.Z., Korableva, S.L., 2012. Hyperfine interactions of Ho^{3+} ions in KY_3F_{10}: electron paramagnetic resonance and optical spectroscopy studies. Phys. Rev. B 86 (11), 115124.

Rabi, I., 1937. Space quantization in a gyrating magnetic field. Phys. Rev. 51 (8), 652–654.

Rieländer, D., Kutluer, K., Ledingham, P.M., Gündoğan, M., Fekete, J., Mazzera, M., de Riedmatten, H., 2014. Quantum storage of heralded single photons in a praseodymium-doped crystal. Phys. Rev. Lett. 112 (4), 040504.

Rippe, L., Nilsson, M., Kröll, S., Klieber, R., Suter, D., 2005. Experimental demonstration of efficient and selective population transfer and qubit distillation in a rare-earth-metal-ion-doped crystal. Phys. Rev. A 71 (6), 062328.

Rippe, L., Julsgaard, B., Walther, A., Ying, Y., Kröll, S., 2008. Experimental quantum-state tomography of a solid-state qubit. Phys. Rev. A 77 (2), 022307.

Roos, I., Mølmer, K., 2004. Quantum computing with an inhomogeneously broadened ensemble of ions: suppression of errors from detuning variations by specially adapted pulses and coherent population trapping. Phys. Rev. A 69 (2), 022321.

Ruggiero, J., Simon, C., Chanelière, T., 2009. Why the two-pulse photon echo is not a good quantum memory protocol. Phys. Rev. A 79 (5), 053851.

Sabooni, M., Li, Q., Kröll, S., Rippe, L., 2013. Efficient quantum memory using a weakly absorbing sample. Phys. Rev. Lett. 110 (13), 133604.

Saglamyurek, E., Sinclair, N., Jin, J., Slater, J.A., Oblak, D., Bussières, F., George, M., Ricken, R., Sohler, W., Tittel, W., 2011. Broadband waveguide quantum memory for entangled photons. Nature 469 (7331), 512–515.

Sangouard, N., Simon, C., Minář, J., Afzelius, M., Chanelière, T., Gisin, N., Le Gouët, J.-L., de Riedmatten, H., Tittel, W., 2010. Impossibility of faithfully storing single photons with the three-pulse photon echo. Phys. Rev. A 81 (6), 062333.

Sasaki, M., Fujiwara, M., Ishizuka, H., Klaus, W., Wakui, K., Takeoka, M., Miki, S., Yamashita, T., Wang, Z., Tanaka, A., Yoshino, K., Nambu, Y., Takahashi, S., Tajima, A., Tomita, A., Domeki, T., Hasegawa, T., Sakai, Y., Kobayashi, H., Asai, T., Shimizu, K., Tokura, T., Tsurumaru, T., Matsui, M., Honjo, T., Tamaki, K., Takesue, H., Tokura, Y., Dynes, J.F., Dixon, A.R., Sharpe, A.W., Yuan, Z.L., Shields, A.J., Uchikoga, S., Legré, M., Robyr, S., Trinkler, P., Monat, L., Page, J.-B., Ribordy, G., Poppe, A., Allacher, A., Maurhart, O., Länger, T., Peev, M., Zeilinger, A., 2011. Field test of quantum key distribution in the Tokyo QKD Network. Opt. Express 19 (11), 10387–10409.

Scarani, V., Bechmann-Pasquinucci, H., Cerf, N., Dušek, M., Lütkenhaus, N., Peev, M., 2009. The security of practical quantum key distribution. Rev. Mod. Phys. 81 (3), 1301–1350.

Sellars, M.J., Meltzer, R.S., Fisk, P.T.H., Manson, N.B., 1994. Time-resolved ultranarrow optical hole burning of a crystalline solid: Y_2O_3:Eu^{3+}. J. Opt. Soc. Am. B 11 (8), 1468–1473.

Serrano, D., Yan, Y., Karlsson, J., Rippe, L., Walther, A., Kröll, S., Ferrier, A., Goldner, P., 2014. Impact of the ion-ion energy transfer on quantum computing schemes in rare-earth doped solids. J. Lumin. 151, 93–99.

Shor, P.W., 1994. Algorithms for quantum computation: discrete logarithms and factoring. In: 35th Annu. Symp. Found. Comput. Sci. Los Alamitos, USA, pp. 124–134.

Shor, P.W., 1996. Fault-tolerant quantum computation. In: 37th Annu. Symp. Found. Comput. Sci. Los Alamitos, USA, pp. 56–65.

Siyushev, P., Xia, K., Reuter, R., Jamali, M., Zhao, N., Yang, N., Duan, C., Kukharchyk, N., Wieck, A.D., Kolesov, R., Wrachtrup, J., 2014. Coherent properties of single rare-earth spin qubits. Nat. Commun. 5, 3895.

Souza, A., Álvarez, G., Suter, D., 2011. Robust dynamical decoupling for quantum computing and quantum memory. Phys. Rev. Lett. 106 (24), 240501.

Souza, A.M., Álvarez, G.A., Suter, D., 2012. Robust dynamical decoupling. Philos. Trans. R. Soc. A 370 (1976), 4748–4769.

Staudt, M.U., Hoi, I.-C., Krantz, P., Sandberg, M., Simoen, M., Bushev, P., Sangouard, N., Afzelius, M., Shumeiko, V.S., Johansson, G., Delsing, P., Wilson, C.M., 2012. Coupling of an erbium spin ensemble to a superconducting resonator. J. Phys. B At. Mol. Opt. Phys. 45 (12), 124019.

Sternheimer, R., 1966. Shielding and antishielding effects for various ions and atomic systems. Phys. Rev. 146 (1), 140–160.

Sternheimer, R., 1967. Quadrupole shielding and antishielding factors for atomic states. Phys. Rev. 164 (1), 10–20.

Stolze, J., Suter, D., 2008. Quantum Computing: A Short Course from Theory to Experiment, second ed. Wiley-VCH, Berlin, Germany.

Stucki, D., Walenta, N., Vannel, F., Thew, R.T., Gisin, N., Zbinden, H., Gray, S., Towery, C.R., Ten, S., 2009. High rate, long-distance quantum key distribution over 250 km of ultra low loss fibres. New J. Phys. 11 (7), 075003.

Stucki, D., Legré, M., Buntschu, F., Clausen, B., Felber, N., Gisin, N., Henzen, L., Junod, P., Litzistorf, G., Monbaron, P., Monat, L., Page, J.-B., Perroud, D., Ribordy, G., Rochas, A., Robyr, S., Tavares, J., Thew, R., Trinkler, P., Ventura, S., Voirol, R., Walenta, N., Zbinden, H., 2011. Long-term performance of the SwissQuantum quantum key distribution network in a field environment. New J. Phys. 13 (12), 123001.

Sun, Y.C., 2005. Rare earth materials in optical storage and data processing applications. In: Liu, G., Jacquier, B. (Eds.), Spectroscopic Properties of Rare Earths in Optical Materials. Springer, Berlin, pp. 379–429.

Sun, Y., Thiel, C.W., Cone, R.L., Equall, R.W., Hutcheson, R.L., 2002. Recent progress in developing new rare earth materials for hole burning and coherent transient applications. J. Lumin. 98 (1), 281–287.

Sun, Y., Böttger, T., Thiel, C.W., Cone, R., 2008. Magnetic g tensors for the $^4I_{15/2}$ and $^4I_{13/2}$ states of Er^{3+}:Y_2SiO_5. Phys. Rev. B 77 (8), 085124.

Sun, Y., Thiel, C.W., Cone, R., 2012. Optical decoherence and energy level structure of 0.1%Tm^{3+}:$LiNbO_3$. Phys. Rev. B 85 (16), 165106.

Thiel, C.W., Macfarlane, R.M., Böttger, T., Sun, Y., Cone, R.L., Babbitt, W.R., 2010. Optical decoherence and persistent spectral hole burning in Er^{3+}:$LiNbO_3$. J. Lumin. 130 (9), 1603–1609.

Thiel, C.W., Böttger, T., Cone, R.L., 2011. Rare-earth-doped materials for applications in quantum information storage and signal processing. J. Lumin. 131 (3), 353–361.

Thiel, C.W., Babbitt, W., Cone, R., 2012. Optical decoherence studies of yttrium oxyorthosilicate Y_2SiO_5 codoped with Er^{3+} and Eu^{3+} for optical signal processing and quantum information applications at 1.5 microns. Phys. Rev. B 85 (17), 174302.

Thorpe, M.J., Rippe, L., Fortier, T.M., Kirchner, M.S., Rosenband, T., 2011. Frequency stabilization to 6×10^{-16} via spectral-hole burning. Nat. Photonics. 5 (11), 688–693.

Timoney, N., Lauritzen, B., Usmani, I., Afzelius, M., Gisin, N., Timoney, N., Lauritzen, B., Usmani, I., Afzelius, M., Gisin, N., 2012. Atomic frequency comb memory with spin-wave storage in $^{153}Eu^{3+}$:Y_2SiO_5. J. Phys. B At. Mol. Opt. Phys. 45 (12), 124001.

Timoney, N., Usmani, I., Jobez, P., Afzelius, M., Gisin, N., 2013. Single-photon-level optical storage in a solid-state spin-wave memory. Phys. Rev. A 88 (2), 022324.

Tittel, W., Chanelière, T., Cone, R.L., Kröll, S., Moiseev, S.A., Sellars, M.J., 2010. Photon-echo quantum memory in solid state systems. Laser & Photon. Rev. 4 (2), 244–267.

Turukhin, A., Sudarshanam, V., Shahriar, M., Musser, J., Ham, B., Hemmer, P., 2001. Observation of ultraslow and stored light pulses in a solid. Phys. Rev. Lett. 88 (2), 023602.

Usmani, I., Afzelius, M., de Riedmatten, H., Gisin, N., 2010. Mapping multiple photonic qubits into and out of one solid-state atomic ensemble. Nat. Commun. 1, 12.

Usmani, I., Clausen, C., Bussières, F., Sangouard, N., Afzelius, M., Gisin, N., 2012. Heralded quantum entanglement between two crystals. Nat. Photonics 6 (4), 234–237.

Utikal, T., Eichhammer, E., Petersen, L., Renn, A., Götzinger, S., Sandoghdar, V., 2014. Spectroscopic detection and state preparation of a single praseodymium ion in a crystal. Nat. Commun. 5, 3627.

Viola, L., Lloyd, S., 1998. Dynamical suppression of decoherence in two-state quantum systems. Phys. Rev. A 58 (4), 2733–2744.

Wesenberg, J., Mølmer, K., Rippe, L., Kröll, S., 2007. Scalable designs for quantum computing with rare-earth-ion-doped crystals. Phys. Rev. A 75 (1), 012304.

Wong, N.C., Kintzer, E.S., Mlynek, J., DeVoe, R.G., Brewer, R.G., 1983. Raman heterodyne detection of nuclear magnetic resonance. Phys. Rev. B 28 (9), 4993–5010.

Wrachtrup, J., Jelezko, F., 2006. Processing quantum information in diamond. J. Phys. Condens. Matter 18 (21), S807–S824.

Xu, H., Nilsson, M., Ohser, S., Rauhut, N., Kröll, S., Aguiló, M., Díaz, F., 2004. Hyperfine structure and homogeneous broadening in Pr^{3+}:$KY(WO_4)_2$. Phys. Rev. B 70 (21), 214115.

Yan, Y., Karlsson, J., Rippe, L., Walther, A., Serrano, D., Lindgren, D., Pistol, M.-e, Kröll, S., Goldner, P., Zheng, L., Xu, J., 2013. Measurement of linewidths and permanent electric dipole moment change of the Ce 4f-5d transition in Y_2SiO_5 for qubit readout scheme in rare-earth ion based quantum computing. Phys. Rev. B 87 (18), 184205.

Yang, W., Wang, Z.-Y., Liu, R.-B., 2010. Preserving qubit coherence by dynamical decoupling. Front. Phys. 6 (1), 2–14.
Yin, C., Rancic, M., de Boo, G.G., Stavrias, N., McCallum, J.C., Sellars, M.J., Rogge, S., 2013. Optical addressing of an individual erbium ion in silicon. Nature 497 (7447), 91–94.
Zhou, Z.-Q., Lin, W.-B., Yang, M., Li, C.-F., Guo, G.-C., 2012. Realization of reliable solid-state quantum memory for photonic polarization qubit. Phys. Rev. Lett. 108 (19), 190505.

Chapter 268

REY-Rich Mud: A Deep-Sea Mineral Resource for Rare Earths and Yttrium

Kentaro Nakamura[*,†], Koichiro Fujinaga[*,‡], Kazutaka Yasukawa[*], Yutaro Takaya[†], Junichiro Ohta[*], Shiki Machida[§], Satoru Haraguchi[¶] and Yasuhiro Kato[*,†,‡]

[*]*Department of Systems Innovation, School of Engineering, The University of Tokyo, Bunkyo-ku, Japan*

[†]*Research and Development Center for Submarine Resources, Japan Agency for Marine-Earth Science and Technology (JAMSTEC), Yokosuka, Japan*

[‡]*Frontier Research Center for Energy and Resources (FRCER), School of Engineering, The University of Tokyo, Bunkyo-ku, Japan*

[§]*Department of Resources and Environmental Engineering, School of Creative Science and Engineering, Waseda University, Shinjyu-ku, Japan*

[¶]*Department of Solid Earth Geochemistry, Japan Agency for Marine-Earth Science and Technology (JAMSTEC), Yokosuka, Japan*

Chapter Outline

Handbook on the Physics and Chemistry of Rare Earths, Vol. 46. http://dx.doi.org/10.1016/B978-0-444-63260-9.00268-6

1 INTRODUCTION

Rare-earth elements and yttrium (together known as REY) are widely recognized as strategic materials for high-technology applications (e.g., laptop computers, flat screen televisions, cell phones, MRI scanners, and medicine) and green energy technologies (e.g., electric and hybrid vehicles, wind power generators, and compact fluorescent lighting) (Table 1). World demand for REY is increasing rapidly (Fig. 1) (Humphries, 2010; Roskill Information Services Ltd., 2007; USGS, 2013) and a stable supply of REY is key to future development of technology and the global economy.

At present, ~90% of the world's production of REY is from China, although China has only half of known global reserves; the United States, India, Australia, and other countries together have another half (Fig. 2) (USGS, 2013). China's dominance pertains especially to heavy rare-earth elements (HREE; conventionally Gd to Lu, but Eu is included here), which are important materials for high-technology products including electronic, clean energy, and military technological devices (Service, 2010). In contrast to light REE (LREE), which can be obtained from carbonatite/alkaline igneous complexes in many countries, known HREE reserves are almost all in ion-adsorption-type ore deposits in southern China (e.g., Longnan and Xinxiu ore deposits), which are characterized by larger proportions of HREE (Fig. 3). Therefore, diversification of sources and increased access to REY resources, especially HREE, are important to maintain supply capable of meeting the ever-rising demand for the rare earths.

Kato et al. (2011) reported the potential of deep-sea REY-rich mud in the Pacific Ocean as a new source of REY. Their study was based on investigations of drill core samples from 51 sites of the Deep Sea Drilling Project (DSDP) and Ocean Drilling Program (ODP), and piston core samples obtained from 27 sites by the Ocean Research Institute of the University of Tokyo; together, these samples cover much of the Pacific Ocean (Fig. 4). Chemical analyses of 2037 bulk-sediment samples revealed the mud to have high REY resource potential, especially for HREE; the muds commonly have considerably higher concentrations of REE (including HREE) than the ion-adsorption-type ore deposits in southern China (Kato et al., 2011; Fig. 5). In this chapter, we describe the distribution of REY-rich muds and discuss the lithology, geochemistry, and genesis of the deposits. We also describe possible development systems and processes for the REY-rich mud deposits.

2 DISTRIBUTION OF REY-RICH MUDS

REY-rich mud is defined as deep-sea sediment containing more than 400 ppm of total REY (hereafter, ΣREY), which is comparable to ΣREY in ion-adsorption-type ore deposits in southern China (Bao and Zhao, 2008; Wu et al., 1990, 1996). Several types of seafloor sediment have been reported to

TABLE 1 Industrial Applications of Rare-Earth Elements

	Element	Application
Light rare earths (LREE)	Lanthanum [La]	• Optical glass • Ceramic condensers • Catalysts • Phosphors • Rechargeable nickel–metal hydride batteries
	Cerium [Ce]	• Polishing powders • Catalysts • UV cut glass • Glass decolorizers • Rechargeable nickel–metal hydride batteries
	Praseodymium [Pr]	• Nd magnets • Ceramic tile coloring • Rechargeable nickel–metal hydride batteries
	Neodymium [Nd]	• Nd magnets • Ceramic condensers • Rechargeable nickel–metal hydride batteries
	Samarium [Sm]	• Sm–Co magnets
	Europium [Eu]	• Phosphor (red)
Heavy rare earths (HREE)	Gadolinium [Gd]	• Optical glass • Neutron shielding material for atomic reactors
	Terbium [Tb]	• Phosphor (green) • Magnetic optical disk targets • Nd magnets • Giant magnetostrictive material
	Dysprosium [Dy]	• Nd magnets • Giant magnetostrictive material
	Holmium [Ho]	• Lasers • Magnetic superconductive material
	Erbium [Er]	• Erbium-doped fiber amplifiers • Crystal glass colorant
	Thulium [Tm]	• Lasers • Thulium-doped fiber amplifiers
	Ytterbium [Yb]	• Lasers • Visible upconversion
	Lutetium [Lu]	• Scintillators
	Yttrium [Y]	• Phosphor (red) • Optical glass • Yttria-stabilized zirconia • Anodic/cathodic material for rechargeable batteries • High-temperature superconductors

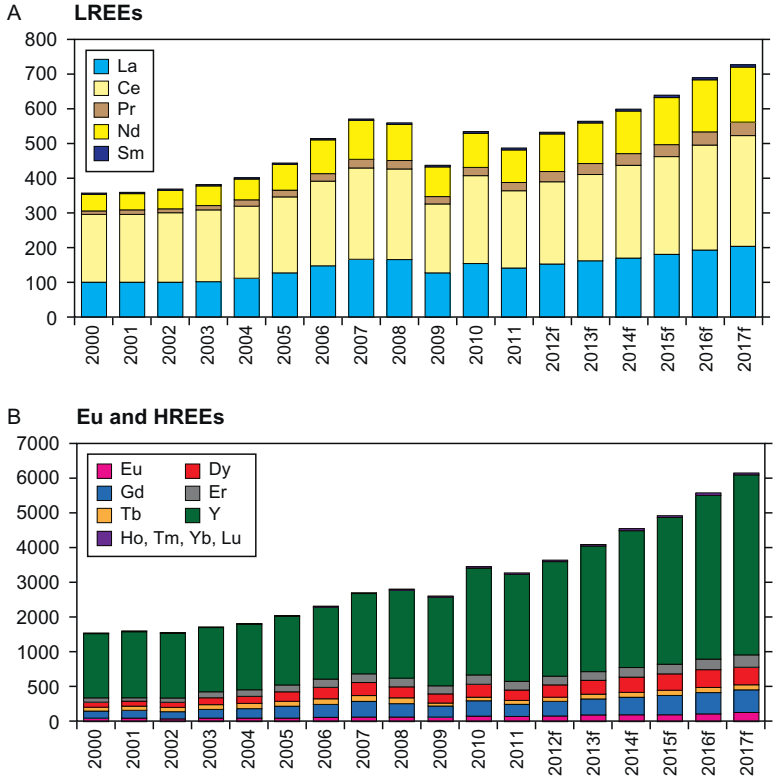

FIGURE 1 Global demand for rare earths from 2000 to 2017. (A) Normalized demand for LREEs (except Eu). La in 2000 = 100. (B) Normalized demand for Eu and HREEs. Eu in 2000 = 100. f = forecast. *Modified from Shaw and Chegwidden (2012).*

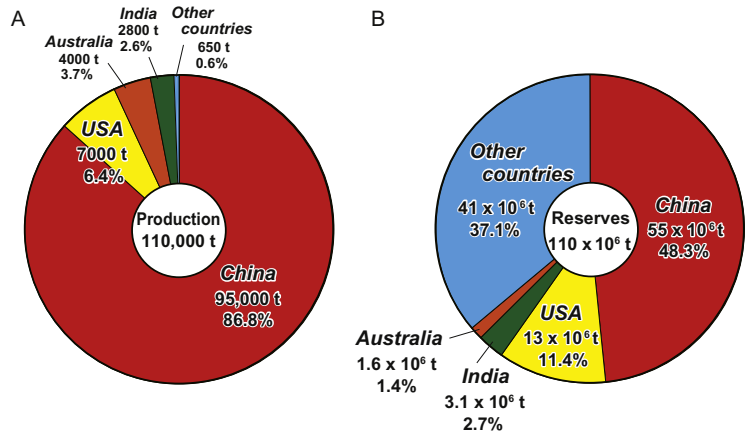

FIGURE 2 Global rare-earth (A) production and (B) reserves in 2012 (USGS, 2013).

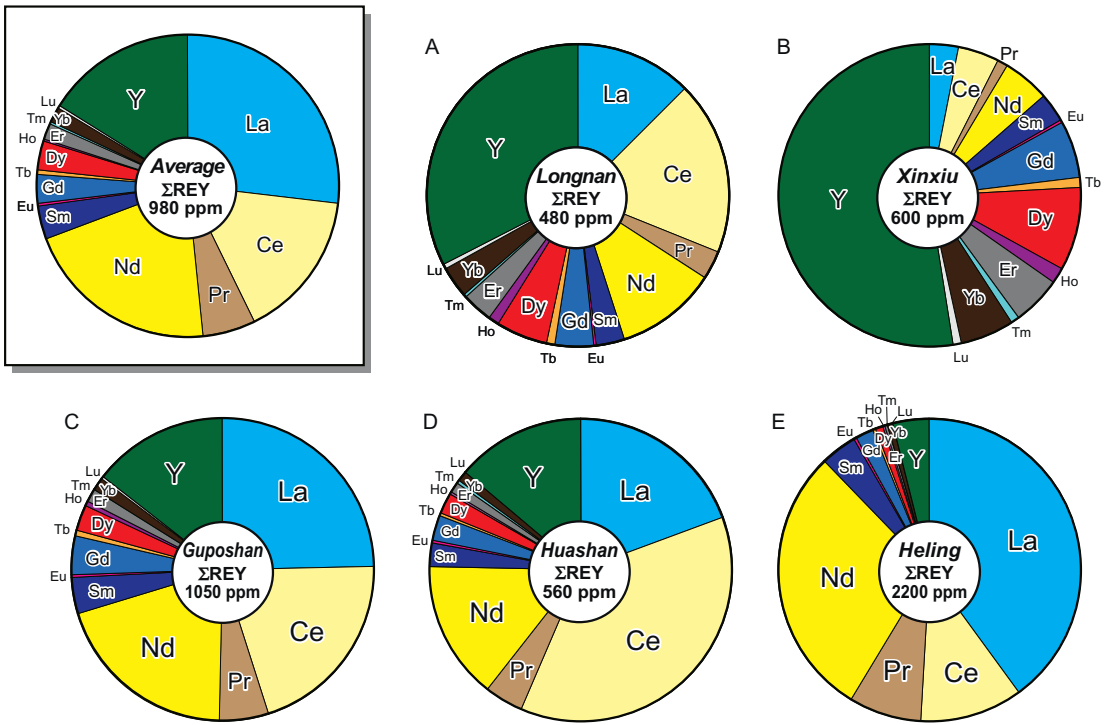

FIGURE 3 REY contents of ion-adsorption-type ore deposits in southern China. *Data from Wu et al. (1990) and Bao and Zhao (2008).*

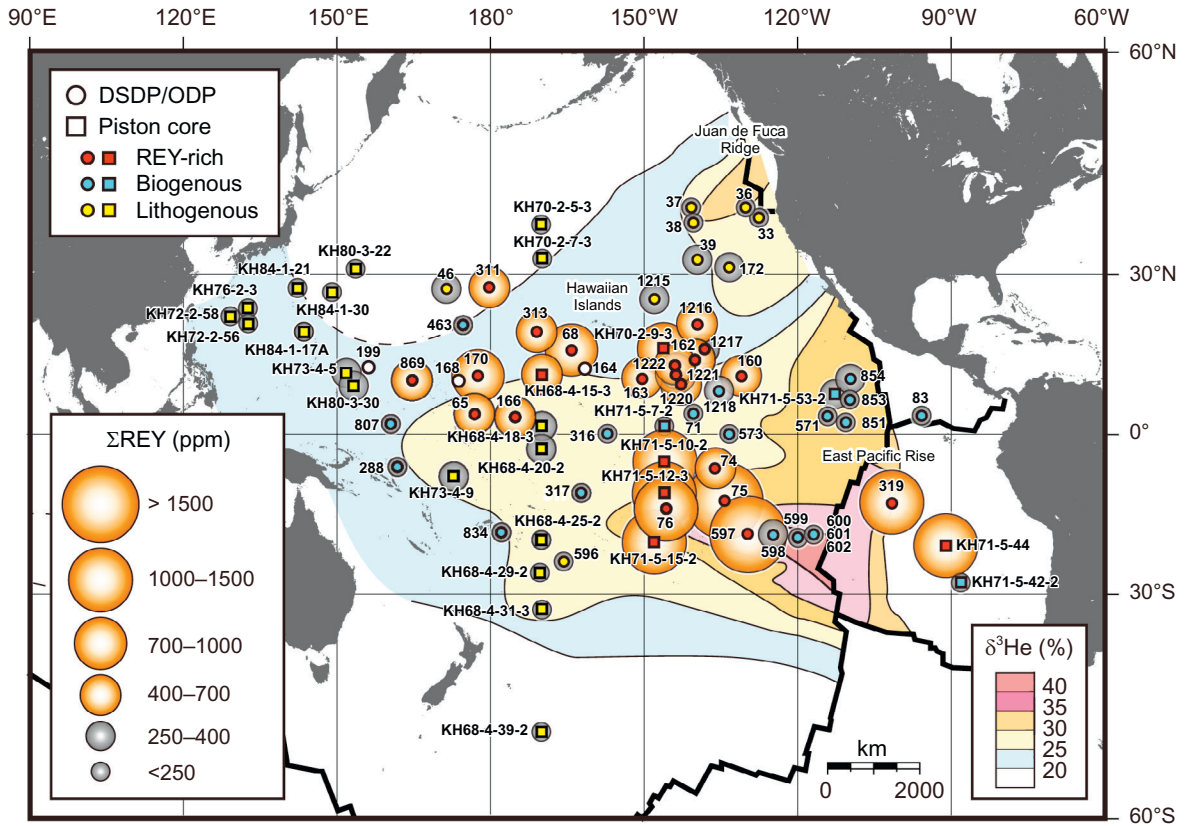

FIGURE 4 Distribution of average ΣREY contents in surface sediments (less than 2 m below seafloor) in the Pacific Ocean (Kato et al., 2011). Circles and squares represent DSDP/ODP sites and University of Tokyo (UT) piston core sites, respectively, with colors (red, blue, and yellow) (dark gray, gray, and light gray in the print version) corresponding to the dominant origin of surface sediments. Open symbols are sites lacking samples from the sediment surface. Contours represent helium-3 anomalies (δ^3He) of mid-depth seawater (Lupton, 1995).

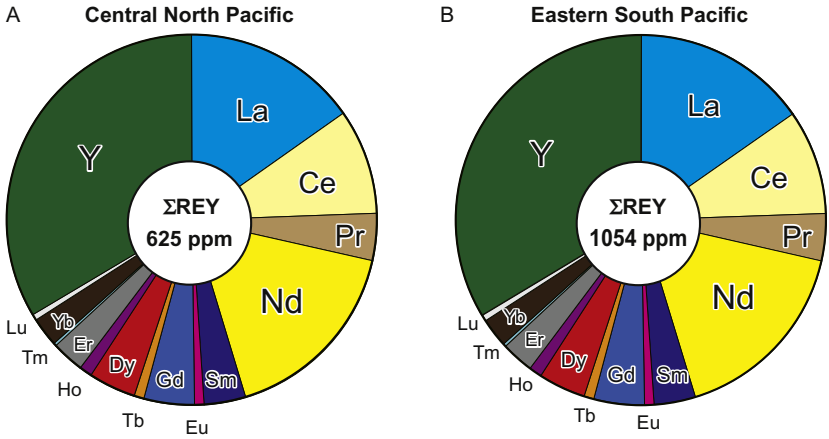

FIGURE 5 REY contents of REY-rich mud in (A) the central North and (B) eastern South Pacific. *Data from Kato et al. (2011).*

contain high concentrations of REY (Courtois and Clauer, 1980; Dubinin and Sval'nov, 2000; Murray and Leinen, 1993; Ruhlin and Owen, 1986). However, seafloor sediments have not been regarded as a REY resource because of insufficient data on the spatial distribution of the REY-enriched sediments.

Kato et al. (2011) discovered that REY-rich deep-sea muds are distributed over large areas of the Pacific Ocean (Fig. 4) on the basis of the elemental compositions of more than 2000 samples collected at ~1-m depth intervals from sediment cores from 78 sites in the Pacific Ocean. Their results clearly indicate the potential of REY-rich deep-sea mud as a source of REY. More recently, Yasukawa et al. (2014) recognized REY-rich muds in the Indian Ocean (Fig. 6 and Table 2).

2.1 Pacific Ocean

REY-rich muds in the Pacific Ocean are found mainly in pelagic region at water depths of greater than 4000 m in areas more than 2000 km from land. On the basis of chemical analyses of mud samples from 78 sites in the Pacific Ocean, Kato et al. (2011) demonstrated that REY-rich muds are distributed mainly in two regions: the eastern South Pacific and central North Pacific (Fig. 6 and Table 2).

In the eastern South Pacific region, REY-rich mud layers are less than ~10 m thick. They have ΣREY contents of 1000–2230 ppm with total HREE concentrations (ΣHREE) of 200–430 ppm (Figs. 7 and 8), which are comparable to or greater than those of ion-adsorption-type deposits in southern China (ΣREY contents of 500–2000 ppm with 50–200 ppm ΣHREE; Bao and Zhao, 2008; Wu et al., 1990, 1996). There are relatively thin (under 3 m) REY-rich mud layers with very high average ΣREY contents that

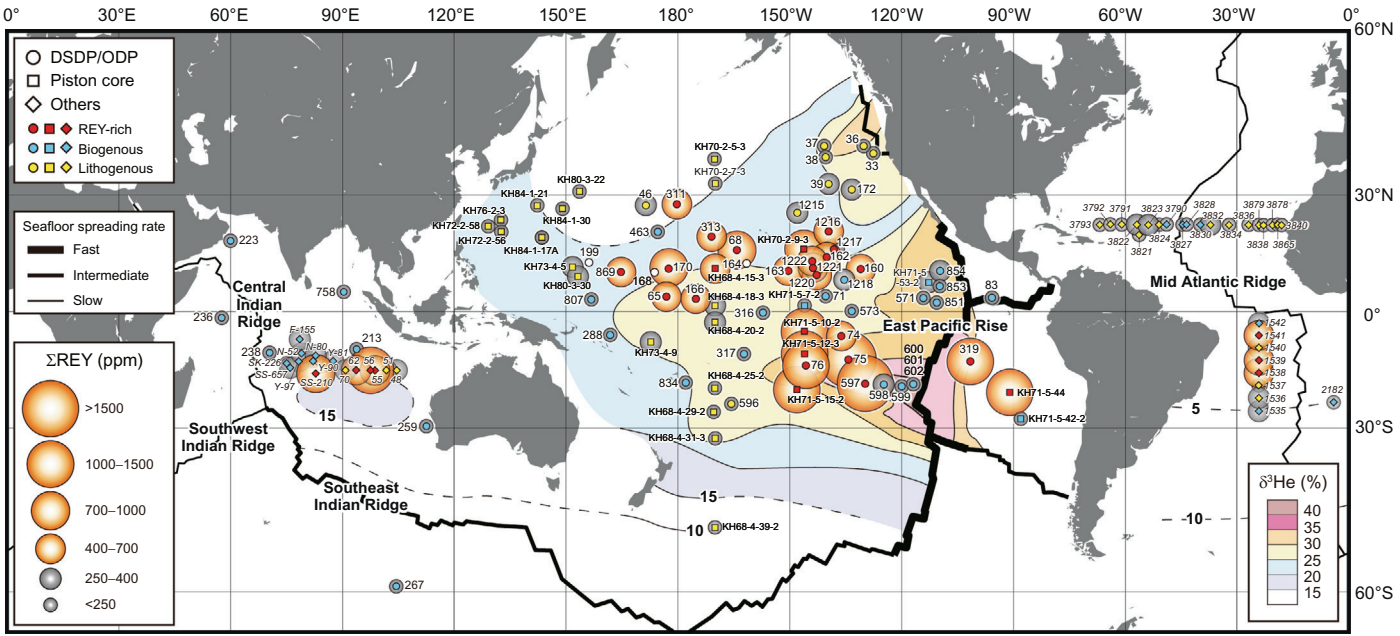

FIGURE 6 Global compilation of average ΣREY contents for deep-sea muds (less than 2 m below seafloor). Circles, squares, and diamonds represent DSDP/ODP sites, UT piston core sites analyzed by Kato et al. (2011), and other sites from previous studies (listed in Table 2), respectively. The color-coding is the same as in Fig. 4. Because most of these data sets do not include the full suite of REEs, missing REEs were estimated by correlations among REE contents derived from the complete data set of Pacific Ocean sediment compositions (Kato et al., 2011; correlation method described in footnote of Table 2). Relative spreading rates of MORs are also shown here.

TABLE 2 Compilation of Global Data on ΣREY Contents of Seafloor Sediments (<2 mbsf)

Site/Station No.	Latitude	Longitude	Area	Water Depth (m)	Average ΣREY (ppm)	Data Source[a]
Pacific Ocean						
DSDP Site 33	39°28.48′N	127°29.81′W	Northeast Pacific	4284	143	1
DSDP Site 36	40°59.08′N	130°06.58′W	Northeast Pacific	3273	177	1
DSDP Site 37	40°58.74′N	140°43.11′W	Northeast Pacific	4682	219	1
DSDP Site 38	38°42.12′N	140°21.27′W	Northeast Pacific	5134	222	1
DSDP Site 39	32°48.28′N	139°34.29′W	Northeast Pacific	4929	380	1
DSDP Site 46	27°53′N	171°26.30′E	North Central Pacific	5768.9	350	1
DSDP Site 65	04°21.21′N	176°59.16′E	Central Pacific	6130	490	1
DSDP Site 68	16°43.32′N	164°10.36′W	Central Pacific	5467	963	1
DSDP Site 71	04°28.28′N	140°18.91′W	Central Equatorial Pacific	4419	80	1
DSDP Site 74	06°14.20′S	136°05.80′W	Southeast Pacific	4431	594	1
DSDP Site 75	12°31′S	134°16′W	Southeast Pacific	4181	1536	1
DSDP Site 76/76A	14°05.90′S	145°39.64′W	Southeast Pacific	4597.9	1122	1
DSDP Site 83	04°02.80′N	95°44.25′W	Eastern Equatorial Pacific	3645.7	119	1
DSDP Site 160	11°42.27′N	130°52.81′W	Central Tropical Pacific	4940	449	1

Continued

TABLE 2 Compilation of Global Data on ΣREY Contents of Seafloor Sediments (<2 mbsf)—Cont'd

Site/Station No.	Latitude	Longitude	Area	Water Depth (m)	Average ΣREY (ppm)	Data Source[a]
DSDP Site 162	14°52.19′N	140°02.61′W	Central Tropical Pacific	4854	444	1
DSDP Site 163	11°14.66′N	150°17.52′W	Central Tropical Pacific	5230	675	1
DSDP Site 164	13°12.14′N	161°30.98′W	Central Pacific	5499	–	1
DSDP Site 166	03°45.70′N	175°04.80′W	Central Pacific	4962	609	1
DSDP Site 168	10°42.20′N	173°35.90′E	Central Pacific	5420	–	1
DSDP Site 170	11°48′N	177°37′E	Central Pacific	5792	925	1
DSDP Site 172	31°32.23′N	133°22.36′W	Northeast Pacific	4767	262	1
DSDP Site 199	13°30.80′N	156°10.30′E	Western Pacific	6090	–	1
DSDP Site 288	05°58.35′S	161°49.53′E	Southwest Pacific	3000	59	1
DSDP Site 311	28°07.46′N	179°44.25′E	North Central Pacific	5775	439	1
DSDP Site 313	20°10.52′N	170°57.15′W	Central Pacific	3484	327	1
DSDP Site 316	00°05.44′N	157°07.71′W	Central Pacific	4451	71	1
DSDP Site 317B	11°00.09′S	162°15.78′W	Central Pacific	2598	44	1
DSDP Site 319	13°01.04′S	101°31.46′W	Southeast Pacific	4296	1168	1
DSDP Site 463	21°21.01′N	174°40.07′E	North Central Pacific	2525	142	1
DSDP Site 571	03°59.84′N	114°08.53′W	Eastern Equatorial Pacific	3962	73	1

DSDP Site 573/573A	00°29.91′N	133°18.57′W	Central Equatorial Pacific	4301	49	1
DSDP Site 596	23°51.20′S	165°39.27′W	Southwest Pacific	5701	193	1
DSDP Site 597A	18°48.43′S	129°46.22′W	Southeast Pacific	4162.6	1487	1
DSDP Site 598	19°00.28′S	124°40.61′W	Southeast Pacific	3699	291	1
DSDP Site 599	19°27.09′S	119°52.88′W	Southeast Pacific	3654	168	1
DSDP Site 600C	18°55.70′S	116°50.45′W	Southeast Pacific	3398	87	1
DSDP Site 601	18°55.22′S	116°52.11 W	Southeast Pacific	3433	50	1
DSDP Site 602B	18°54.41′S	116°54.68′W	Southeast Pacific	3535	128	1
ODP Site 807A	03°36.42′N	156°37.49′E	Western Equatorial Pacific	2803.8	68	1
ODP Site 834A	18°34.06′S	177°51.74 W	Southwest Pacific	2692.3	93	1
ODP Site 851B	02°46.22′N	110°34.31′W	Eastern Equatorial Pacific	3760.3	48	1
ODP Site 853B	07°12.66′N	109°45.08′W	Eastern Equatorial Pacific	3715.5	180	1
ODP Site 854C	11°13.43′N	109°35.65′W	Eastern Equatorial Pacific	3568.2	309	1
ODP Site 869A	11°00.09′N	164°44.97′E	Western Pacific	4826.7	686	1
ODP Site 1215A	26°01.77′N	147°55.99′W	Central Tropical Pacific	5395.6	286	1
ODP Site 1216A	21°27.16′N	139°28.79′W	Central Tropical Pacific	5152.5	442	1
ODP Site 1217A	16°52.01′N	138°06′W	Central Tropical Pacific	5342.1	365	1
ODP Site 1218A	08°53.37′N	135°22′W	Central Tropical Pacific	4826.3	257	1
ODP Site 1220A	10°10.60′N	142°45.49′W	Central Tropical Pacific	5217.9	523	1

Continued

TABLE 2 Compilation of Global Data on ΣREY Contents of Seafloor Sediments (<2 mbsf)—Cont'd

Site/Station No.	Latitude	Longitude	Area	Water Depth (m)	Average ΣREY (ppm)	Data Source[a]
ODP Site 1221A	12°02′N	143°41.65′W	Central Tropical Pacific	5175.3	322	1
ODP Site 1222A	13°48.98′N	143°53.35′W	Central Tropical Pacific	4988.7	485	1
KH68-4-15-3	12°00′N	169°58.5′W	Central Pacific	5050	498	1
KH68-4-18-3	01°59.5′N	170°00.5′W	Central Pacific	5470	307	1
KH68-4-20-2	02°28.4′S	169°59.7′W	Central Pacific	5130	343	1
KH68-4-25-2	19°59.1′S	170°01.6′W	Southwest Pacific	5300	153	1
KH68-4-29-2	25°54.4′S	170°19.5′W	Southwest Pacific	5600	204	1
KH68-4-31-3	32°09.2′S	169°56.3′W	Southwest Pacific	5650	169	1
KH68-4-39-2	50°07.2′S	169°58.9′W	Southwest Pacific	5190	210	1
KH70-2-5-3	38°25.5′N	170°05.7′W	North Central Pacific	5245	213	1
KH70-2-7-3	33°01.9′N	169°53.5′W	North Central Pacific	5420	227	1
KH70-2-9-3	17°05′N	146°12.3′W	Central Tropical Pacific	4950	651	1
KH71-5-7-2	02°00.8′N	145°59′W	Central Equatorial Pacific	4550	74	1
KH71-5-10-2	04°58.5′S	146°03.5′W	Southeast Pacific	4960	1035	1
KH71-5-12-3	11°01.4′S	146°01.5′W	Southeast Pacific	4830	1274	1
KH71-5-15-2	20°23′S	148°02′W	Southeast Pacific	4615	1047	1

KH71-5-42-2	27°34.8′S	88°03′W	Southeast Pacific	3690	86	1
KH71-5-44	21°S	93°W	Southeast Pacific	–	1124	1
KH71-5-53-2	08°15.3′N	112°42.1′W	Eastern Equatorial Pacific	3380	329	1
KH72-2-56	21°34′N	132°42′E	Philippine Sea	5360	245	1
KH72-2-58	22°53′N	129°13′E	Philippine Sea	5300	216	1
KH73-4-5	12°23.2′N	151°48′E	Western Pacific	5920	325	1
KH73-4-9	07°49.9′S	172°48.6′E	Central Pacific	5390	328	1
KH76-2-3	24°27.2′N	132°35.4′E	Philippine Sea	4750	221	1
KH80-3-22	31°16.2′N	153°42.9′E	Western Pacific	5750	130	1
KH80-3-30	09°50.6′N	153°13.5′E	Western Pacific	5480	355	1
KH84-1-17A	20°05.1′N	143°35′E	Philippine Sea	4140	117	1
KH84-1-21	27°55.1′N	142°22.3′E	Philippine Sea	3500	125	1
KH84-1-30	27°13.3′N	149°06.7′E	Western Pacific	5800	201	1
Indian Ocean						
DSDP Site 213	10°12.71′S	93°53.77′E	Wharton Basin	5609	199	2
DSDP Site 223	18°44.98′N	60°07.78′E	Arabian Sea	3633	78	2
DSDP Site 236	1°40.62′S	57°38.85′E	Western Equatorial Indian	4487	110	2
DSDP Site 238	11°09.21′S	70°31.56′E	Central Tropical Indian	2832	16	2
DSDP Site 259	29°37.05′S	112°41.78′E	Perth Abyssal Plain	4696	65	2
DSDP Site 267	59°15.74′S	104°29.30′E	Southern Ocean	4522	202	2

Continued

TABLE 2 Compilation of Global Data on ΣREY Contents of Seafloor Sediments (<2 mbsf)—Cont'd

Site/Station No.	Latitude	Longitude	Area	Water Depth (m)	Average ΣREY (ppm)	Data Source[a]
ODP Site 758A	5°23.049′N	90°21.673′E	Northeastern Tropical Indian	2924	131	2
48	15°20′S	104°20′E	Wharton Basin	–	389[b]	3
51	15°10′S	101°40′E	Wharton Basin	–	361[b]	3
55	15°S	98°E	Wharton Basin	–	573[b]	3
56	15°S	97°20′E	Wharton Basin	–	1190[b]	3
62	14°50′S	94°E	Wharton Basin	–	649[b]	3
70	14°50′S	91°10′E	Wharton Basin	–	346[b]	3
N-52	10°20′S	79°E	Central Indian Ocean Basin	–	261[b]	4
N-80	11°S	82°30′E	Central Indian Ocean Basin	–	258[b]	4
Y-81	12°20′S	87°20′E	Central Indian Ocean Basin	–	312[b]	4
Y-90	12°20′S	82°E	Central Indian Ocean Basin	–	215[b]	4
Y-97	12°20′S	78°20′E	Central Indian Ocean Basin	–	270[b]	4
F-155	6°50′S	78°30′E	Central Indian Ocean Basin	–	308[b]	4
SS-210	15°20′S	83°E	Central Indian Ocean Basin	–	786[b]	4
SK-226	13°S	75°E	Central Indian Ocean Basin	–	170[b]	4
SS-657	14°S	75°50′E	Central Indian Ocean Basin	–	275[b]	4

Atlantic Ocean						
Station 3793	22°20′N	67°09.5′W	Nares Abyssal plain	5720	219[b]	5
Station 3792	22°24.9′N	64°07′W	Nares Abyssal plain	5830	238[b]	5
Station 3791	22°28′N	61°18′W	Nares Abyssal plain	5900	245[b]	5
Station 3822	22°26′N	56°55.6′W	North American Basin	5250	276[b]	5
Station 3821	19°44.6′N	56°27.5′W	North American Basin	5050	248[b]	5
Station 3823	22°18.5′N	53°55′W	North American Basin	5055	289[b]	5
Station 3824	22°21′N	51°01′W	North American Basin	4960	230[b]	5
Station 3790	22°28.3′N	49°00.3′W	Mid-Atlantic Ridge	4560	141[b]	5
Station 3827	22°17′N	44°40.6′W	Mid-Atlantic Ridge	3680	104[b]	5
Station 3828	22°17.6′N	43°42′W	Mid-Atlantic Ridge	4230	84[b]	5
Station 3830	22°20′N	39°47.3′W	Mid-Atlantic Ridge	4810	121[b]	5
Station 3832	22°18.9′N	37°12.5′W	Canary Basin	6080	303[b]	5
Station 3834	22°18.6′N	32°03.6′W	Canary Basin	5080	180[b]	5
Station 3836	22°20′N	26°51′W	Canary Basin	5320	172[b]	5
Station 3879	22°16.5′N	24°05.2′W	African Continental Slope	5040	102[b]	5
Station 3838	22°13.2′N	22°48′W	African Continental Slope	4760	94[b]	5
Station 3878	22°16.9′N	20°28.4′W	African Continental Slope	4188	86[b]	5
Station 3865	22°18′N	19°01′W	African Continental Slope	3360	97[b]	5

Continued

TABLE 2 Compilation of Global Data on ΣREY Contents of Seafloor Sediments (<2 mbsf)—Cont'd

Site/Station No.	Latitude	Longitude	Area	Water Depth (m)	Average ΣREY (ppm)	Data Source[a]
Station 3840	22°17.6′N	17°58.8′W	African Continental Slope	1921	112[b]	5
Station 1535	25°35.7′S	24°02.4′W	Brazil Basin	4500	292[b]	6
Station 1536	22°17.6′S	24°01.1′W	Brazil Basin	5500	295[b]	6
Station 1537	19°05.5′S	24°02.9′W	Brazil Basin	5000	218[b]	6
Station 1538	15°52.9′S	24°04.6′W	Brazil Basin	5200	464[b]	6
Station 1539	12°41.1′S	24°02.1′W	Brazil Basin	5100	456[b]	6
Station 1540	9°22.4′S	24°02.1′W	Brazil Basin	5500	328[b]	6
Station 1541	6°10.8′S	24°01.1′W	Brazil Basin	5800	465[b]	6
Station 1542	2°59.1′S	24°01.2′W	Brazil Basin	5500	261[b]	6
Station 2182	23°30.52′S	4°17.19′W	Angola Basin	4990	115	7

[a] *1, Kato et al. (2011); 2, Yasukawa et al. (2014); 3, Pattan et al. (1995); 4, Pattan and Parthiban (2011); 5, Dubinin and Rozanov (2001); 6, Dubinin and Rimskaya-Korsakova (2011); 7, Dubinin et al. (2013).*

[b] *Individual REY contents that were not included were estimated from the data provided by using correlations among REE contents derived from the entire data set of Pacific Ocean sediment compositions. For data sources 3 and 4, missing data for Pr, Tb, and Tm were calculated using Nd, Gd, and Er data, respectively, based on linear correlations of the entire Pacific Ocean data set (R^2 for each pair >0.99). For data sources 5 and 6, missing data for Y were calculated using Lu data based on a second-order approximation curve ($R^2 = 0.984$) for the entire Pacific Ocean data set.*

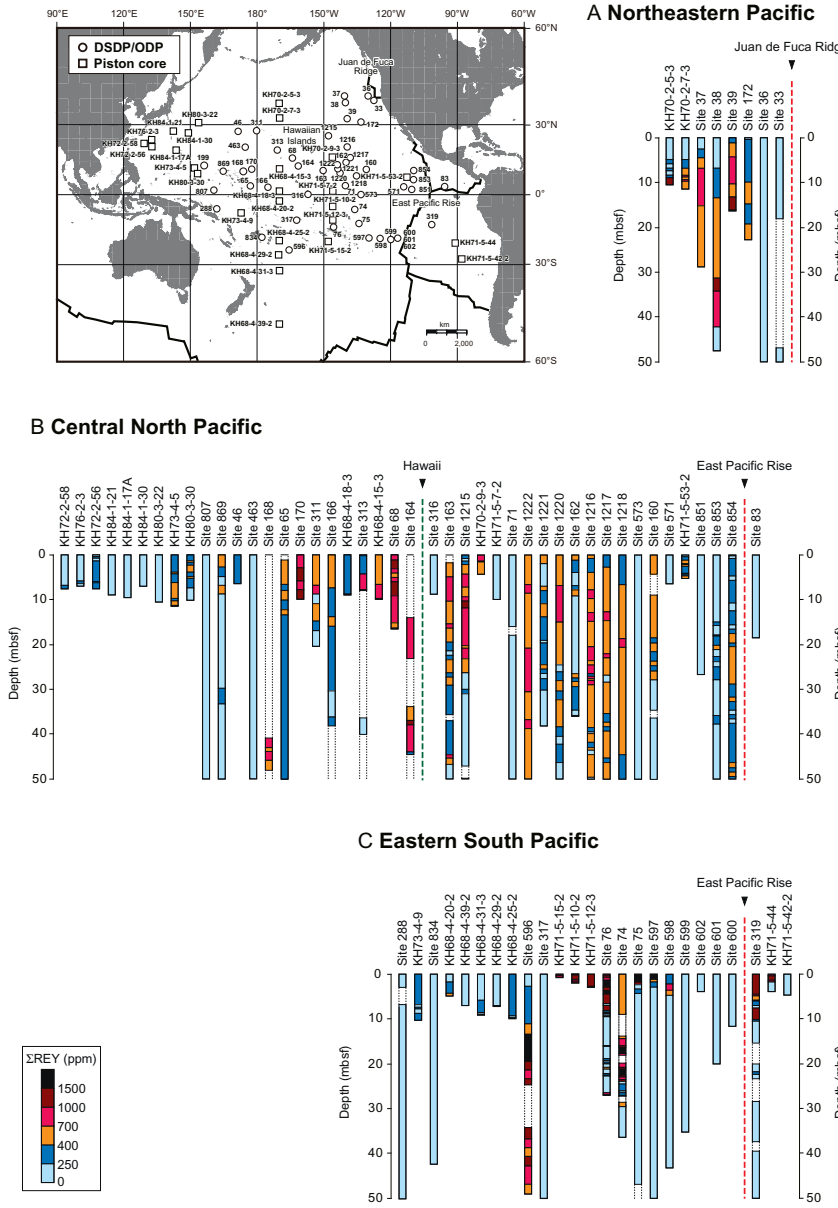

FIGURE 7 Depth profiles of ΣREY content in cores from the Pacific Ocean. Profiles extend to a maximum of 50 mbsf. *Modified from Kato et al. (2011).*

exceed 1500 ppm at some sites (e.g., Sites 75 and 597). On the other hand, at other sites (e.g., Sites 76 and 319) REY-rich muds are relatively thick (~10 m) with average ΣREY contents of ~1000 ppm (Figs. 7 and 8). Interestingly, a thick REY-rich mud layer (~40 m) with average ΣREY content of

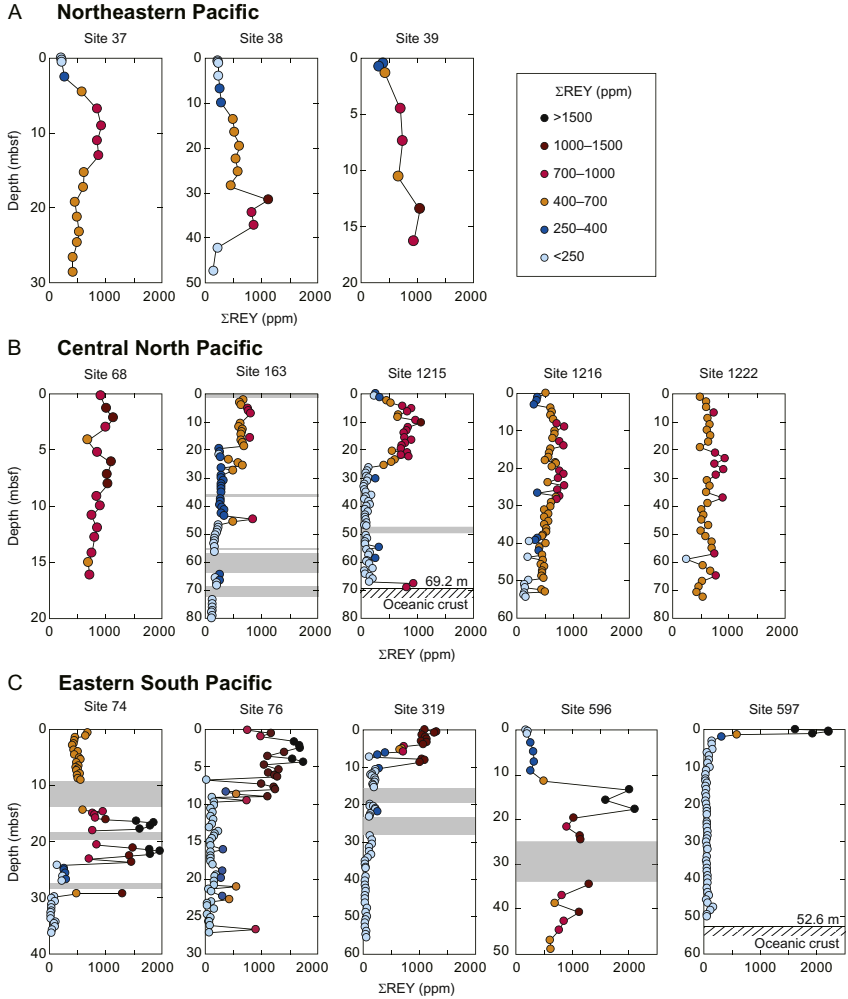

FIGURE 8 Detailed depth profiles of ΣREY content for selected cores from those shown in Fig. 7. Intervals shaded pale gray indicate no core recovery. *Modified from Kato et al. (2011).*

1100 ppm was found 13.5 m below the seafloor at Site 596, even though the surface sediments there have low ΣREY contents of less than 250 ppm (Figs. 7 and 8).

In the central North Pacific region, REY-rich mud layers are much thicker (mostly greater than 30 m, locally over 70 m) than in the eastern South Pacific. ΣREY contents are moderately high (400–1000 ppm) with ΣHREE contents of 70–180 ppm. Especially east of the Hawaiian Islands, layers of REY-rich mud are noticeably thick (mostly over 30 m and locally in excess of 70 m) (Figs. 7 and 8). The average ΣREY contents of the thick REY-rich

muds are 625 ppm which are lower than those of the eastern South Pacific muds. Some cores from west of the Hawaiian Islands have higher ΣREY contents (up to 1130 ppm) than those east of the islands, whereas the REY-enriched layers are thinner (mostly under 20 m).

Apart from these two main regions, REY-rich muds are also found in the northeastern Pacific (west of the Juan de Fuca Ridge) (Figs. 7 and 8). Here, REY-rich muds at several sites (e.g., Sites 37, 38, and 39) are 10–20 m below the seafloor, as is the case for Site 596 in the eastern South Pacific. ΣREY contents of muds in the northeastern Pacific are generally comparable to those of muds in the central North Pacific, with thicknesses of 5–30 m. Even though the surface muds there have low ΣREY contents (Figs. 7 and 8), this type of shallow subseafloor REY-rich mud might also be a suitable REY resource.

2.2 Indian Ocean

Yasukawa et al. (2014) reported a 50-m REY-rich mud layer at DSDP Site 213 in the Wharton Basin, eastern Indian Ocean (Fig. 6). The muds there are 70–120 m below the seafloor and have moderate average ΣREY contents of 630 ppm (maximum content of 1100 ppm). ΣREY contents and thickness of the Indian Ocean REY-rich mud are generally comparable to those in the central North Pacific, although they are considerably deeper below the seafloor.

The existence of REY-rich muds in other regions of the Indian Ocean is also suggested by previously published data (Fig. 6 and Table 2). Bulk-sediment analyses of the uppermost sediments of the Wharton Basin, reported by Pattan et al. (1995), identified a red clay sample with remarkably high total REE content (749 ppm), despite a lack of data on Pr, Tb, and Tm contents. Taking into account their yttrium content datum (386 ppm) and inferred concentrations of Pr, Tb, and Tm, the ΣREY content of the red clay is up to 1190 ppm (Fig. 6 and Table 2). Pattan and Parthiban (2011) also reported chemical compositions of sediment samples from the Central Indian Ocean Basin. On the basis of calculated Pr, Tb, and Tm concentrations (lacking in their data set), the ΣREY content of one red clay sample (SS-210; Fig. 6 and Table 2) is estimated to be 786 ppm.

Compared to the Pacific Ocean, however, information about the distribution of such high ΣREY muds in the Indian Ocean is sparse. More detailed investigations are needed for evaluation of the resource potential of the REY-rich muds in the Indian Ocean.

2.3 Atlantic Ocean

Previous studies have reported REE contents of deep-sea mud in the Atlantic Ocean. However, almost all REE contents reported to date are less than 400 ppm (our criterion for definition of REY-rich mud). For example,

Dubinin and Rozanov (2001) examined REE contents of deep-sea sediments on an east–west traverse across the Mid-Atlantic Ridge at about Lat. 22°N (Fig. 6 and Table 2), but reported no mud with ΣREY >400 ppm. Dubinin et al. (2013) reported a maximum ΣREY content of 379 ppm (average 115 ppm) for deep-sea mud from Station 2182 in the Angola Basin (Fig. 6 and Table 2). Dubinin and Rimskaya-Korsakova (2011) reported deep-sea sediments with relatively high ΣREY contents from the Brazil Basin (Fig. 6 and Table 2). Their data indicate that some of the surface muds on the floor of the basin have ΣREY contents of up to 600 ppm.

3 LITHOLOGICAL AND GEOCHEMICAL CHARACTERISTICS OF REY-RICH MUDS

REY-rich muds are dark-brown pelagic clays (Fig. 9) characterized by low contents of terrigenous detrital materials, biogenous silica, and carbonates. Major constituents are phillipsite (a zeolite mineral found in pelagic areas with low sedimentation rates), clay minerals (e.g., illite), Fe-oxyhydroxides (e.g., goethite), and calcium phosphates (e.g., apatite) (Fig. 10), although the proportions of these minerals vary considerably.

The muds are greatly enriched in REY (an order of magnitude higher than the average composition of upper continental crust), although Ce contents are considerably lower than other REY elements (Fig. 11). These REY patterns suggest that REY in the mud are adsorbed from seawater, which has a similar

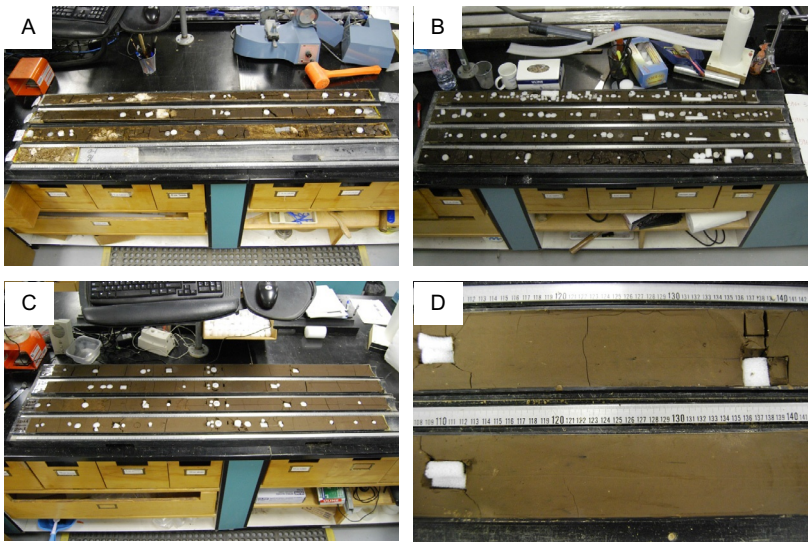

FIGURE 9 Photographs of REY-rich muds in DSDP/ODP cores. (A) Site 76, (B) Site 596, (C) Site 1216, and (D) close-up of Site 1216 core.

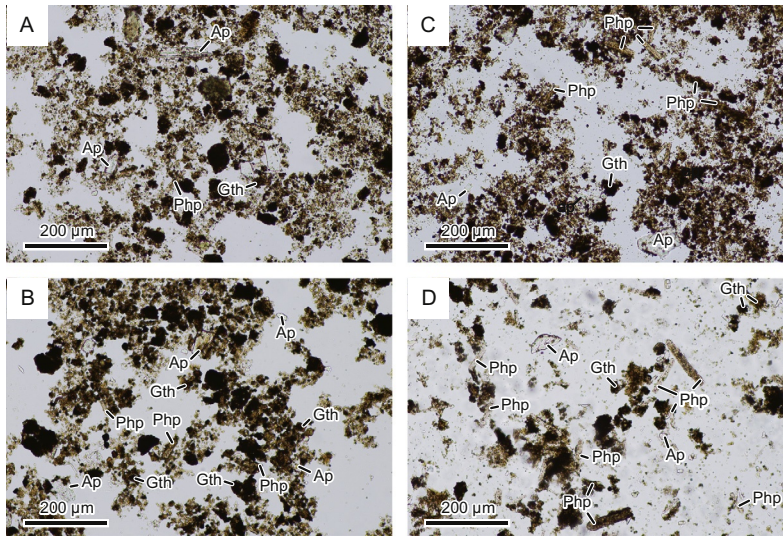

FIGURE 10 Photomicrographs of samples from (A) DSDP Site 76, Core 1, Section 3, 132–134 cm, ΣREY = 1744 ppm, (B) DSDP Site 319, Core 1, Section 1, 55–57 cm, ΣREY = 1312 ppm, (C) DSDP Site 597A, Core 1, Section 1, 64–66 cm, ΣREY = 2228 ppm, and (D) ODP Site 1215A, Core 2, Section 7, 49–51 cm, ΣREY = 1079 ppm. Abbreviations: Ap, apatite; Gth, goethite; Php, phillipsite.

REE pattern (Fig. 11). In Fig. 12 showing correlations of ΣREY contents with concentrations of other elements in REY-rich mud, a clear positive correlation between ΣREY and P_2O_5 contents is recognizable. In addition, strong positive correlations between P_2O_5 and CaO contents and ΣREY and CaO contents are also evident in REY-rich muds (Fig. 12). The relationships among ΣREY, CaO, and P_2O_5 suggest the possible involvement of Ca-phosphate minerals in the formation of REY-rich mud. ΣREY contents of REY-rich muds also correlate positively with MnO and Fe_2O_3 contents (Fig. 12), suggesting that Fe- and Mn-bearing phases also contribute to the formation of REY-rich muds.

4 HOST MINERAL OF REY IN REY-RICH MUD

Very recently, Kashiwabara et al. (2014) used X-ray absorption fine structure (XAFS) and micro-focused X-ray fluorescence (μ-XRF) to analyze La in REY-rich mud sampled from DSDP Site 597 in the eastern Pacific Ocean. They showed that La in REY-rich mud is accumulated in apatite (a Ca-phosphate mineral). This means that apatite is an important host mineral for La, probably for other rare-earth elements and yttrium in REY-rich mud. Kon et al. (2014) also reported the REY composition of apatite separates from Pacific Ocean REY-rich mud, based on analysis using laser-ablation

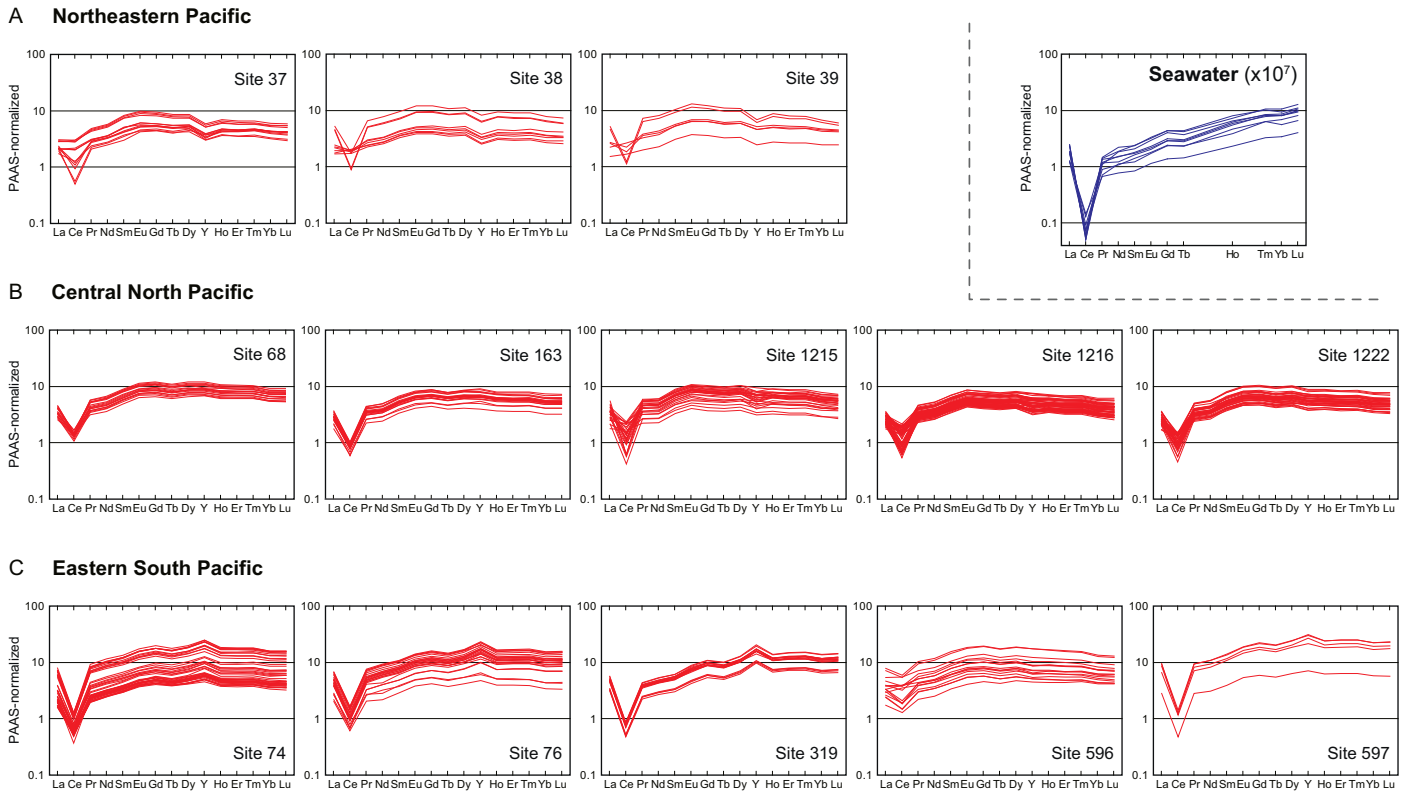

FIGURE 11 Post-Archean average Australian Shale (PAAS) normalized REY patterns of REY-rich muds at same sites as shown in Fig. 8. Normalizing PAAS values are from Taylor and McLenann (1985). Normalized REE pattern for seawater is also shown. Data sources: REY-rich muds, Kato et al. (2011); seawater, de Baar et al. (1985).

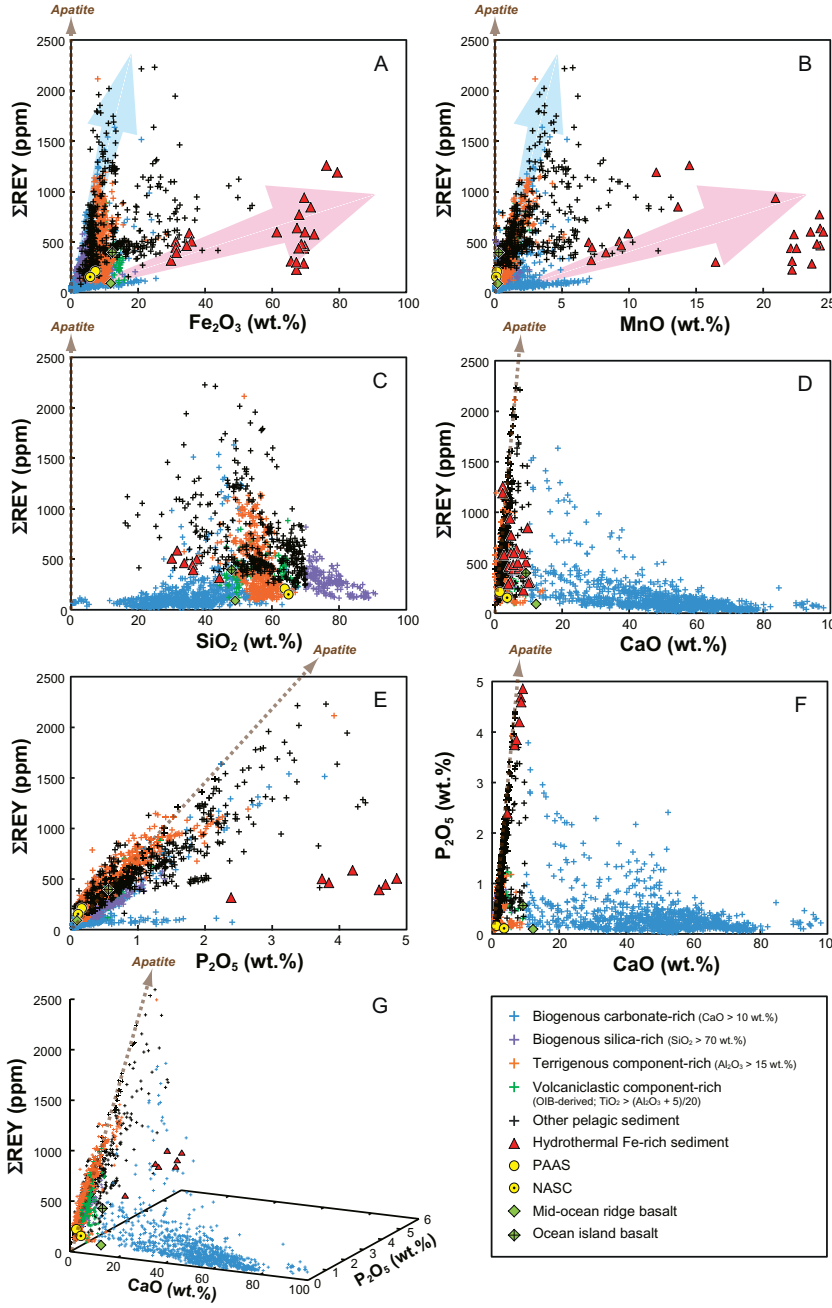

FIGURE 12 ΣREY versus (A) Fe_2O_3, (B) MnO, (C) SiO_2, (D) CaO, (E) P_2O_5, (F) P_2O_5 versus CaO, and (G) three-dimensional plot of ΣREY, CaO, and P_2O_5 for all deep-sea sediment data compiled from the Pacific, Atlantic, and Indian Oceans for this study (Table 2). Data points are

(*Continued*)

inductively coupled plasma mass spectrometer. Their results also demonstrated that a significant part of REY in REY-rich mud is hosted by apatite (Kon et al., 2014).

For bulk chemical compositions of the Indian Ocean REY-rich mud, Yasukawa et al. (2014) found a strong positive correlation between CaO and P_2O_5 and pointed out that CaO/P_2O_5 ratios of REY-rich muds are close to the stoichiometric composition of hydroxyapatite (Fig. 13). Based on this result, Yasukawa et al. (2014) interpreted that apatite is a major host mineral of REY in the Indian Ocean REY-rich mud. Moreover, they reported the presence of irregularly curved apatite crystals in the REY-rich mud (Fig. 14A and B). These crystals showed no peaks on X-ray diffraction analyses, indicating an amorphous or low crystallinity habit (Fig. 15). These observations led them to consider that the apatite minerals presented in REY-rich mud are of biogenic origin.

It should be, however, noted that, as shown in Fig. 12, ΣREY contents of REY-rich mud correlate with not only CaO and P_2O_5 but also other elements that are not present in apatite (e.g., Fe_2O_3 and MnO). This clearly indicates that REY-rich mud cannot be formed by a simple mixing of REY-enriched apatite with other components (i.e., terrigenous, biogenic, and hydrothermal components), even though the present host mineral of REY is apatite. This has been previously pointed out by Kato et al. (2011). They applied independent component analysis (ICA) to the whole data set of bulk-sediment composition and demonstrated that there is no appreciable trend that consistently extends toward an apatite composition in multielement space, including SiO_2, Al_2O_3, TiO_2, Fe_2O_3, CaO, P_2O_5, and ΣREY. These facts lead us to consider a possibility that the REY hosted by apatite in the present REY-rich mud were originally brought by other components and then redistributed onto apatite after deposition.

5 GENESIS OF REY-RICH MUDS

Kato et al. (2011) noted the correspondence of the distributions of REY-rich muds and helium-3 anomalies (δ^3He) in mid-depth (~2500 m water depth) seawater (Fig. 6). Because δ^3He is used as an index of propagation of hydrothermal plumes along mid-ocean ridges (MORs) (Lupton, 1995, 1998; Rüth et al., 2000; Srinivasan et al., 2004; Wu et al., 2011), this correspondence

FIGURE 12—Cont'd colored according to their dominant components by applying the criteria of Kato et al. (2011). Pink (light gray in the print version) and light blue (dark gray in the print version) arrows in (A) represent "Fe-rich" and a "low-Fe" trends, respectively. Data sources for end-members as follows. Hydrothermal Fe-rich sediment from Jarvis (1985), Barrett et al. (1987), and Barrett and Jarvis (1988); PAAS from Taylor and McLenann (1985); NASC (North American shale composite) from Gromet et al. (1984) and Goldstein and Jacobsen (1988); MORB (mid-ocean ridge basalt) from Floyd and Castillo (1992); and OIB (ocean island basalt) from Christie et al. (1995).

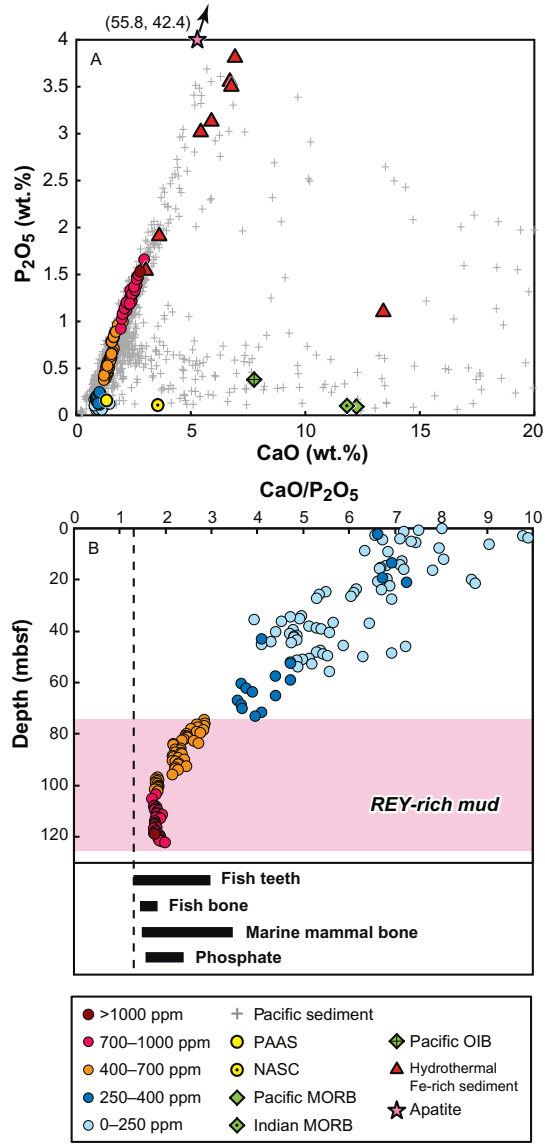

FIGURE 13 (A) CaO versus P_2O_5 for Pacific deep-sea sediments (gray crosses; Kato et al., 2011) and for DSDP Site 213 sediments (filled circles, the color-coding is the same as in Fig. 8; Yasukawa et al., 2014). Representative composition of apatite calculated on the basis of the formula $Ca_5(PO_4)_3(OH)$ (i.e., hydroxyapatite) is also shown. (B) Depth profile of CaO/P_2O_5 ratios at Site 213. Horizontal black bars represent ranges of CaO/P_2O_5 ratios for biogenic apatites and phosphatized materials from the floors of the Atlantic and Pacific Oceans (Nemliher et al., 2004). Vertical dashed line indicates the CaO/P_2O_5 ratio based on the stoichiometric composition of apatite. Horizontal pink (gray in the print version) bar represents the REY-rich mud layer at Site 213. *Both (A) and (B) are modified from Yasukawa et al. (2014).*

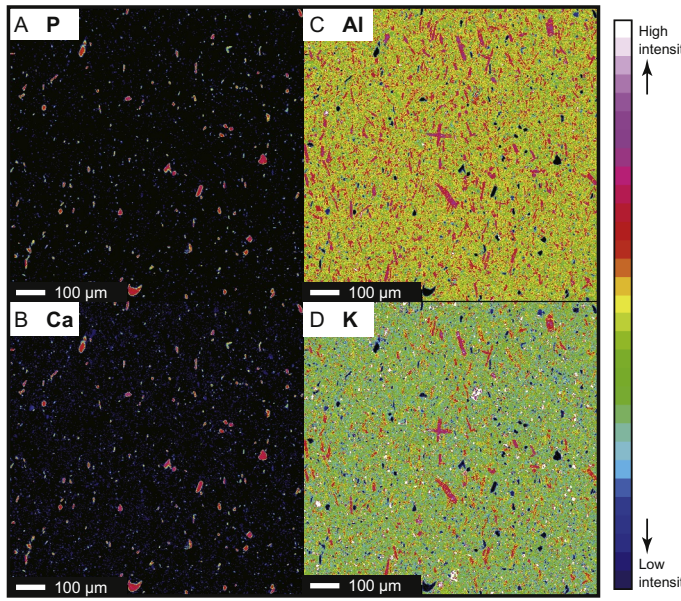

FIGURE 14 EPMA element maps of a polished thin section of Indian Ocean REY-rich mud from DSDP Site 213 for (A) P, (B) Ca, (C) Al, and (D) K. High-intensity areas (mostly red (light gray in the print version) in color) for P and Ca (A, B) and Al and K (C, D) represent irregularly shaped biogenic apatite and euhedral phillipsite crystals, respectively. *Modified from Yasukawa et al. (2014).*

strongly suggests that hydrothermal activity at MORs plays some role in the formation of REY-rich muds. It is well known that the East Pacific Rise (EPR) is a fast-spreading MOR (Müller et al., 2008) accompanied by intense hydrothermal activity due to high rates of magma production (Baker et al., 1995; Lupton, 1995, 1998; Shinha and Evans, 2004). Thus, it is reasonable to suggest that hydrothermal plumes containing considerable amounts of Fe/Mn-oxyhydroxides have formed at hydrothermal vents on the EPR and spread westward precipitating Fe-oxyhydroxides with REY adsorbed from seawater onto the seafloor (Kato et al., 2011). Positive correlations between ΣREY and both MnO and Fe_2O_3 contents in REY-rich muds (Fig. 12) support this interpretation.

In contrast to the remarkably high δ^3He values of Pacific Ocean seawater, those of the Indian Ocean are moderate (Lupton, 1995; Srinivasan et al., 2004) and those of the Atlantic Ocean are lower still (Fig. 6) (Lupton, 1995; Rüth et al., 2000). Assuming that the formation of REY-rich muds is correlated with δ^3He values of mid-depth seawater (reflecting the distribution of hydrothermal plumes emanating from MORs), a limited distribution of REY-rich muds in the Indian and Atlantic Oceans seems likely.

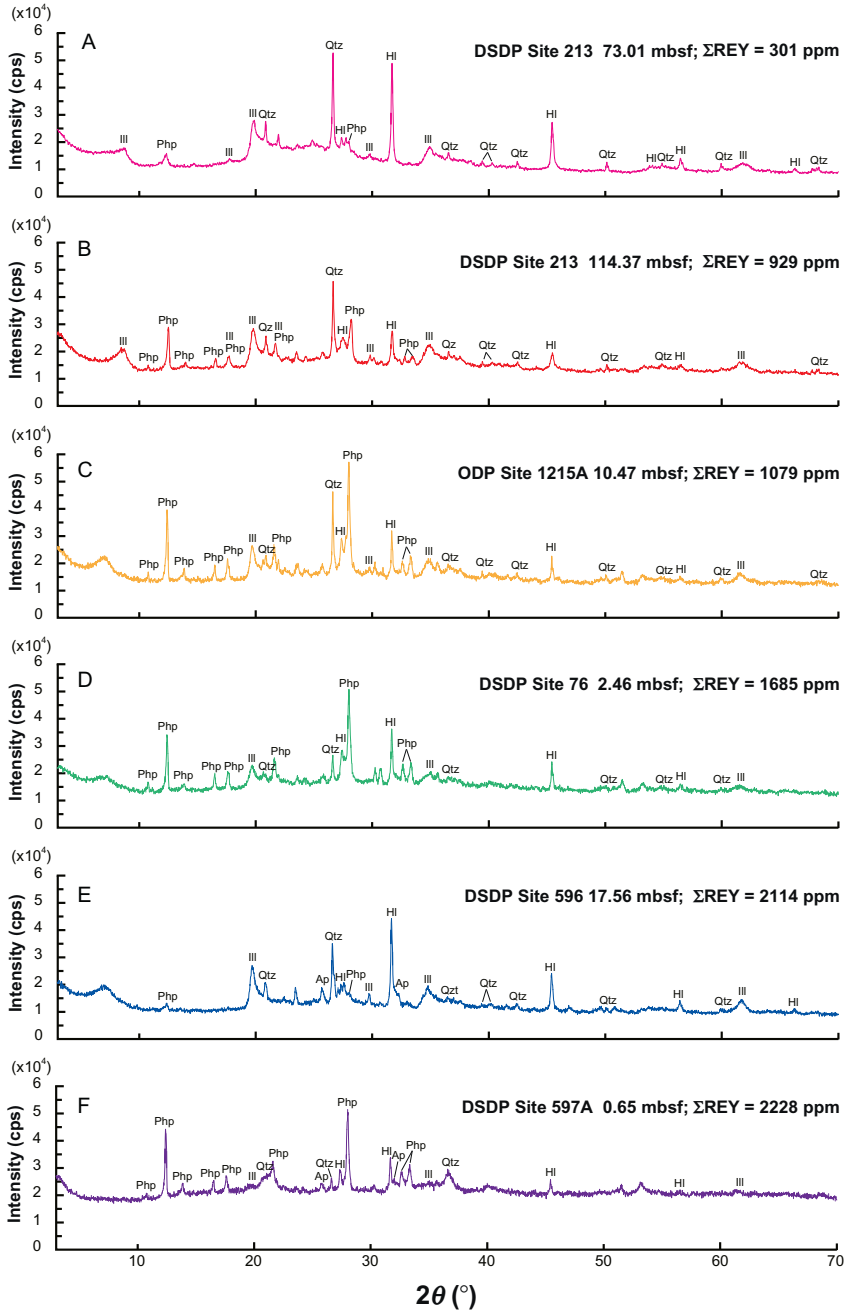

FIGURE 15 X-ray diffractograms for bulk-sediment samples from the Pacific and Indian Oceans. (A) DSDP Site 213 (eastern Indian Ocean), (B) DSDP Site 213, (C) ODP Site 1215A (central North Pacific), (D) DSDP Site 76 (eastern South Pacific), (E) DSDP Site 596 (central South Pacific), and (F) DSDP Site 597A (eastern South Pacific). Abbreviations: Ap, apatite; Hl, halite; Ill, illite; Php, phillipsite; Qtz, quartz.

Kato et al. (2011) also pointed out that, in addition to Fe- and Mn-oxyhydroxides, phillipsite plays an important role in REY enrichment of REY-rich muds based on bulk-rock chemical composition of the latter. Indeed, elemental mapping (Fig. 14C and D) and X-ray diffraction patterns (Fig. 15) show the presence of phillipsite in REY-rich muds. Detailed descriptions of phillipsite in REY-rich muds from the Southern Basin of the Pacific Ocean suggest that phillipsite commonly occurs in aggregates along with bone detritus (biogenic apatite), Fe-oxyhydroxides, and Fe-Ca-hydroxophosphates (Dubinin, 2000). Dubinin (2000) pointed out that the phillipsite itself is not the main host of REY; rather, pseudorhombic phillipsite aggregated with REY-containing concomitants (including biogenic apatite, Fe-oxyhydroxide, and Fe-Ca-hydroxophosphates) is responsible for the high ΣREY values. This observation may be consistent with the positive correlations between ΣREY and Fe_2O_3 and MnO, as well as the amount of phillipsite in REY-rich muds (Fig. 12).

Kato et al. (2011) also showed that concentrations of REY in deep-sea mud are negatively correlated with sedimentation rate. In particular, REY-rich muds with high concentrations of REY ($\Sigma REY > 1000$ ppm) exhibit extremely low sedimentation rates, less than 0.1 cm/kyr. Kato et al. (2011) pointed out that dilution by biogenic $CaCO_3$ and SiO_2 has a critical influence on the ΣREY values of deep-sea muds, based on negative correlations of ΣREY with both CaO and SiO_2 in Pacific Ocean deep-sea muds. Indeed, in pelagic environments, the sedimentation rate of biogenic components is much higher than that of other components (Hüneke and Henrich, 2011; Wheeler and Stadnitskaia, 2011). Sedimentation rates of biogenic $CaCO_3$ and SiO_2 are, in turn, controlled by carbonate compensation depth (CCD) and silica compensation depth (SCD), defined as the water depths at which carbonate and silica dissolution rates become equal to their precipitation rates. CCD and SCD are controlled by multiple factors such as hydrostatic pressure, water temperature, degree of undersaturation of deep-water masses, and bioproductivity in surface ocean waters. Shallow seafloors at depths above the CCD and SCD, and/or high bioproductivity in surface waters, therefore, result in the accumulation of biogenic components on the seafloor, thus leading to dilution of the REY-rich component of sediments. This explains the absence of REY-rich mud near the EPR (relatively shallow depth) and in the equatorial Pacific (high bioproductivity) (Fig. 16). CCD varies among ocean basins and is generally deeper in the Atlantic and Indian oceans than in the Pacific (van Andel, 1975; Wheeler and Stadnitskaia, 2011). Thus, the Pacific Ocean is more amenable to the formation of extensive areas of REY-rich mud in areas where the seafloor is deeper than the CCD. On the other hand, although the difference of SCDs among ocean basins is not fully understood, deposition of biogenic silica is generally greater in areas of high bioproductivity, such as the equatorial Pacific and Southern Oceans (Heezen et al., 1973; Hüneke and Henrich, 2011).

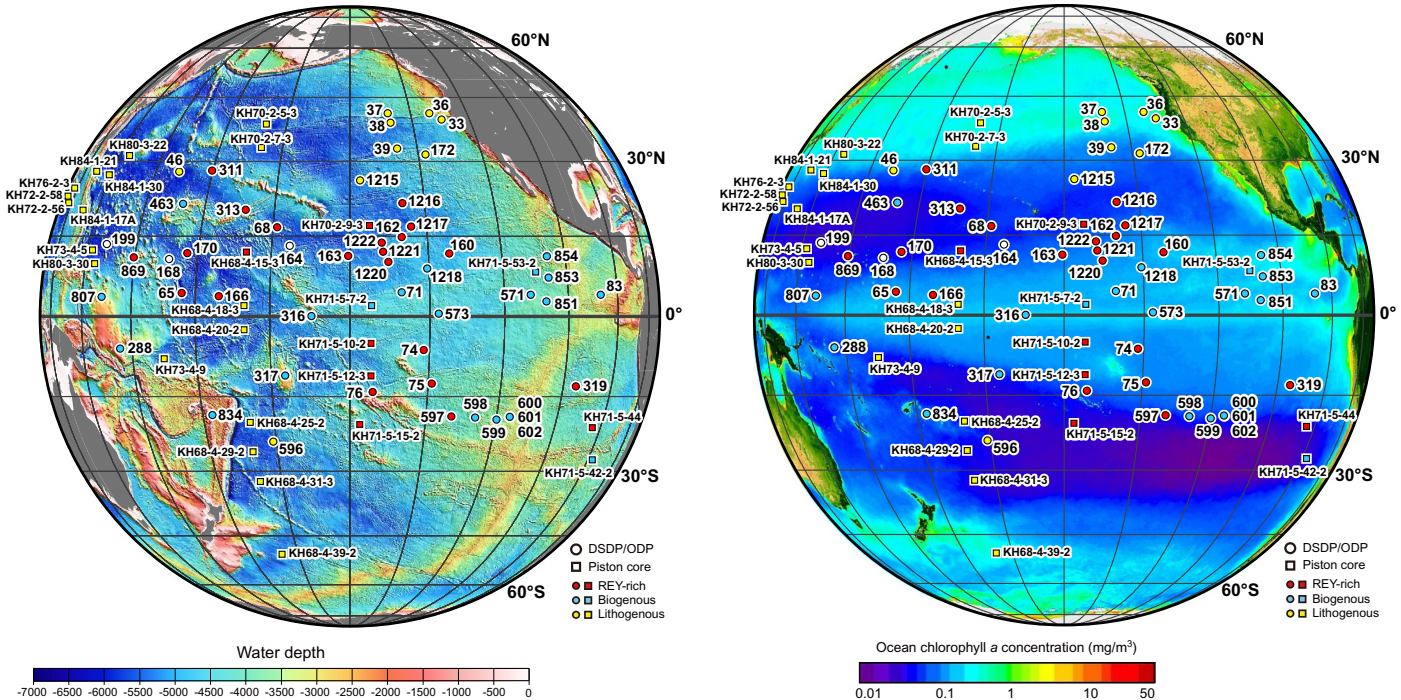

FIGURE 16 Sample sites in the Pacific Ocean showing major components of seafloor muds with (A) bathymetry and (B) sea-surface chlorophyll *a* concentrations (courtesy of SeaWiFS Project, NASA/Goddard Space Flight Center, and ORBIMAGE). Bathymetry is based on 2-min-gridded global relief data (ETOPOv2; National Geophysical Data Center, 2006; http:/www.ngdc.noaa.gov/mgg/fliers/06mgg01.html).

6 RESOURCE POTENTIAL AND ADVANTAGES OF DEVELOPING REY-RICH MUD DEPOSITS

REY-rich muds have five advantages as a mineral resource: (1) tremendous resource potential because of their extensive distribution, (2) high REY concentrations with HREE enrichment, (3) ease of exploration, (4) low radioactive element concentrations, and (5) high and easy recovery of REY by acid leaching. In this section, we describe these favorable properties of REY-rich muds by comparing them with onshore REY deposits.

6.1 Tremendous Resource Potential

Kato et al. (2011) made estimates of the resource potential of REY-rich muds at DSDP Site 76 in the eastern South Pacific and ODP Site 1222 in the central North Pacific. At DSDP Site 76 (average ΣREY content of 1180 ppm and dry bulk density of 0.66 g/cm^3), a 10-m-thick bed of REY-rich mud in an area of just 1 km^2 contains roughly 9000 metric tons of REY-oxides (tREY-oxides), which, assuming a complete recovery of the rare earths from the mud, is about one-twelfth of global annual onshore production of REY in 2012 (1.1×10^8 metric tons of REY-oxides; USGS, 2013). At ODP Site 1222 (average ΣREY content of 640 ppm and dry bulk density of 0.477 g/cm^3), a 70-m-thick bed of REY-rich mud in an area of 1 km^2 contains approximately 25,000 tREY-oxides, which is comparable to one-fourth of the 2012 global annual onshore production (USGS, 2013). The estimates indicate that production of REY from ~12 km^2 (about 3.5 km × 3.5 km) at Site 76, or from ~4 km^2 (about 2.1 km × 2.1 km) at Site 1222, would be comparable to current global annual REY production from onshore deposits.

Considering pelagic, deep-sea depositional environments (Lyle et al., 2010; Tracey et al., 1971), REY-rich mud is likely to be distributed over much greater areas than used in the estimates by Kato et al. (2011). Assuming, for example, that deposits at these two sites each cover an area of 10,000 km^2 (100 km × 100 km), the resource potential is far greater. If this were the case, a 10-m-thick layer of REY-rich mud similar to that at Site 76 and a 70-m-thick layer of mud similar to that at Site 1222 might be expected to produce 0.9×10^8 and 2.5×10^8 tREY-oxides, respectively. Both of them are equivalent to or greater than known global reserves onshore (1.1×10^8 tREY-oxides; USGS, 2013). Taking into consideration the large distribution areas of REY-rich muds in the eastern South Pacific and central North Pacific, these are indeed enormous resources that by two to three orders of magnitude exceed the known global reserves onshore. However, further core sampling and geochemical analysis at much higher spatial resolution are needed before a more extensive and precise evaluation of the resource potential can be made.

6.2 High REY Concentrations with HREE Enrichment

REY concentrations in Southeast Pacific REY-rich muds commonly exceed 1000 ppm (Kato et al., 2011), two to three times higher than those of ion-adsorption-type REY deposits in southern China (Fig. 17). More importantly, the Pacific Ocean muds are highly enriched in HREE (e.g., Eu, Dy, and Tb) (Figs. 5 and 17). In contrast, most onshore REE deposits (including the Bayan-Obo deposit in China and the Mountain Pass deposit in the USA, which are the main global sources of LREE) are extremely enriched in LREE (Fig. 18). These deposits are hosted primarily by carbonatite and alkaline igneous rocks (Castor and Hedrick, 2006). During genesis of the magma that produces these rocks, LREE are preferentially partitioned into magma, resulting in strong LREE-enrichment (Castor and Hedrick, 2006).

In contrast, there are only a few HREE deposits in the world. To date, only ion-adsorption-type deposits in southern China have been recognized as commercially viable HREE deposits (Bao and Zhao, 2008; Wu et al., 1990, 1996). These are formed during weathering of igneous rocks by leaching REY and partitioning them into clay minerals in soils. In this aqueous process, REY are leached from the host rocks with a relatively equal proportion of HREE to LREE and partitioned into clay minerals, resulting in enrichment by both LREE and HREE. This is quite different from the preferential enrichment by LREE occurs during magmatic processes (Castor and Hedrick, 2006). Ion-adsorption-type deposits have been developed only in southern China, and the resources they contain are small. Therefore, REY-rich deep-sea muds with high concentrations of HREE have a remarkable potential as a new source of HREE.

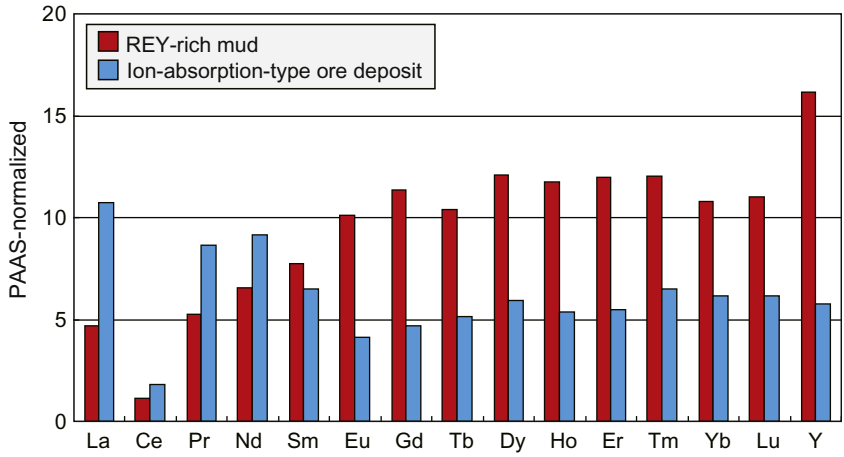

FIGURE 17 Comparison of average REY concentrations of REY-rich muds (Kato et al., 2011) and ion-adsorption-type ore deposits (Bao and Zhao, 2008).

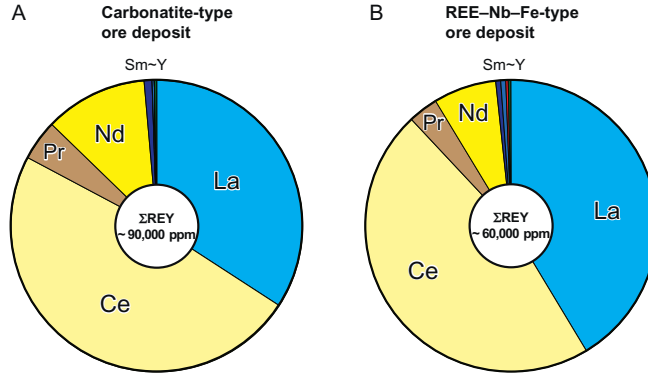

FIGURE 18 REY contents of LREE ore deposits. (A) Carbonatite-type ore deposit (Murakami and Ishihara, 2006) and (B) REE–Nb–Fe-type ore deposit (Yang et al., 2009).

6.3 Ease of Exploration

REY-rich muds are typically found as layered pelagic sediments that are uniformly distributed over extensive areas in the Pacific Ocean. It is commonly believed that pelagic deep-sea muds of relatively homogeneous lithology cover large areas of the Pacific Ocean seafloor, perhaps more than 10,000 km^2 (100 km $\times$ 100 km) (Lyle et al., 2010; Tracey et al., 1971). If this is the case for pelagic REY-rich muds, the distribution of REY-rich muds can be easily estimated from the results of relatively sparse sediment coring at intervals as wide as several tens of kilometers. Such an easy exploration for pelagic deep-sea REY-rich muds has a distinct economic advantage over exploration for other deep-sea mineral resources and many onshore mineral resources.

6.4 Low Radioactive Element Concentrations

Most onshore REY deposits have high concentrations of radioactive elements such as U and Th (Fig. 19) (e.g., Murakami and Ishihara, 2006; Sørensen et al., 2011; Yang et al., 2009) that are attributed to the behavior of U and Th as incompatible elements during magma genesis, similar to the behavior of LREE. Therefore, production of REY from onshore LREE deposits (e.g., carbonatite and alkaline basalt-type deposits) produces massive amounts of radioactive waste, which is a serious and persistent environmental problem in REY mining.

Concentrations of these radioactive elements in REY-rich muds are strikingly lower. At concentrations of only $\sim$10 ppm of Th and U (combined) as compared to 1000 ppm of REY, they are one to two orders of magnitude lower than that in onshore REY deposits and equal to or lower than the crustal abundances of these elements (Fig. 19). Therefore, mining of REY from deep-sea muds would be expected to produce no hazardous radioactive waste.

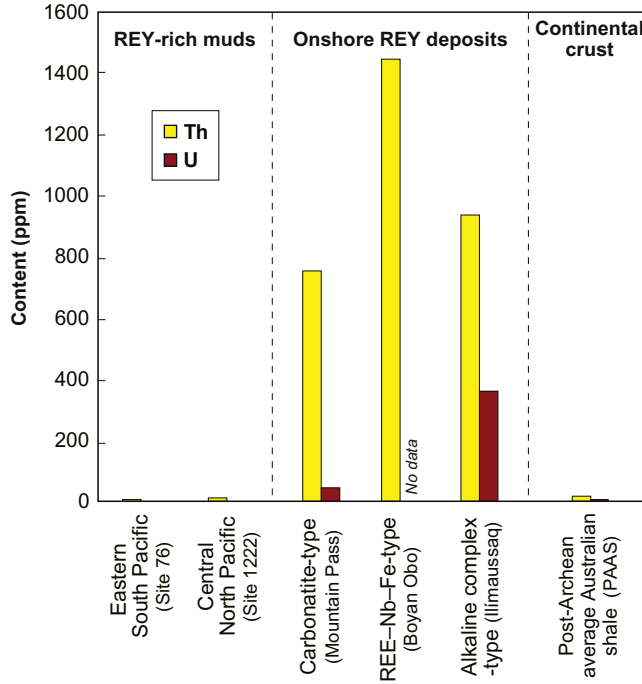

FIGURE 19 Comparison of U and Th contents of REY-rich muds, onshore REY deposits, and continental crust. Data sources: REY-rich muds, Kato et al. (2011); carbonatite-type ore deposit, Murakami and Ishihara (2006); REE–Nb–Fe-type ore deposit, Yang et al. (2009); alkaline complex-type ore deposit, Sørensen et al. (2011); and PAAS, Taylor and McLenann (1985).

6.5 High and Easy Recovery of REY by Acid Leaching

Kato et al. (2011) reported that more than 90% of REY can be quickly and easily leached from deep-sea muds by using dilute hydrochloric acid without heating. Because the leached REY can be refined by using well-established, traditional onshore mining approaches, this clearly demonstrates the potential for low cost and high recovery of REY from REY-rich muds. Details of the acid leaching processes and proposed refining systems for REY-rich muds are presented in Section 7.2.

7 DEVELOPMENT SYSTEMS

7.1 Mining System

Deep-sea mineral resources other than REY-rich muds are known to exist; these include manganese nodules, cobalt-rich ferromanganese crust, and hydrothermal sulfide deposits (Fig. 20). Here, we briefly review the mining systems and concepts for the previously recognized deep-sea mineral

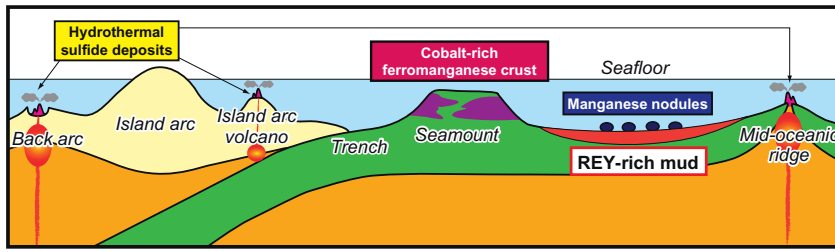

	Hydrothermal sulfide deposit	Cobalt-rich ferromanganese crust	Manganese nodule	REY-rich mud
Mode of occurrence	Chimney or mound ($10–10^2$ m)	Thin coating (0.1–10 cm)	Spherical (2.5–25 cm)	Bedded (2–70 m)
Amount	$10^4–10^6$ t (one site)	5×10^{10} t	5×10^{11} t	$>1 \times 10^{14}$ t

FIGURE 20 Schematic illustration of different types of deep-sea mineral resources.

resources, most of which are developed and tested for mining of manganese nodules.

In the 1970s and 1980s, development and testing of systems for mining manganese nodules were undertaken by four international consortia made up of companies from the United States, Canada, United Kingdom, Federal Republic of Germany, Belgium, the Netherlands, Italy, France, and Japan. Three government-sponsored entities from the Union of Soviet Socialist Republics, India, and China also developed and tested systems for mining manganese nodules. The basic elements of these systems are a propelled or towed nodule collector and a lifting system (Fig. 21) (ISA Technology Brochure, http://www.isa.org.jm/en/documents/technical/ENG7.pdf). Nodules are collected from the ocean floor and crushed to make a seawater slurry which is then pumped to the surface through a riser pipe. Both pump-lift and air-lift systems have been developed (Fig. 22).

The pump-lift system employs multistage centrifugal pumps at intervals along the riser and is more energy efficient than the air-lift system described below. However, wearing of impellers and difficulties in pump maintenance are negative features of this system. The air-lift system uses injection of compressed air at bottom and/or intermediate depths to produce three-phase (gas–liquid–solid) upward flow. This simple system is powered only by compressed air without the need for an underwater mechanical pump. However, expansion of the injected air at shallow depths causes excessively high flow velocity and turbulence, resulting in wearing of the riser pipe.

The first test of a mining system was conducted in 1970 by Deepsea Ventures Inc., which used an air-lift system to recover manganese nodules collected from a depth of 1000 m (ISA Technology Brochure, http://www.isa.org.jm/en/documents/technical/ENG7.pdf). Between 1976 and 1978, Ocean

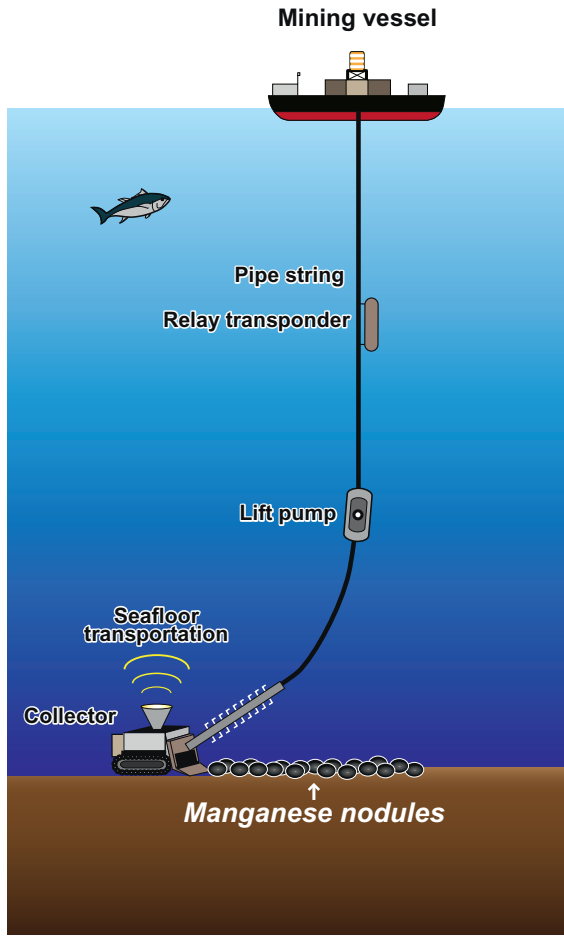

FIGURE 21 System used to mine manganese nodules. *Modified from ISA Technology Brochure, http:/www.isa.org.jm/en/documents/technical/ENG7.pdf.*

Mineral Associates tested an air-lift system with a towed collector and recovered 550 t of manganese nodules during 18 h of operation (ISA Technology Brochure, http:/www.isa.org.jm/en/documents/technical/ENG7.pdf). In 1978, Ocean Mining Inc. performed pre-pilot mining tests for both pump-lift and air-lift systems, during which it recovered 600 t of manganese nodules (ISA Technology Brochure, http:/www.isa.org.jm/en/documents/technical/ENG7.pdf). All of the above tests were conducted over short periods of time and using small-scale experimental or pilot systems, although commercial mining will require the design and operation of mining systems that are at least 10 times larger.

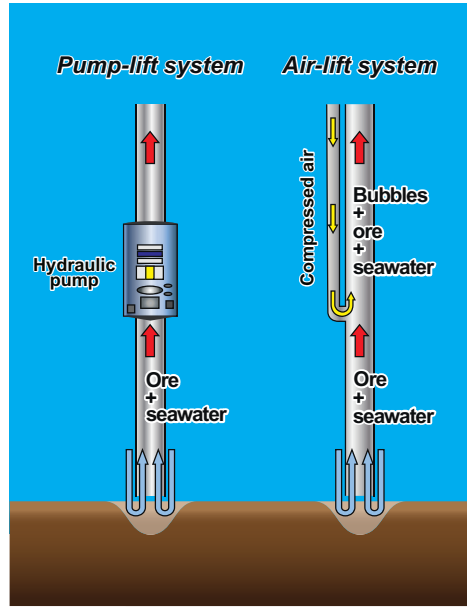

FIGURE 22 Hydraulic pump-lift and air-lift systems.

Other than manganese nodules, deep-sea mining of sulfide-rich muds in the Red Sea at ~2000 m water depth has been tested by Preussag AG, a German mining company (Amann, 1983, 1985). Pre-pilot test mining in 1979 used a hydraulic pump system to raise 15,000 m^3 (2.6 million tons) of mud (Fig. 23) (Amann, 1983, 1985). More recently, Nautilus Minerals Inc. began development of a system to mine seafloor hydrothermal sulfide deposits at the Solwara site in Papua New Guinea (Blackburn and Hanrahan, 2010). The planned system comprises seafloor production tools with a riser and lifting system (Blackburn and Hanrahan, 2010) and is essentially the same as previous systems developed to mine deep-sea manganese nodules and sulfide-rich mud.

It is reasonable to assume that REY-rich muds can be recovered using mining systems similar to those tested for mining of other deep-sea resources; in particular, the system used to mine deep-sea sulfide-rich muds in the Red Sea is a useful reference.

It can be envisioned that a system for mining REY-rich mud will comprise seafloor mud collecting tools, a riser and air-lift system, and a support vessel equipped with facilities for acid leaching and storage (Fig. 24). The air-lift system will have compressed air injected at three or more points (depending on water depth) to lift the slurry of REY-rich mud and seawater to the support vessel. A major difference between deep-sea mining of the sulfide-rich muds and REY-rich muds is water depth (sulfide-rich muds at ~2000 m water depth

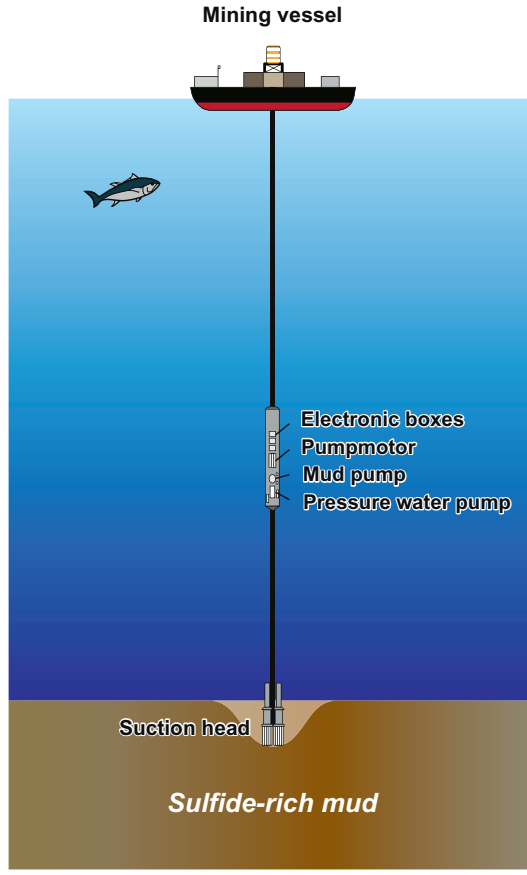

FIGURE 23 System used to mine sulfide-rich muds in the Red Sea. *Modified from Nawab (1984).*

versus REY-rich muds at >4000 m water depth). Some parts of REY-rich muds in the Pacific Ocean are found at water depths of >5000 m. If the air-lift system is used in very deep water (>5000 m), compressed air injected at 5000 m will have expanded 500-fold when it reaches the surface, potentially damaging the riser pipe. Quite recently, a Japanese ocean equipment development company, Mitsui Ocean Development & Engineering Co., Ltd. (MODEC), has proposed a pressurized air-lift system that will overcome such damage to the riser pipe by applying 30 bars of back pressure to the system from the support vessel. This system can reduce expansion of the rising air by a factor of 20, which in turn reduces the danger of damaging the riser pipe significantly.

On the support vessel, the slurry is separated from seawater and transferred to storage tanks. REY is then leached from the mud by using dilute

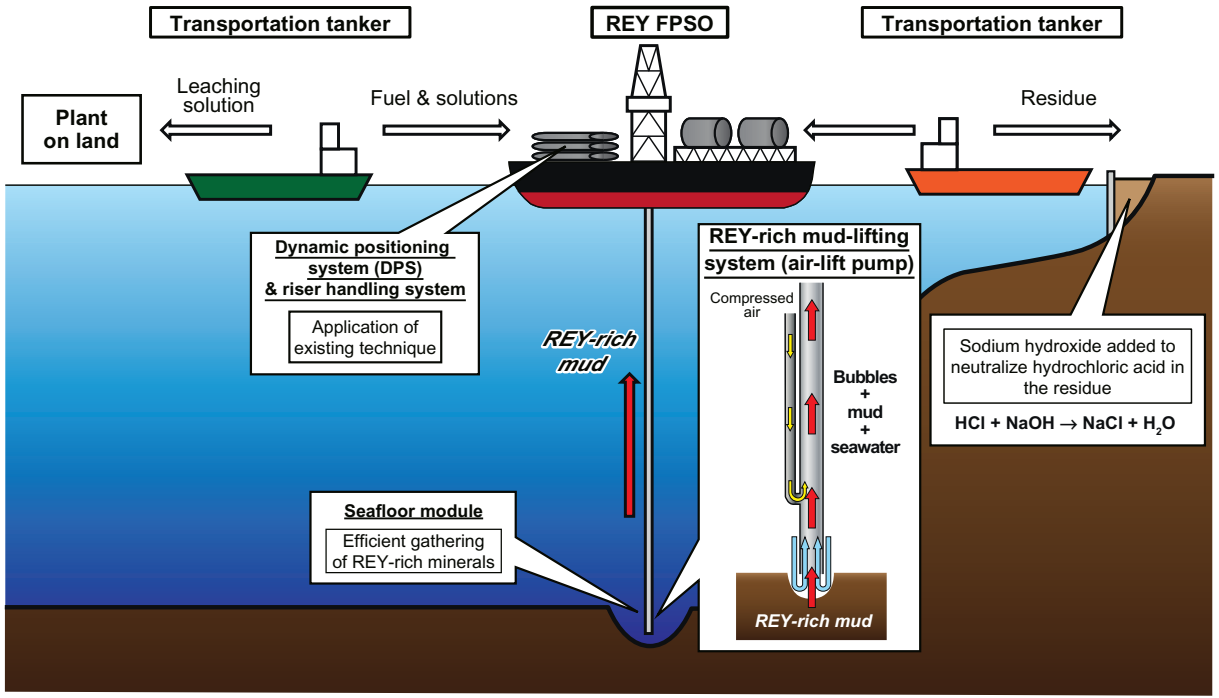

FIGURE 24 Conceptual floating production storage and offloading (FPSO) system for REY-rich mud mining.

hydrochloric acid, either onboard the vessel or onshore (see Section 7.2), before smelting at an onshore plant. Residual mud is detoxified by adding sodium hydroxide and then used for landfill or building material.

7.2 Leaching Systems

Kato et al. (2011) showed that acid leaching is an effective method for extraction of REY from REY-rich mud. In this section, we focus on optimization of this method and discuss its adoption in a future REY production system.

7.2.1 In Situ *Leaching of Chinese REY Ores*

To date, the *in situ* leaching method described below has been used only for ion-adsorption-type REY deposits in China (Schüler et al., 2011). Leaching solution pumped into drill holes flows downward through the ore–soil mixture, collecting REY along the way, until it reaches an underlying aquitard where it flows to the downslope recovery point (Fig. 25). In the Chinese ion-adsorption-type REY deposits, ammonium sulfate is used as the leaching solution (e.g., Xiujuan et al., 2012). *In situ* leaching with ammonium sulfate has been effective for these deposits and has considerable economic advantages over off-site leaching. However, a disadvantage of this method is some unrecoverable losses of leaching solution and residue to the environment, leading to environmental pollution.

7.2.2 *Experimental Acid Leaching of REY-Rich Muds*

We plan to use chemical leaching, either heap leaching (Fig. 26) or leaching in a purpose-built pool, to extract REY from deep-sea muds. As discussed above, Kato et al. (2011) showed acid leaching to be an effective method for extraction of REY from REY-rich muds. They reported recovery rates from REY-rich muds that exceeded 95% (Ce excluded) for 3 h of leaching

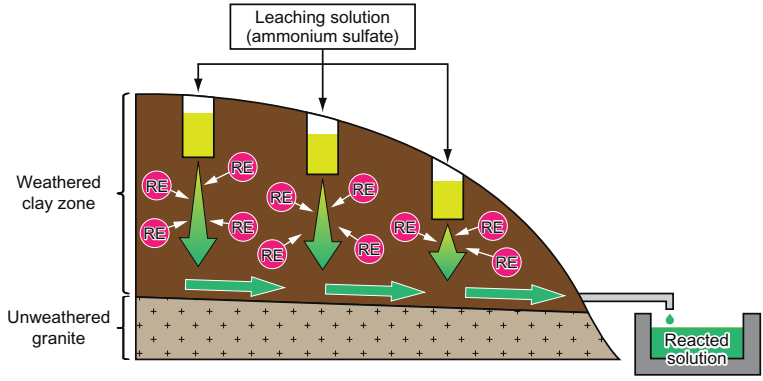

FIGURE 25 Schematic diagram of *in situ* leaching method used for ion-adsorption-type ore deposits in southern China.

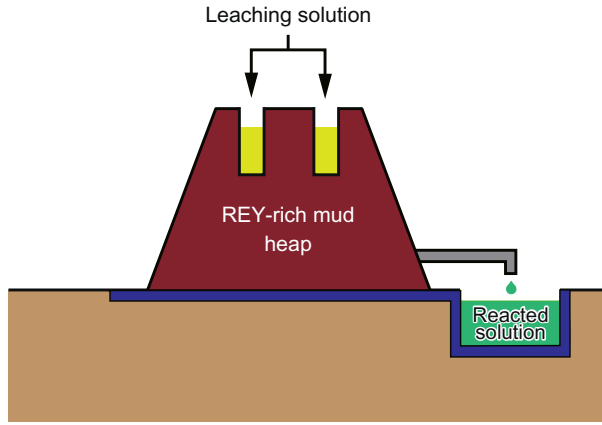

FIGURE 26 Schematic diagram of heap leaching of REY-rich mud.

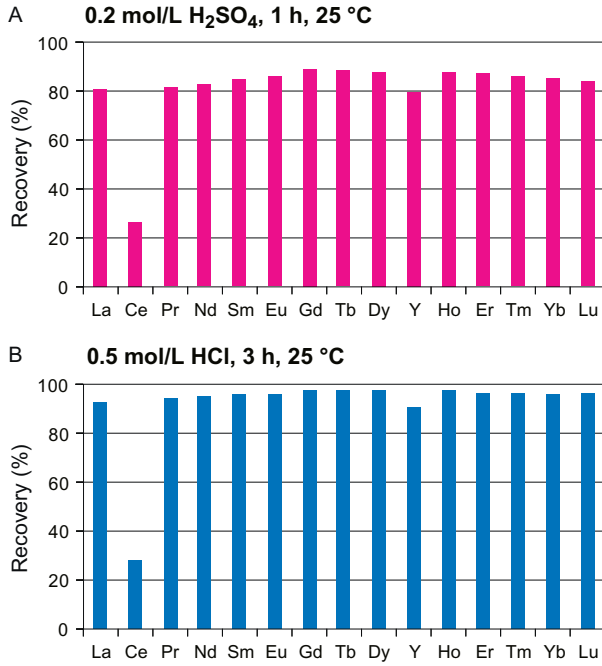

FIGURE 27 Results of experiments on concentrations of diluted leaching reagents (mud from Site 68, Core 1, Section 3, 50–52 cm, ΣREY = 1133 ppm). *Modified from Kato et al. (2011).*

with 0.5 mol/L hydrochloric acid, and 80% for 1 h of leaching with 0.2 mol/L sulfuric acid. A solution-to-mud ratio of 10:1 was used in both cases (Fig. 27). In an attempt to further optimize the leaching process, we experimented by using different reagents (hydrochloric acid, sulfuric acid, nitric acid, sodium

hydroxide, and ammonium sulfate) for various leaching times, temperatures, and reagent concentrations. We used geochemical reference material JMS-2 prepared by the Geological Survey of Japan (Terashima et al., 2002), a REY-rich (916 ppm REY; Takaya et al., 2014) deep-sea mud from the Penrhyn Basin in the South Pacific.

Our experiments showed that strong acids, such as hydrochloric, sulfuric, and nitric acids, are suitable for extraction of REY. Each of these reagents gave recovery rates exceeding 90% in our experiments (Fig. 28). We also demonstrated that ammonium sulfate and sodium hydroxide do not extract REY from REY-rich muds. The failure of ammonium sulfate to extract REY in our experiments clearly indicates that the enrichment mechanism and/or host minerals of REY in REY-rich muds differ from those of Chinese ion-adsorption-type deposits. Our experiments also showed that dilute hydrochloric, sulfuric, and nitric acids were strong enough to effectively leach REY from the mud. Using dilute acid in a production environment will inhibit elution of unwanted elements that would be regarded as impurities during subsequent refining.

Having tested the concentration of acids used as leaching agents, we next considered the time required to extract REY. We achieved similar recovery rates for leaching times ranging from 5 to 60 min (Fig. 29) and concluded that if there is sufficient leaching solution, and the mud and leaching solution mixture is adequately stirred, REY will be extracted into the leaching solution almost instantaneously.

Our tests of temperature dependence of the recovery rate of REY showed, surprisingly, that recovery was higher at room temperature (25 °C) than at higher temperatures (up to 75 °C) (Fig. 30). The decrease of the solubility of apatite (the main host of REY in REY-rich mud) with increasing solution temperature might explain the lower REY recovery rate at higher temperatures. The temperature dependence of the recovery rate for REY indicates that REY can be selectively extracted from mud by controlling the reaction temperature during acid leaching.

7.2.3 Acid Leaching Process for Commercial Production of REY from REY-Rich Mud

In a commercial production system, acid leaching of REY-rich mud can be done either onboard the support vessel or at an onshore facility. In either case, a highly efficient leaching process will be needed to deal with the massive amounts of REY-rich mud mined (estimated to be 10,000 t per day).

We have shown (Section 7.2.2) the advantages of using dilute strong acids (hydrochloric, sulfuric, or nitric acids) to extract REY from REY-rich mud. We favor the use of hydrochloric acid as the leaching solution for a production system. Although sulfuric acid is the cheapest of the three acids we considered, the process of detoxification and removal of sulfuric acid and sulfate

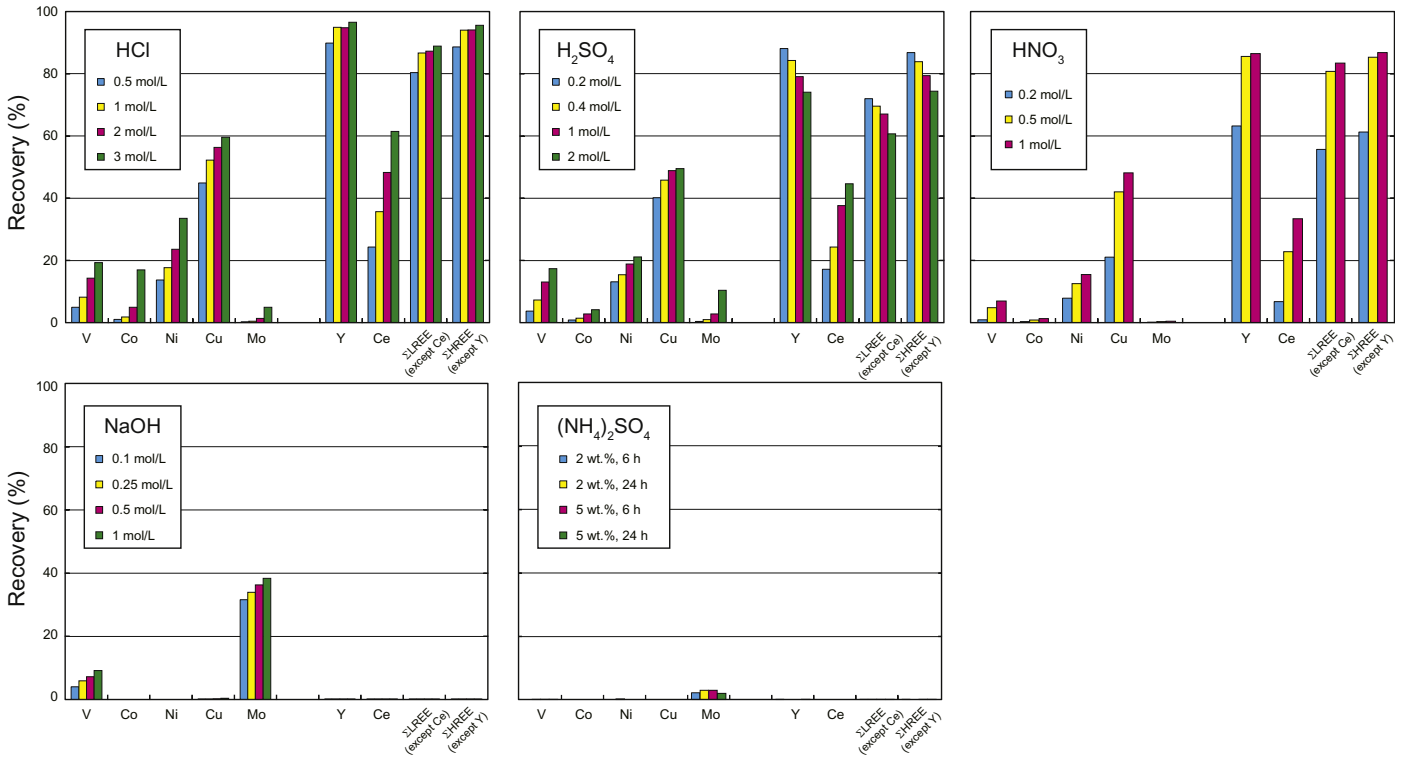

FIGURE 28 Recoveries from JMS-2 reference sample as a function of reagent concentration. *Modified from Takaya et al. (2014).*

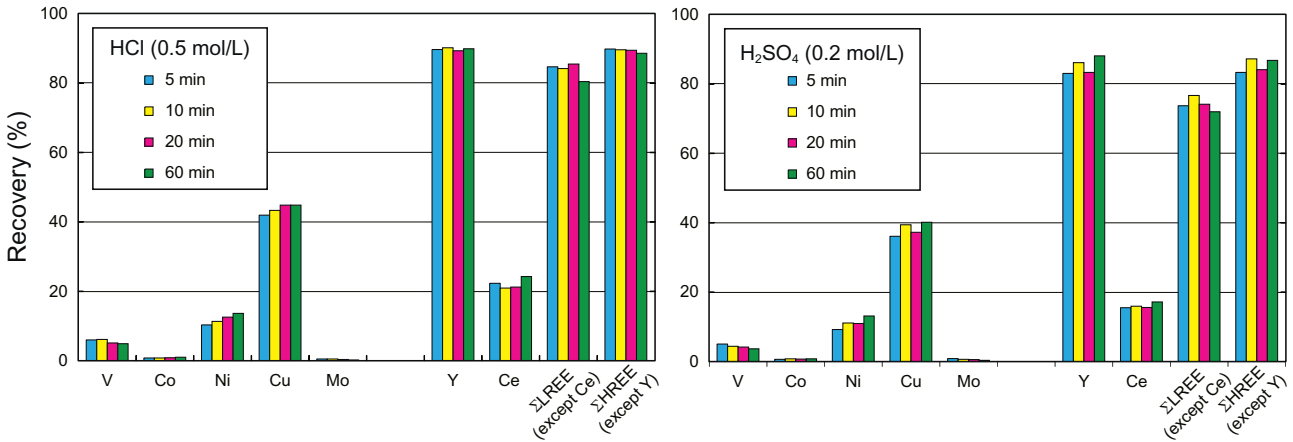

FIGURE 29 Recoveries from JMS-2 reference sample as a function of leaching time. *Modified from Takaya et al. (2014).*

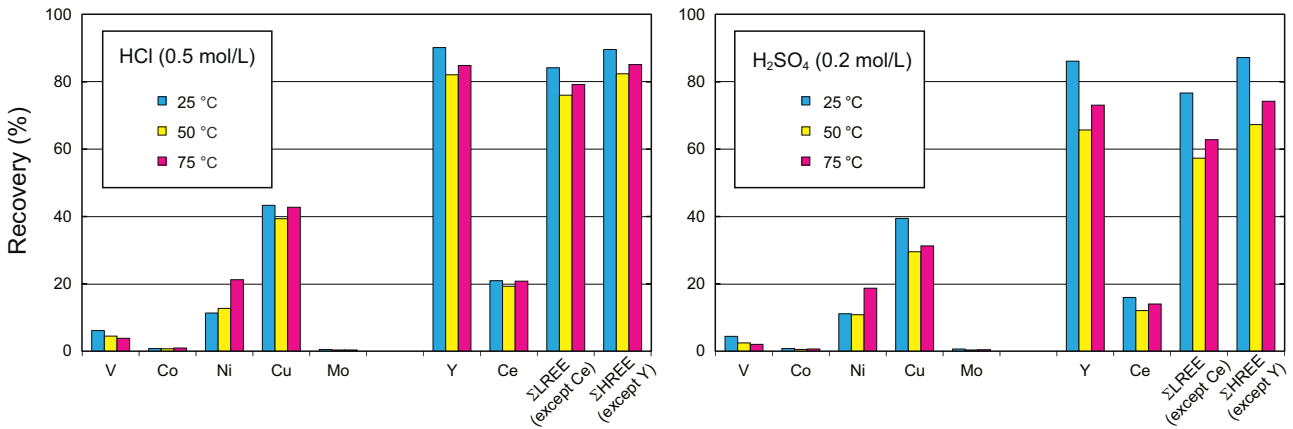

FIGURE 30 Recoveries from JMS-2 reference sample as a function of temperature. *Modified from Takaya et al. (2014).*

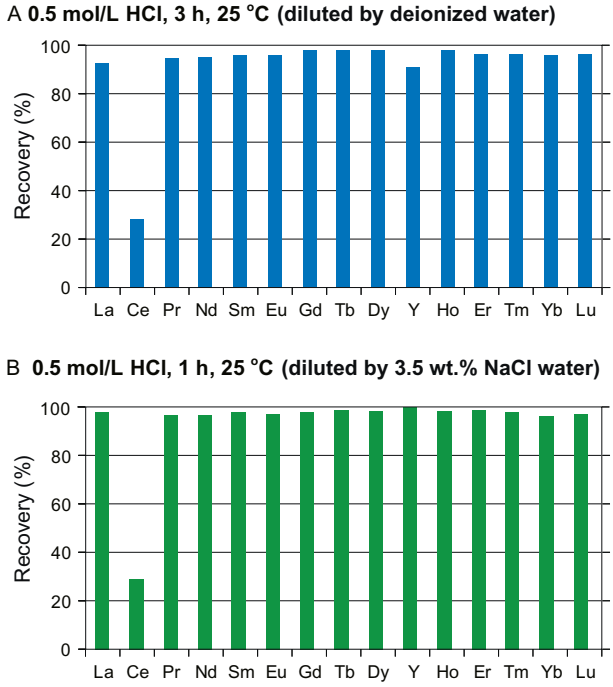

FIGURE 31 Results of experiments on concentrations of leaching reagents diluted by deionized water and 3.5 wt.% NaCl water (mud from Site 68, Core 1, Section 3, 50–52 cm, ΣREY = 1133 ppm).

by-products is difficult and costly. In contrast, after leaching with hydrochloric acid, chloride ions in the leachate and residual mud can be simply converted to nontoxic sodium chloride by addition of sodium hydroxide (NaOH) or sodium hydrogen carbonate ($NaHCO_3$). Adoption of this method will minimize both the cost of acid leaching and deleterious impacts on the surrounding environment. We have confirmed that REY recovery rates achieved by diluting the hydrochloric acid with seawater are much the same as those achieved by diluting with deionized water, so costs can be further reduced by using seawater (Fig. 31). For leaching in a leaching pool, the leaching solution can be separated from residual mud by using a hydrocyclone, or by gravitational separation or filtration.

7.2.4 Separation and Precipitation of REY

After recovery of leachate, REY can be chemically separated (precipitated) as carbonates or oxalates by adding sodium bicarbonate ($NaHCO_3$) or oxalic acid ($H_2C_2O_4$) solution; recovered carbonates or oxalates can then be transported to an onshore facility for further refining by established processes (Fig. 24).

After separation of REY carbonates or oxalates from the leaching solution, it is necessary to neutralize and detoxify the residual solution and mud. If hydrochloric acid is used as the leaching solution, and the acid remaining in the residual solution and mud is neutralized and detoxified by adding appropriate amounts of sodium hydroxide or sodium hydrogen carbonate, the neutralized leaching solution and residual mud can be reused as the dilute solution in subsequent leaching and landfill or in construction materials (e.g., concrete), respectively.

8 SUMMARY AND CONCLUSIONS

Extensive deposits of deep-sea mud containing high REY concentrations have been identified in the eastern South and central North Pacific. The distribution of REY-rich muds in the Pacific suggests that they formed as a result of adsorption of REY in seawater by Fe/Mn-oxyhydroxides in hydrothermal plumes emanating from the EPR. Similar REY-rich deep-sea sediments were also reported from the Indian and Atlantic Oceans by a few researchers. However, the extent and amounts of these REY-rich muds are likely to be much smaller than the Pacific Ocean REY-rich mud, because hydrothermal activity in the Indian and Atlantic Oceans suggested by helium-3 anomalies (δ^3He) in mid-depth ($\sim$2500 m water depth) seawater is much lower than the Pacific Ocean.

Bulk-rock composition of ΣREY, P_2O_5, and CaO, as well as XAFS/μ-XRF analyses of apatite minerals, indicates that apatite is a major host mineral of REY in REY-rich muds. On the other hand, multielement compositions (including Fe_2O_3, TiO_2, and K_2O) of the bulk samples suggest that REY-rich muds cannot be formed by a simple mixing of apatite with other components including terrigenous and biogenic components. Thus, even though apatite is regarded as a main host of REY, other phases (e.g., Fe- and Mn-oxyhydroxides) are likely to be involved in REY-enrichment in REY-rich mud as a carrier of REY.

The deep-sea REY-rich mud is characterized by (1) tremendous resource potential by virtue of their wide distribution, (2) high REY concentrations with significant HREE enrichment, (3) a stratiform distribution that allows relatively simple and cost-effective exploration, (4) very low concentrations of radioactive elements such as Th and U, and (5) ease of extraction of REY by acid leaching. These features demonstrate that the REY-rich mud in the Pacific Ocean could constitute a highly promising REY resource for the future, even though the great water depths (up to $>$5000 m) have a certain impact on the technological and economic viability of deep-sea mining of REY-rich mud.

A system to mine REY-rich muds can be developed based on a system developed and tested to mine sulfide-rich muds in the Red Sea and manganese nodules in the Pacific Ocean. In case of lifting REY-rich muds from very deep

water (>5000 m), however, pressurized air-lift system will be needed. REY-rich muds processed by acid leaching with dilute hydrochloric acid (1 mol/L HCl) for only 5 min at temperatures of about 25 °C can provide better than 90% recovery of REY, which can then be chemically separated and precipitated as REY carbonates or oxalates by using already established techniques.

ACKNOWLEDGMENT

This research was financially supported by the Japan Society for the Promotion of Science (JSPS) through Grants-in-Aid No. 22226015 to Y. K.

ABBREVIATIONS

CCD	carbonate compensation depth
DSDP	Deep Sea Drilling Project
EPR	East Pacific Rise
HREE	heavy rare-earth elements
LREE	light rare-earth elements
MORs	mid-ocean ridges
ODP	Ocean Drilling Program
REE	rare-earth elements
REY	rare-earth elements and yttrium
SCD	silica compensation depth
XAFS	X-ray absorption fine structure
μ-XRF	micro-focused X-ray fluorescence
ΣHREE	total amounts of heavy rare-earth elements
ΣREY	total amounts of rare-earth elements and yttrium

REFERENCES

Amann, H., 1983. In: OCEANS '83, Proceedings.

Amann, H., 1985. Mar. Min. 5, 103.

Baker, E.T., German, C.R., Elderfield, H., 1995. Hydrothermal plumes over spreading-center axes: global distributions and geological inferences. In: Humphris, S.E., Zierenberg, R.A., Mullineaux, L.S., Thomson, R.E. (Eds.), Seafloor Hydrothermal Systems: Physical, Chemical, Biological, and Geological Interactions. Geophysical Monograph Series, vol. 91. American Geophysical Union, Washington, DC, p. 47.

Bao, Z., Zhao, Z., 2008. Ore Geol. Rev. 33, 519.

Barrett, T.J., Jarvis, I., 1988. Chem. Geol. 67, 243.

Barrett, T.J., Taylor, P.N., Lugowski, J., 1987. Geochim. Cosmochim. Acta 51, 2241.

Blackburn, J., Hanrahan, S., 2010. Offshore Production System Definition and Cost Study. Nautilus Minerals, Tronto, p. 275.

Castor, S.B., Hedrick, J.B., 2006. Rare earth elements. Industrial Minerals, seventh ed. Society for Mining, Metallurgy, and Exploration, Littleton, CO, p. 769.

Christie, D.M., Dieu, J.J., Gee, J.S., 1995. Proc. Ocean Drill. Prog. Sci. Results 144, 495.

Courtois, C., Clauer, N., 1980. Sedimentology 27, 687.

de Baar, H.J., Bacon, M.P., Brewer, P.G., Bruland, K.W., 1985. Geochim. Cosmochim. Acta 49, 1943.

Dubinin, A.V., 2000. Lithol. Miner. Resour. 35, 101.

Dubinin, A.V., Rimskaya-Korsakova, M.N., 2011. Lithol. Miner. Resour. 46, 1.

Dubinin, A.V., Rozanov, A.G., 2001. Lithol. Miner. Resour. 36, 268.

Dubinin, A.V., Sval'nov, V.N., 2000. Lithol. Miner. Resour. 35, 520.

Dubinin, A.V., Sval'nov, V.N., Berezhnaya, E.D., Rimskaya-Korsakova, M.N., Demidova, T.P., 2013. Lithol. Miner. Resour. 48, 175.

ETOPOv2; National Geophysical Data Center, 2006. http://www.ngdc.noaa.gov/mgg/fliers/06mgg01.html (accessed March 14, 2014).

Floyd, P.A., Castillo, P.R., 1992. Proc. Ocean Drill. Prog. Sci. Results 129, 361.

Goldstein, S.J., Jacobsen, S.B., 1988. Earth Planet. Sci. Lett. 89, 35.

Gromet, L.P., Dymek, R.F., Haskin, L.A., Korotev, R.L., 1984. Geochim. Cosmochim. Acta 48, 2469.

Heezen, B.C., MacGregor, I.D., Foreman, H.P., Forristall, G., Hekel, H., Hesse, R., Hoskins, R.H., Jones, E.J.W., Krasheninnikov, V.A., Okada, H., Ruef, M.H., 1973. The post Jurassic sedimentary sequence on the Pacific plate: a kinematic interpretation of diachronous deposits. In: Heezen, B.C., MacGregor, I.D. (Eds.), The Initial Reports of the Deep Sea Drilling Project, vol. 20. U.S. Government Printing Office, Washington, DC, p. 725.

Humphries, M., 2010. Rare Earth Elements: The Global Supply Chain: CRS Report for Congress, R41347. Congressional Research Service, Washington, DC, p. 27.

Hüneke, H., Henrich, R., 2011. Pelagic sedimentation in modern and ancient oceans. In: Hüneke, H., Mulder, T. (Eds.), Deep-Sea Sediments. Developments in Sedimentology, vol. 63. Elsevier, Netherlands, p. 215.

International Seabed Authority, Polymetallic Nodules. ISA Technology Brochure. http://www.isa.org.jm/en/documents/technical/ENG7.pdf (accessed March 14, 2014).

Jarvis, I., 1985. Initial Rep. Deep Sea Drill. Proj. 85, 781.

Kashiwabara, T., Toda, R., Fujinaga, K., Honma, T., Takahashi, Y., Kato, Y., 2014. Chem. Lett. 43, 199.

Kato, Y., Fujinaga, K., Nakamura, K., Takaya, Y., Kitamura, K., Ohta, J., Toda, R., Nakashima, T., Iwamori, H., 2011. Nat. Geosci. 4, 535.

Kon, Y., Hoshino, M., Sanematsu, K., Morita, S., Tsunematsu, M., Okamoto, N., Yano, N., Tanaka, M., Takagi, T., 2014. Resour. Geol. 64, 47.

Lupton, J.E., 1995. Hydrothermal plumes: near and far field. In: Humphris, S.E., Zierenberg, R.A., Mullineaux, L.S., Thomson, R.E. (Eds.), Seafloor Hydrothermal Systems: Physical, Chemical, Biological, and Geological Interactions. Geophysical Monograph Series, vol. 91. American Geophysical Union, Washington, DC, p. 317.

Lupton, J.E., 1998. J. Geophys. Res. 103, 15853.

Lyle, M., Pälike, H., Nishi, H., Raffi, I., Gamage, K., Klaus, A., 2010. Sci. Drill. 9, 4.

Müller, R.D., Sdrolias, M., Gaina, C., Roest, W.R., 2008. Geochem. Geophys. Geosyst. 9, Q04006. http://dx.doi.org/10.1029/2007GC001743.

Murakami, H., Ishihara, S., 2006. Shigen-Tishitsu 56, 197 (in Japanese with English abstract).

Murray, R.W., Leinen, M., 1993. Geochim. Cosmochim. Acta 57, 4141.

Nawab, Z.A., 1984. Deep Sea Res. A 31, 813.

Nemliher, J.G., Baturin, G.N., Kallaste, T.E., Murdmaa, I.O., 2004. Lithol. Miner. Resour. 39, 468.

Pattan, J.N., Parthiban, G., 2011. J. Asian Earth Sci. 40, 569.

Pattan, J.N., Rao, C.M., Higgs, N.C., Colley, S., Parthiban, G., 1995. Chem. Geol. 121, 201.

Roskill Information Services Ltd., 2007. The Economics of Rare Earths & Yttrium, 13th ed. Roskill, London, p. 340.
Ruhlin, D.E., Owen, R.M., 1986. Geochim. Cosmochim. Acta 50, 393.
Rüth, C., Well, R., Roether, W., 2000. Deep Sea Res. I 47, 1059.
Schüler, D., Buchert, M., Liu, R., Dittrich, S., Merz, C., 2011. Study on Rare Earths and Their Recycling. Final report for The Greens/EFA group in the European Parliament, OKO-Insititut e.V, p. 140.
Service, R.F., 2010. Science 327, 1596.
Shaw, S., Chegwidden, J., 2012. Roskill Information Services, http://www.roskill.com/news/4th-baotou-china-rare-earth-industry-forum/ (accessed March 14, 2014).
Shinha, M.C., Evans, R.L., 2004. Geophysical constraints upon the thermal regime of the ocean crust. In: German, C.R., Lin, J., Parson, L.M. (Eds.), Mid-Ocean Ridges: Hydrothermal Interactions Between the Lithosphere and Oceans. Geophysical Monograph Series, vol. 148. American Geophysical Union, Washington, DC, p. 19.
Sørensen, H., Bailey, J.C., Rose-Hansen, J., 2011. Bull. Geol. Soc. Den. 59, 69.
Srinivasan, A., Top, Z., Schlosser, P., Hohmann, R., Iskandarani, M., Olson, D.B., Lupton, J.E., Jenkins, W.J., 2004. J. Geophys. Res. 109, C06012. http://dx.doi.org/10.1029/2003JC002028.
Takaya, Y., Hiraide, T., Fujinaga, K., Nakamura, K., Kato, Y., 2014. J. MMIJ 130, 94. (in Japanese with English abstract).
Taylor, S.R., McLenann, S.M., 1985. The Continental Crust: Its Composition and Evolution. Blackwell, Oxford, p. 312.
Terashima, S., Imai, N., Taniguchi, M., Okai, T., Nishimura, A., 2002. Geostand. Newslett. 26, 85–94.
Tracey Jr., J.I., Sutton, G.H., Nesteroff, W.D., Galehouse, J., Von der Borch, C.C., Moore, T., Lipps, J., Ul Haq, U.Z.B., Beckmann, J.P., 1971. Initial Rep. Deep Sea Drill. Proj. 8, 17.
U.S. Department of the Interior and U.S. Geological Survey, 2013. Rare Earths, Mineral Commodity Summaries 2013. U.S. Government Printing Office, Washington, DC.
van Andel, T.H., 1975. Earth Planet. Sci. Lett. 26, 187.
Wheeler, A.J., Stadnitskaia, A., 2011. Benthic deep-sea carbonates: reefs and seeps. In: Hüneke, H., Mulder, T. (Eds.), Deep-Sea Sediments. Developments in Sedimentology, vol. 63. Elsevier, Netherlands, p. 397.
Wu, C., Huang, D., Guo, Z., 1990. Acta Geol. Sin. 3, 193.
Wu, C., Yuan, Z., Bai, G., 1996. Rare earth deposits in China. In: Jones, A.P., Wall, F., Williams, C.T. (Eds.), Rare Earth Minerals: Chemistry, Origin, and Ore Deposits. Mineralogical Society Series, vol. 7. Chapman and Hall, London, p. 281.
Wu, J., Wells, M.L., Rember, R., 2011. Geochim. Cosmochim. Acta 75, 460.
Xiujuan, F., Tao, T., Yichun, Z., 2012. Procedia Environ. Sci. 12, 917.
Yang, X.-Y., Sun, W.-D., Zhang, Y.-X., Zheng, Y.-F., 2009. Geochim. Cosmochim. Acta 73, 1417.
Yasukawa, K., Liu, H., Fujinaga, K., Machida, S., Haraguchi, S., Ishii, T., Nakamura, K., Kato, Y., 2014. J. Asian Earth Sci. 93, 25.

Index

Note: Page numbers followed by "*f*" indicate figures, and "*t*" indicate tables.